UNIVERSITÀ DEGLI STUDI FIRENZE

PhD in Physics and Astronomy

CYCLE XXXIII

COORDINATOR Prof. D'Alessandro Raffaello

Development, testing and application to real case studies of a three-dimensional tomographic technique based on muon transmission radiography

Sviluppo, test e applicazione a casi di studio reali di una tecnica tomografica tridimensionale basata sulla radiografia muonica per trasmissione

Academic Discipline (SSD) FIS/04

Doctoral Candidate
Dr. Baccani Guglielmo

Supervisors
Dr. Bonechi Lorenzo

Prof. D'Alessandro Raffaello

Coordinator
Prof. D'Alessandro Raffaello

Years 2017/2020

Contents

Introduction **5**

1 Cosmic ray muons and muography **7**
1.1 Some definitions . . . 7
1.1.1 Cartesian and spherical coordinate systems . . . 7
1.1.2 Particle differential and integral flux . . . 8
1.2 Cosmic rays . . . 9
1.3 Cosmic muon flux at sea level . . . 12
1.3.1 Magnetic effects and East-West asymmetry . . . 17
1.3.2 Temporal variations . . . 18
1.4 Muon interaction with matter . . . 19
1.4.1 Energy loss . . . 19
1.4.2 Multiple scattering . . . 22
1.5 Muography . . . 24
1.5.1 Transmission and absorption radiography . . . 25
1.5.2 Scattering tomography . . . 26

2 The MIMA detector **28**
2.1 Hardware . . . 29
2.1.1 Detector structure . . . 29
Local and global frames of reference . . . 31
2.1.2 Trigger configuration . . . 33
2.1.3 Geometrical factor and effective area . . . 34
2.2 Analysis procedures . . . 37
2.2.1 Track reconstruction . . . 37
2.2.2 Equalization of gains . . . 38
2.2.3 Detector resolution and multiple scattering . . . 41
2.2.4 Detector efficiency . . . 43
2.2.5 Atmospheric pressure variation . . . 46
2.2.6 Track angular distribution . . . 47
2.2.7 East-West effect . . . 50

3 Muon transmission radiography **52**
3.1 Transmission 52
3.2 Simulations 54
3.2.1 Experimental muon spectra 54
3.2.2 Geant4 simulation 56
3.2.3 Range-based simulations 57
muRange simulation 60
Simulation with conversion map 62
Estimation of measurement uncertainty 64
3.2.4 Soft electron background 66

4 Muon transmission tomography **68**
4.1 Inversion problem 69
4.1.1 Non uniqueness and regularization methods 70
4.2 Inversion algorithms 71
4.2.1 Minimum of Chi-squared 71
4.2.2 The ART family algorithms 73
SART 74
DART 74
4.2.3 Triangulation 75

5 Muography of the Temperino mine **78**
5.1 The Temperino mine at the San Silvestro park 78
5.1.1 The Archaeological park 78
5.1.2 The target: the Temperino mine and the Gran Cava . . 80
5.1.3 Geometric structure of the target 82
Lidar of the hill and of the Temperino mine 82
Position and orientation of the detector 83
Mesh of the known cavities and depth maps 86
5.2 Muon radiography measurements 89
5.2.1 Muon count maps 90
5.2.2 Transparency maps 91
5.2.3 Opacity maps 92
5.2.4 Average density maps 93
5.3 Tomography reconstruction 96
5.3.1 Initialization of the problem: World, Voxels and Rays . 96
3D slicing 97
Selection of Voxels and Rays 98
Air volumes known a priori 99
Ray-Voxel intersection length 100
MacroVoxel 102

Simulated tomography 104
5.3.2 Tomographic inversion 104
Minimum of Chi-squared 105
SART 109
Triangulation 112

6 Conclusions and future developments 115

A Threshold momentum for multilayer target 119

B Maps of the opacity measurements 121

Introduction

The present work is part of the research on muon radiography and focuses on the development and application of tomographic inversion algorithms, applied to muographic measurements carried out inside a mine. A brief summary of the contents of the various chapters is shown below.

In the first chapter, after having provided some useful definitions, cosmic rays are presented with particular attention to the flux of muons at sea level, whose dependence is described as a function of the direction of propagation, the energy of the particles and time. The phenomena related to the interaction processes of muons with matter (loss of energy and multiple scattering), which are the basis of the relative muography techniques (transmission radiography and scattering tomography), are then described.

Chapter two describes the MIMA muon tracker developed and used by the muon radiography group of Florence. After referring to previous works, the structure of the detector is briefly described which is used to define the local reference system for the track reconstruction. Once the trigger configuration usually adopted has been presented, the geometric factor of the detector is calculated. Then a series of analysis are presented which are repeated for each single measurement: the reconstruction of the tracks, the equalization of the gains, the calculation of the spatial and angular resolution of the detector and the measurement of the trigger efficiencies of each plane. Therefore, for some measurements made in free-sky, i.e. without objects in the detector acceptance, the dependence of the muon flux on atmospheric pressure and azimuth angle is evaluated. To present this latter result, the angular distribution of the muon tracks is first described.

In the third chapter the analysis process used to carry out a muon radiography measurement is presented. A target measurement, with the detector pointed towards the target of interest, is compared with a free-sky measurement allowing to define the muon transmission (or transparency). The same process is repeated through simulations obtained from the knowledge of the differential muon flux at ground level. These can be based on the complete simulation of the physical interaction process of muons with the target or on

the estimate of the average range of muons in a certain material as a function of their initial energy. In this second case, the simulation allows to obtain a measure (with uncertainty) of the angular distribution of opacity of the target and, once the thickness of the studied target is known, of the distribution of average density which are useful for obtaining direct quantitative information from the measurements.

Chapter four describes the tomographic inversion problem and some limitations that arise with the muon radiography technique: the goal is to combine the opacity measurements from multiple observation points, to reconstruct the spatial distribution of density with particular focus on void identification, which generate an evident signal in the average density maps. Referring to similar works, the techniques of tomographic inversion and reconstruction of cavities employed are presented: Chi-square minimum, ART-type iterative algorithms and triangulation.

Finally, in chapter five, what was previously presented is applied to a real case study: the Temperino mine in the San Silvestro park in Campiglia Marittima. After quickly describing the history of the park and the geophysical characteristics of the mine, the geometry of the muography measurements made is presented in detail: the airborne lidar reliefs, those made with the laser scanner and the position and aiming measurements of the detectors define the geometry of the problem. The results obtained from the analysis of each single measurement are shown as described in chapter three. Then the maps of the angular distribution of opacity and the geometric information of the target are provided as input of a tomographic inversion software specially developed for this work. Finally, the results obtained by applying the inversion techniques presented in chapter four are shown.

Chapter 1

Cosmic ray muons and muography

1.1 Some definitions

1.1.1 Cartesian and spherical coordinate systems

Consider a generic vector $\boldsymbol{r}$ in an orthogonal Cartesian reference system. It is assumed that the system has the z axis arranged vertically according to the local direction of gravity (thus corresponding to the zenith). This vector can be expressed through its Cartesian coordinates as $\boldsymbol{r} = (x, y, z)$. However, it will often be useful to refer to the angles that $\boldsymbol{r}$ forms with the Cartesian axes. For this reason we also introduce a spherical coordinate system described by the triad (r, θ, φ) where r represents the magnitude of the vector $\boldsymbol{r}$, θ is the angle that $\boldsymbol{r}$ forms with the z axis and it is called polar angle or zenith angle, φ is the counterclockwise angle that goes from the x axis to the orthogonal projection of $\boldsymbol{r}$ on the xy plane and it is called azimuth. Expressing the previous definitions in formulas and inverting them we get the following equations:

$$\begin{cases} r = \sqrt{x^2 + y^2 + z^2} \\ \theta = \arctan \dfrac{\sqrt{x^2 + y^2}}{z} \\ \varphi = \arctan \dfrac{y}{x} \end{cases} \qquad \begin{cases} x = r \sin\theta \cos\varphi \\ y = r \sin\theta \sin\varphi \\ z = r \cos\theta \end{cases}, \tag{1.1}$$

necessary to pass from the Cartesian coordinate system to the spherical one and vice versa.

However the same term “azimuth” is usually used in astronomy, but also in the fields of navigation and cartography, to indicate the horizontal angle

measured clockwise from the North. In order not to confuse the two meanings and since both will be used, we define the latter one as astronomical azimuth or clockwise azimuth and will be characterized by the symbol φ_A. We will see later the relationship between these two azimuth angles based on the choice made for the direction of the x axis. Finally, for completeness, we define the elevation α_E as the angle that the vector $\boldsymbol{r}$ forms with the horizontal xy plane. Consequently the elevation and the polar angle are related by the equation $\alpha_E = 90° - \theta$.

1.1.2 Particle differential and integral flux

The differential energy flux (or energy spectrum) of particles i from direction (θ, φ) with energy E, $\phi_i(\theta, \varphi, E)$, is defined as the number of i particles, dN_i, incident upon an element of area, dA, per unit time, dt, within an element of solid angle around (θ, φ), $d\Omega$, per energy interval around E, dE. Thus,

$$\phi_i(\theta, \varphi, E) = \frac{dN_i}{dA\, dt\, d\Omega\, dE} \quad [\mathrm{cm}^2\,\mathrm{s}\,\mathrm{sr}\,\mathrm{GeV}]^{-1}.$$

By integrating the previous equations, the integral energy flux, $\Phi_i(\theta, \varphi, \geq E)$, defined as the integral flux of particles i with energy greater than E, is obtained as:

$$\Phi_i(\theta, \varphi, \geq E) = \int_E^\infty \phi_i(\theta, \varphi, E')\, dE' \quad [\mathrm{cm}^2\,\mathrm{s}\,\mathrm{sr}]^{-1}.$$

In a similar way, the differential and the integral momentum flux can be defined as:

$$\phi_i(\theta, \varphi, p) = \frac{dN_i}{dA\, dt\, d\Omega\, dp} \quad [\mathrm{cm}^2\,\mathrm{s}\,\mathrm{sr}\,\mathrm{GeV}/c]^{-1},$$
$$\Phi_i(\theta, \varphi, \geq p) = \int_p^\infty \phi_i(\theta, \varphi, p')\, dp' \quad [\mathrm{cm}^2\,\mathrm{s}\,\mathrm{sr}]^{-1},$$

where p is the particle momentum and dp is the momentum interval around p. For simplicity we will refer to the integral fluxes as $\Phi_i(\theta, \varphi, E)$ and $\Phi_i(\theta, \varphi, p)$.

Particle spectrum can as well be represented per unit rigidity, R, with R defined as

$$R = \frac{pc}{Ze} \quad [\mathrm{GV}],$$

where (pc) is the kinetic energy of a relativistic particle and (Ze) is the electric charge of the particle. The reason for using this quantity is that different particles with the same rigidity follow identical paths in a given magnetic field.

1.2 Cosmic rays

Cosmic rays are high-energy particles, mainly coming from outside the Solar System.

They are divided into primary cosmic rays and secondary cosmic rays. Primary cosmic rays, which originate outside the Earth's atmosphere, are made up of about 99% nuclei, and about 1% are electrons. The nuclei of cosmic rays in turn differentiate into protons (hydrogen nuclei) for 90%, alpha particles (helium nuclei) for 9% and nuclei of heavier elements for the remaining 1%. A small fraction consists of antimatter particles, such as positrons or antiprotons. The precise measurement of the energy distribution of this remaining fraction is an active research area.

After the discovery of radioactivity it was assumed that the ionization of the air was caused exclusively by the radiation produced by radioactive elements naturally present on Earth. In 1909 Theodor Wulf observed that the electrometer he made discharged faster on the top of the Eiffel Tower than on the ground, indicating the presence of an increasing flux of ionizing radiation as the altitude increases [1]. In 1911 Domenico Pacini, observing the decrease of ionization rate at a depth of 3 meters from the surface of a lake, he concluded that some of the ionization must be due to sources other than terrestrial radioactivity [2]. The following year Victor Hess (Nobel Prize in Physics in 1936) made measurements with electrometers transported with aerostatic balloons to heights otherwise unattainable, observing ionization rates about four times higher than those measured on the ground [3].

In the 1920s, the term "cosmic rays" was coined by Robert Millikan. He performed ionization measurements at various heights around the world and hypothesized that primary cosmic rays were highly energetic electromagnetic radiation, i.e. gamma rays (hence the name of cosmic "rays") that produced secondary electrons through Compton scattering in the atmosphere. However, it was soon realized that the main component of cosmic rays are actually charged particles.

In 1930 Bruno Rossi foresaw an asymmetry in the flux of charged cosmic rays due to their interaction with the Earth's magnetic field: the so-called East-West effect. Later a higher intensity was actually measured from the West, thus demonstrating that most of the primary cosmic rays are positively charged [4].

Bruno Rossi, during one of his cosmic ray measurements, observed that the number of simultaneous counts of two Geiger counters separated from each other was greater than those expected from random coincidences, thus assuming the formation of cosmic showers.

Figure 1.1 shows the "all-particle" spectrum. The differential energy

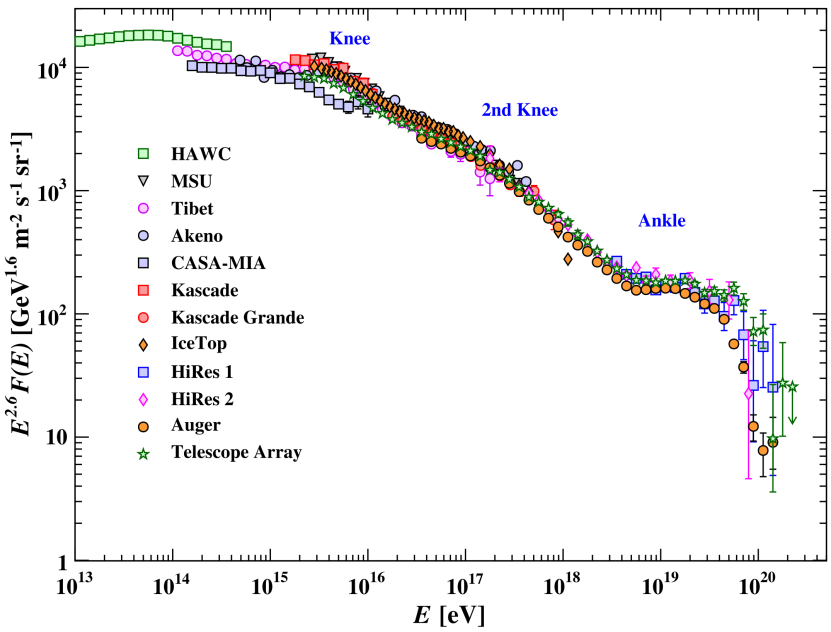

Figure 1.1: The all-particle spectrum as a function of E (energy-per-nucleus) from air shower measurements [5, chapter 29.5].

spectrum has been multiplied by $E^{2.6}$ in order to display the features of the steep spectrum that are otherwise difficult to discern. The spectrum of cosmic rays is well described by a power law of the form $\phi_p(E) = A_p E^{-\gamma_p}$ with $\gamma_p = 2.7$ for values energy lower than 10^{15} eV. The steepening that occurs between 10^{15} eV and 10^{16} eV is known as the "knee" of the spectrum. Another steepening occurs around 10^{17} eV, known as the second knee. The feature around $10^{18.5}$ eV is called the ankle of the spectrum, where the spectrum becomes less steep.

The most energetic particles ever detected come from cosmic rays: on 15 October 1991 the Fly's Eye detected an ultra-high-energy cosmic ray with an energy of approximately $3 \cdot 10^{20}$ eV, about 40 million times the energy of protons accelerated at the Large Hadron Collider [6].

The origin of cosmic rays is not yet clear. It appears that a significant fraction comes from the Supernovae explosions. According to some theories, however, they can also originate from Active Galactic Nuclei (AGN), quasars and Gamma-Ray Bursts (GRBs).

When a primary cosmic ray enter the Earth's atmosphere they interact with atoms and molecules, especially oxygen and nitrogen, trough strong interaction and electromagnetic process (like pair production). The collision produces a cascade of lighter particles, secondary cosmic rays, including X-

rays and γ, neutrons, mesons (such as pions and kaons), electrons and muons. Some of these particles (such as pions, positrons and muons) were identified for the first time in cosmic rays. Of all the secondaries, pions (π^+, π^-, π^0) are the most abundant [7].

The secondary particle spectra have a form which is similar to that of primary spectrum. For secondary pions it has the form

$$\phi_\pi(E) = A_\pi E^{-\gamma_\pi},$$

with an exponent, γ_π, very similar to that of the primary spectrum ($\gamma_\pi \approx \gamma_p$). The same relation holds for kaons as well.

If sufficiently energetic, hadrons will themselves initiate new hadronic interactions building up a hadron cascade, which for energetic events constitutes the core of a shower. However, unstable particles such as pions, kaons and other particles are also subject to decay.

Due to a very short mean life ($\tau_{\pi^0} \approx 8.4 \cdot 10^{-17}$ s) neutral pions (π^0) decay almost instantly into a pair of photons. The latter can produce electron-positron pairs which subsequently undergo bremsstrahlung, which again can produce electron-positron pairs, and so on, as long as the photon energy exceeds 1.02 MeV (two times the electron mass). Eventually, these repetitive processes build up an electromagnetic shower in the atmosphere.

Charged pions ($\pi^\pm$) have a mean life at rest of about $2.6 \cdot 10^{-8}$ s and decay via the processes

$$\pi^+ \to \mu^+ + \nu_\mu,$$
$$\pi^- \to \mu^- + \bar{\nu}_\mu,$$

into muons and neutrinos. At high energies their mean life, τ, is significantly extended by time dilatation: $\tau(E) = \tau_0\gamma$, where τ_0 is the mean life of the particle at rest and γ is the Lorentz factor. Pions with higher energy than the critical energy $\epsilon_\pi = 115$ GeV tend to interact with the atmosphere before decaying [chapter 30][5]. For the definition of the critical energy see section 1.4.1 on page 19.

The charged kaons ($K^\pm$) are strange mesons and have a mean life of about 12 ns. They also mostly decay (with a branching ratio of 64%) like

$$K^+ \to \mu^+ + \nu_\mu,$$
$$K^- \to \mu^- + \bar{\nu}_\mu.$$

The other decay processes lead to the formation of pions which in turn decay as described above.

We distinguish between three major cosmic ray components (partly already described) in the atmosphere: the hadronic component, the photon-electron component, and the muon component. The development of the three components is shown schematically in figure 1.2. Because of their different nature, the three components have different altitude dependencies as shown in figure 1.4 on page 15.

The competition between interaction and decay depends on the mean life and energy of the particles and on the density of the medium in which they propagate. For a given particle propagating in the atmosphere the respective probabilities for the interaction and decay processes become a function of energy, altitude and zenith angle. The decay probability of an unstable particle is given by [7]

$$W = 1 - \exp\left(-\int \frac{m_0}{\rho\tau_0 p} dX\right) \approx \frac{m_0 X}{\rho\tau_0 p},$$

where m_0 is the particle mass, ρ is the matter density, τ_0 is the particle average life at rest, p is the particle momentum, X is the crossed mass thickness or opacity, equal to the product of the average density by the length of the crossed material ($X = \bar{\rho} \cdot L$), and the second equality is valid if the integral is small. If a particle is incident in the atmosphere at a zenith angle, θ, the total mass thickness, and consequently also the decay probability, is enhanced by the factor $\sec\theta$ ($X = X_v \sec\theta$ where X_v is the vertical opacity).

At very low energies (or momentum) the decay probability increases and all mesons decay into muons, which subsequently decay while loosing energy at a rate that increases as their energy decreases (see figure 1.6 on page 19). This lead to a maximum in the muon differential energy spectrum shown in figure 1.3.

At constant density the competition between decay and interaction changes in favour of interaction with increasing energy since time dilatation reduces the probability for decay. For this reason, for the differential energy spectrum of the muons the following relations holds

$$\phi_\mu(E) \propto \phi_\pi(E) \quad \text{for } 10\,\text{GeV} < E < 100\,\text{GeV}$$
$$\phi_\mu(E) \propto \frac{\phi_\pi(E)}{E} \quad \text{for } E > 100\,\text{GeV},$$

which describes the steepening if the energy spectrum, as shown in figure 1.3.

1.3 Cosmic muon flux at sea level

The muon belongs to the lepton family and has a mass of $106\,\text{MeV}/c^2$ (about 200 times that of the electron). It is an unstable particle and has a mean

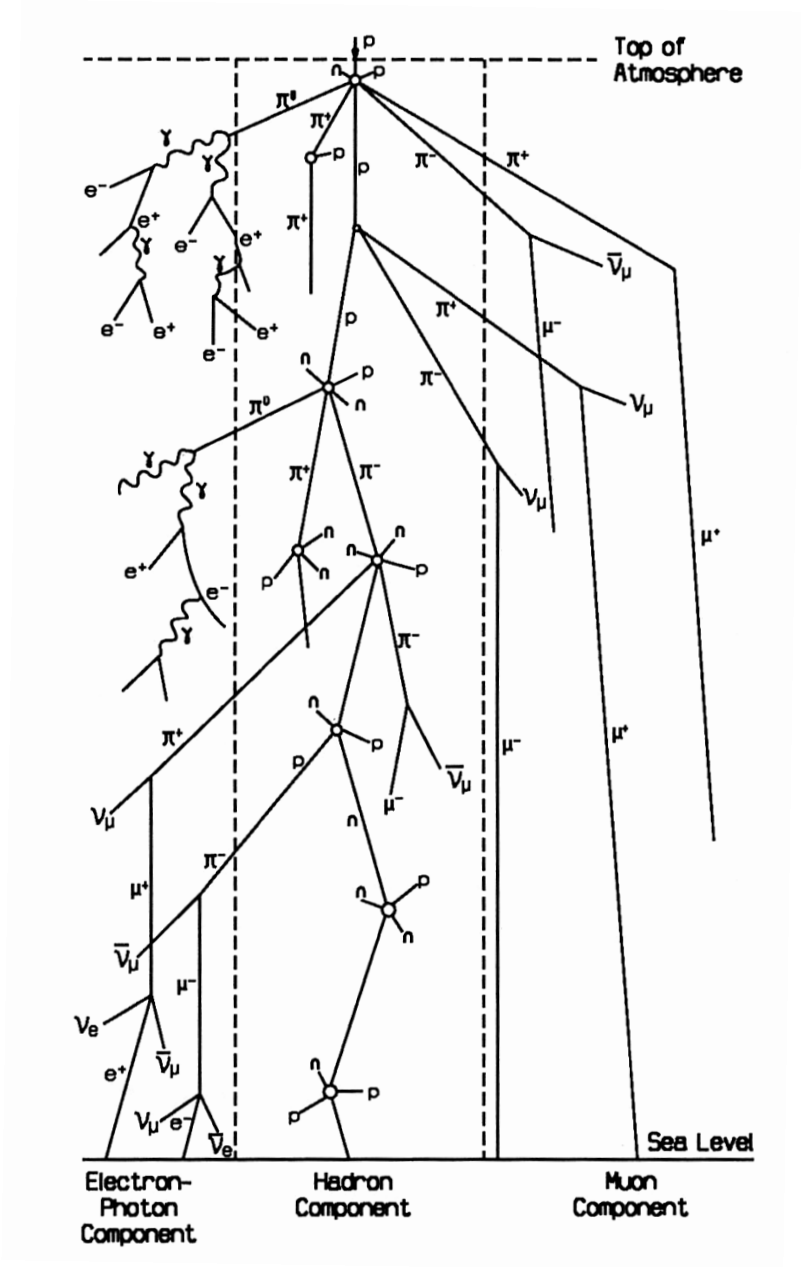

Figure 1.2: Cascade shower: schematic representation of particle production in the atmosphere. The three shower components are visible. The lateral spread is grossly exaggerated [7, chapter 1.5].

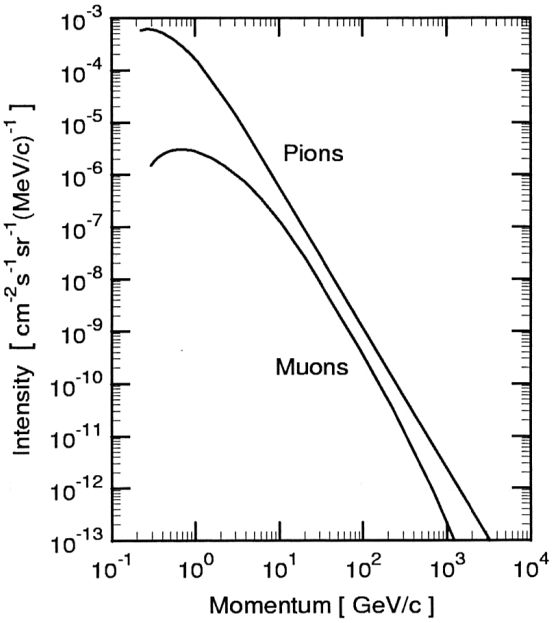

Figure 1.3: Muon differential momentum spectrum compared with parent pion differential spectrum [7, chapter 1.3].

life of about 2.2 µs, the second longest among unstable particles after that of the neutron. Being the lightest charged particle after the electron, the muon can almost exclusively decay according to the process

$$\mu^- \rightarrow e^- + \bar{\nu}_e + \nu_\mu,$$

while its positively charged antiparticle decays according to

$$\mu^+ \rightarrow e^+ + \nu_e + \bar{\nu}_\mu.$$

More rarely, a photon (1.4%) and an electron-positron pair ($3.4 \cdot 10^{-5}$) may also be present in the decay process.

Muons are mainly produced in the upper atmosphere (typically at an altitude of 15 km from the Earth's surface) and lose approximately 2 GeV before reaching the ground. Their energy and angular distribution reflects the convolution of the production spectrum, the loss of energy in the atmosphere and their decay. For example, muons with energy of 2.4 GeV have a decay length of approximately 15 km according to the time dilation predicted by the special theory of relativity (which is reduced to 8.7 km due to energy losses). Thanks to this phenomenon, a large fraction of the muons produced in the upper atmosphere can reach the Earth's surface before decaying, and it is thus possible to detect them on the ground.

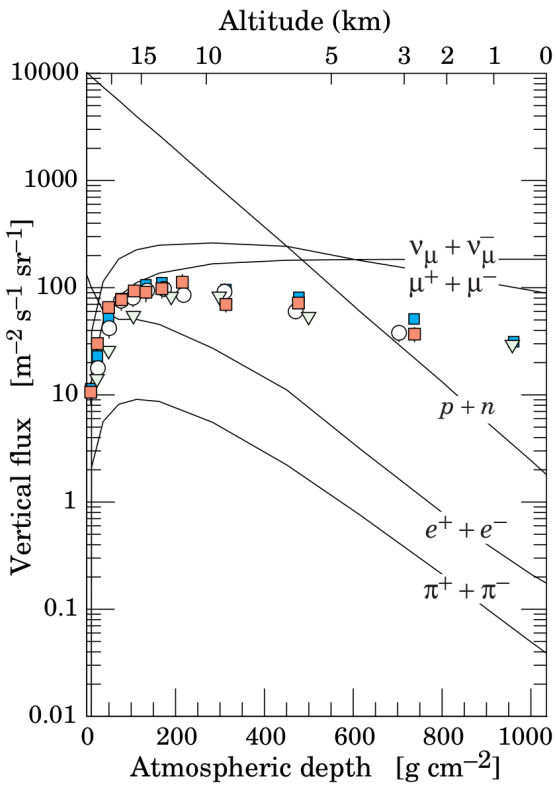

Figure 1.4: Vertical flux of cosmic rays in the atmosphere with $E > 1\,\mathrm{GeV}$ estimated from the theoretical flux of nucleons [5, chapter 30.3]. The points show the measurements corresponding to negative muons with $E_\mu > 1\,\mathrm{GeV}$.

Muons are the most frequent charged particles from cosmic rays at the sea level, with a vertical flux of about $70\,\mathrm{m}^{-2}\,\mathrm{s}^{-1}\mathrm{sr}^{-1}$ for energies greater than $1\,\mathrm{GeV}$ [5, chapter 30.3] (see figure 1.4). Nevertheless, for lower energies, there is also a non-negligible component of electrons, whose flux at sea level amounts to about 35% of that of muons. For electrons with momentum of $0.1\,\mathrm{GeV}$ a differential flux $\phi_V = 10^2\,(\mathrm{m}^2\,\mathrm{s}\,\mathrm{sr}\,\mathrm{GeV}/c)^{-1}$ is measured in the vertical direction [7, chapter 3.5.2]. For muons with the same momentum, a spectrum of the same order of magnitude is measured. However, electrons are part of the soft component that is completely shielded by 15 cm of lead, which corresponds to an opacity X of $167\,\mathrm{g}\,\mathrm{cm}^{-2}$. On the other hand, the hard component at sea level consists almost exclusively of muons ($p_\mu > 0.3\,\mathrm{GeV}/c$) and less than 1% are protons or other particles.

The integral muon flux, with momentum greater than p, depends on the zenith angle θ approximately as $\cos^n\theta$ (for $\theta < 75°$), where n depends on the atmospheric depth, X, and the momentum, p, i.e. $n = n(X, p)$. The

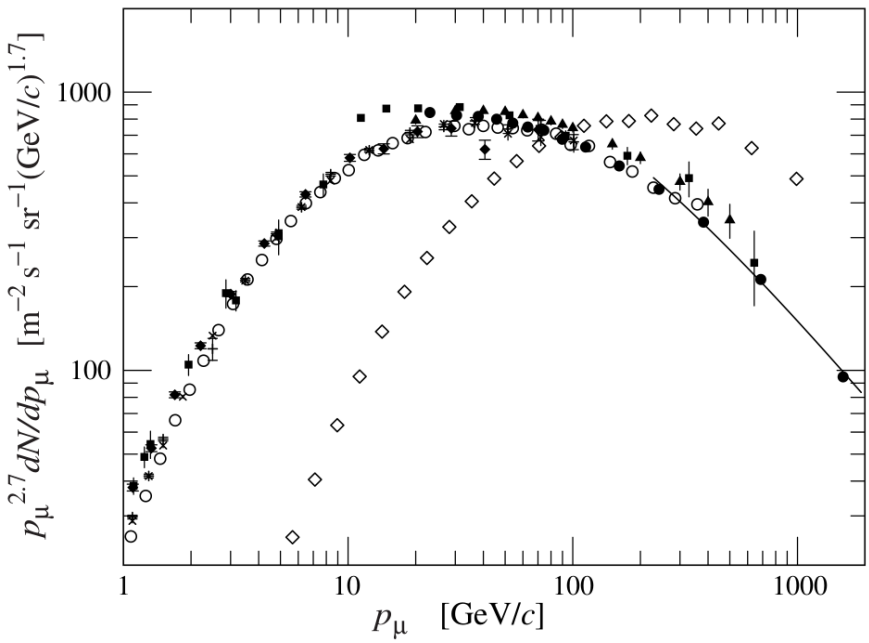

Figure 1.5: Spectrum of muons at sea level for $\theta = 0°$ on the left and for $\theta = 75°$ on the right (empty diamonds) [5, chapter 29]. The average energy of muons increases as the zenith angle of origin increases. The ordinate is multiplied by $p_\mu^{2.7}$ to compress the spectra.

value of n is around 1.7 for $E_\mu \approx 1\,\text{GeV}$, 2 for $E_\mu \approx 3\,\text{GeV}$ and than it decreases progressively until reaching -1 for very energetic muons ($E_\mu \gg \epsilon_\pi = 115\,\text{GeV}$) [5, chapter 29.3.1] (see figure 3.61 at page 433 of [7]).

Figure 1.5 shows the energy spectrum of cosmic ray muons at sea level for two different zenith angles: for large θ values, the layer of atmosphere that cosmic rays must cross is greater (precisely proportional to $\sec\theta$). Therefore the low-energy muons decay before reaching the ground while the energetic pions have time to decay before interacting, thus increasing the average energy of the muons: this cause a zenith angular muon enhancement (see figure 3.48 to 3.50 of [7]).

The differential momentum flux with p from $10\,\text{GeV}/c$ to $1000\,\text{GeV}/c$ has been determined very precisely in the angular range with zenith from 75° to 87.5° with large acceptance instruments, and different sets of data are compiled to obtain the differential momentum flux in the zenith range from 0° to 79° (see figure 3.40 to 3.43 of [7]).

An analytic expression giving a good fit to the muon energy spectrum observed in the atmosphere was obtained by Gaisser [8].

The low energy component of the differential muon flux weakly depends

on the azimuth angle φ because of the interaction of the mainly positive particles in the primarily cosmic radiation with the Earth's magnetic field (this is the so called East-West asymmetry) (see section 1.3.1).

Going into more detail, the muons spectrum depends on the measuring site (on its altitude, latitude and longitude) and varies with time: solar activity and variations in the atmospheric pressure influence the flux of cosmic muons as reported in section 1.3.2 [7, 9].

The charge ratio μ^+/μ^-, that is the ratio between the flux of μ^+ and the flux of μ^-, is equal to about 1.3 for a value of momentum from 10 GeV to 1 TeV. This value is due to the fact that most of the primary cosmic rays are composed of positively charged particles. In the interaction with the Earth's atmosphere, a series of new particles are created (the secondary cosmic rays) which tend to reduce the percentage excess of positively charged particles due to the charge symmetry of the production processes. The excess of positively charged particles allows us to understand the East-West asymmetry described in the next paragraph.

1.3.1 Magnetic effects and East-West asymmetry

Cosmic ray fluxes and spectra from eastern and western directions are different (there is a greater flux from the West) up to energies of about 100 GeV, because of the geomagnetic field and the positive charge excess of the primary radiation. This effect, which is called the East-West effect or East-West asymmetry, is strongest at the top of the atmosphere and, due to the zenith angle dependence of the cosmic ray flux ($\approx \cos\theta^2$), this asymmetry is less pronounced at sea level.

There exists also a longitude effect which is due to the fact that the geomagnetic dipole axis is asymmetrically located with respect to the Earth's rotation axis. In addition there are local magnetic anomalies (the South Atlantic anomaly is the main one).

Charged particles approaching the Earth from outer space follow curved trajectories because of the geomagnetic field in which they propagate. Disregarding the existence of the atmosphere (and any particle interaction with it), a particle can reach the Earth's surface or not only on the basis of the magnitude and direction of the local magnetic field, and of the rigidity and direction of propagation of the particle. A practical measure to compare and interpret particle measurements made at different locations on Earth, in particular at different geomagnetic latitudes, is the vertical cutoff rigidity (or cutoff rigidity), R_C, that depends on location and time. A frequently used method to compute the vertical cutoff rigidity of a particle is to consider an identical particle of opposite charge and opposite velocity being released in

radial outward direction at the reference altitude of 20 km above sea level. The effective cutoff rigidity is defined as the rigidity required for the particle to overcome trapping in the geomagnetic field and being able to escape to infinity.

Furthermore, due to the geomagnetic cutoff, the particle differential flux manifests a latitude dependence (called the latitude effect) for energies up to about 15 GeV at vertical incidence.

The solar activity influences the cosmic ray flux on Earth and the shape of the energy spectrum up to about 100 GeV/nucleon in various ways. Primary radiation are subject to variations due to solar modulation effects. Periodic variation that follows the 11 year solar cycle have been measured. Stochastic and relatively sudden drop of the cosmic ray intensity, followed by a gradual recovery to the previous average intensity, are the so-called Forbush decreases, which are caused by magnetic shocks of solar origin. Occasional transient high energy phenomena on the Sun, caused by solar flares ejecting relativistic particles, are responsible for the ground level enhancement (GLE) that provoke an increase of the intensity of the cosmic radiation (10% to a few 100%) due to the arrival of a superimposed low energy particle component.

1.3.2 Temporal variations

In addition to the geomagnetic and heliospheric variations presented above, some of the intensity variations observed at sea level are seasonal and due to atmospheric effects caused by temperature and pressure changes affecting the mass thickness of the atmosphere. Seasonal variation of the cosmic muon differential flux at sea level can be as high as 20% [7].

The fractional change of integral muon flux, $\Delta\Phi_\mu/\Phi_\mu$, as a function of the atmospheric pressure variation at sea level can be approximated by the expression

$$\Delta\Phi_\mu/\Phi_\mu = -\alpha_{\mu P}\,\Delta P\,, \tag{1.2}$$

where $\alpha_{\mu P}$ is the muonic pressure coefficient ($\alpha_{\mu P} \approx 1.61 \cdot 10^{-3}\,\mathrm{mbar}^{-1}$) and ΔP is the atmospheric pressure change [7, chapter 6.3.2]. The dependencies of muon flux as a function of the altitude of the main production layer of muons, and as a function of the temperature of the main production layer for pions are also discussed in the same paper. However, as we will see later, these dependencies are less evident since the change in atmospheric pressure alone can explain the change in muon flux very well.

For accurate measurements, the altitude and energy dependence of the coefficient $\alpha_{\mu P}$ must be properly included.

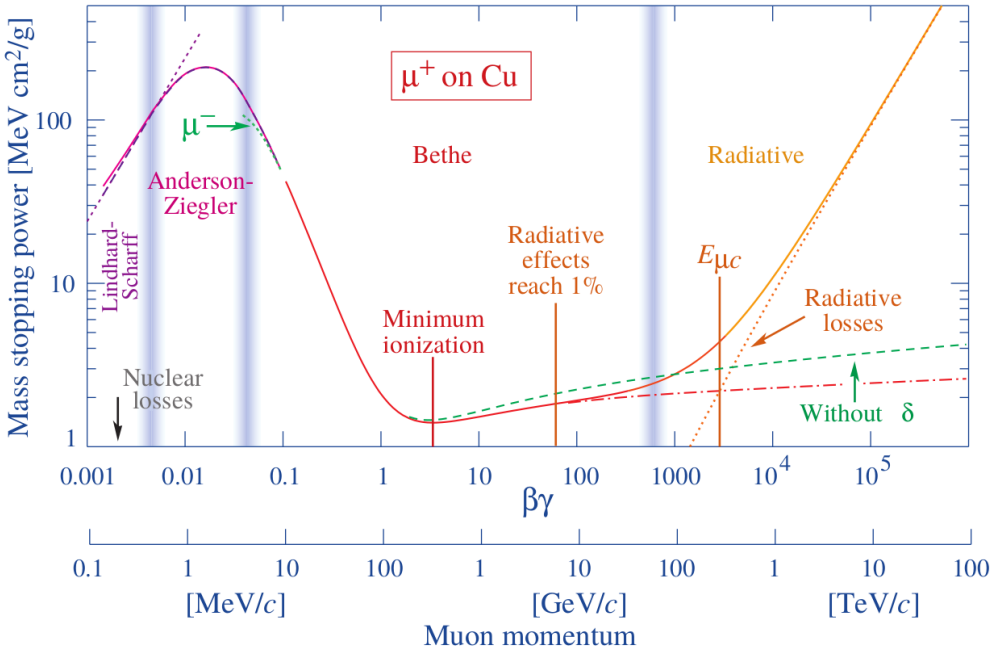

Figure 1.6: Mass stopping power of a positive muon in copper as a function of its momentum [5, chapter 33.2.3]. Solid curves indicate the total stopping power. The vertical bands delimit the regions where different approximations have been used.

1.4 Muon interaction with matter

1.4.1 Energy loss

Muons lose energy through atomic excitation, ionization and radiative processes such as bremsstrahlung, e^+e^- pair production and photonuclear interactions. Figure 1.6 shows the stopping power, defined as the energy loss per unit of crossed opacity, for a positive muon in copper [5, chapter 33.2.3]. The contributions due to the various physical processes are also highlighted.

Above a momentum of $10\,\mathrm{MeV}/c$ the muon stopping power can be parameterized as

$$-\frac{dE}{dX} = a(E) + b(E)E \tag{1.3}$$

where a is the energy loss due to excitation and ionization, while b is the fraction of energy lost due to the three radiative processes mentioned above and they both vary slightly with energy [5, 7].

The a parameter is given by the Bethe-Bloch formula

$$a(E) = -\left.\frac{dE}{dX}\right|_{\text{ion}} = Kz^2\frac{Z}{A}\frac{1}{\beta^2}\left[\frac{1}{2}\ln\frac{2m_ec^2\beta^2\gamma^2W_{\max}}{I^2} - \beta^2 - \frac{\delta}{2}\right], \tag{1.4}$$

where the constant K is equal to

$$K = 4\pi N_A r_e^2 m_e c^2 \approx 0.31\,\text{MeV}\,\text{mol}^{-1}\,\text{cm}^2,$$

I is the mean excitation energy, $W_{\max}$ is the maximum possible energy transfer to an electron in a single collision given by

$$W_{\max} = \frac{2m_ec^2\beta^2\gamma^2}{1 + 2\gamma m_e/M + (m_e/M)^2},$$

N_A is the Avogadro number, r_e is the classical electron radius, m_e is the mass of the electron, z, βc and M are the charge, velocity and mass of the incident particle, Z and A are the atomic number and mass number (expressed in $\text{g}\,\text{mol}^{-1}$) of the absorber and δ is the correction factor for the density effect [1]. Formula 1.4 describes the average stopping power for $0.1 \lesssim \beta\gamma \lesssim 1000$ for intermediate Z materials with an accuracy of a few percent.

The term b takes into account the radiative losses and can be written as a sum of contributions from bremsstrahlung, direct pair production, and photonuclear interactions as $b(E) = b_{br}(E) + b_{pp}(E) + b_{ni}(E)$. A detailed description of the calculation of these contributions is given in [10].

The stopping power functions are characterized by a rather large minimum zone (see figure 1.6) whose position ranges from $\beta\gamma = 3.5$ to 3.0 for Z ranging from 7 to 100. Most relativistic cosmic ray particles have stopping power close to the minimum: such particles are therefore called Minimum-Ionizing Particles (MIP). Typically a MIP has a stopping power from $1\,\text{MeV}\,\text{g}^{-1}\,\text{cm}^2$ to $2\,\text{MeV}\,\text{g}^{-1}\,\text{cm}^2$, that depends on the atomic number Z of the material it passes through.

At sufficiently high energies the radiation processes become predominant over ionization. The energy to which the two types of processes contribute equally is called critical energy, ϵ, and will be given by the relation $\epsilon = a(\epsilon)/b(\epsilon)$. As can be seen in figure 1.7, for muons crossing iron we have $\epsilon_\mu \approx 300\,\text{GeV}$.

The continuous-slowing-down-approximation (CSDA) range, $X(E)$ (expressed in $\text{g}\,\text{cm}^{-2}$), of a muon with initial energy E is obtained integrating the inverse of equation 1.3 as it follows:

$$X(E) = \int_{E_0}^{E} \left[a(E') + b(E')E'\right]^{-1}\, dE', \tag{1.5}$$

[1] As the energy of the particle becomes large, the absorber medium polarizes and it limits the extent of the electric field of the charged particle.

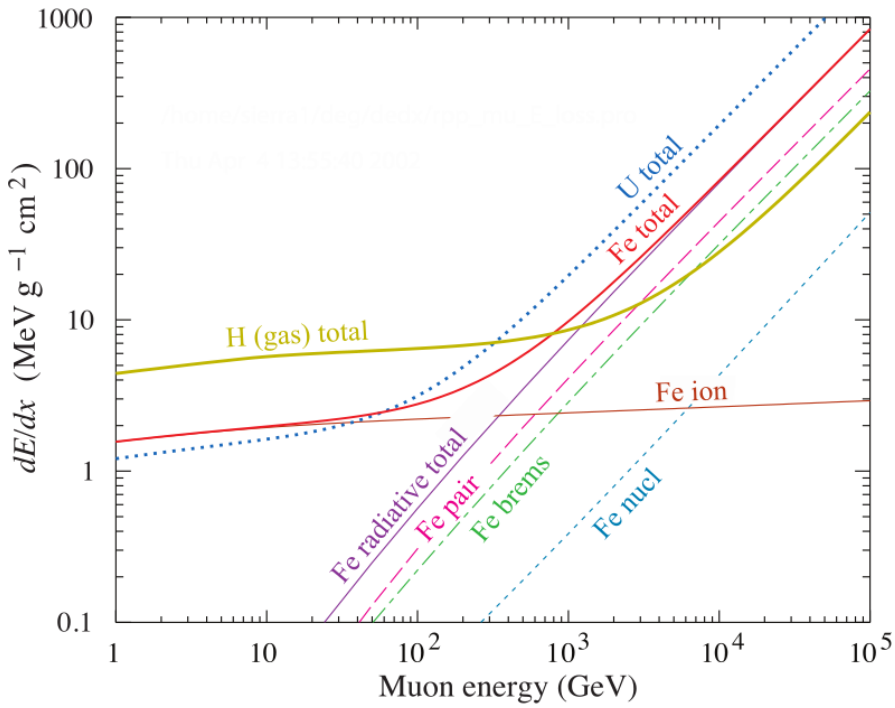

Figure 1.7: Average energy loss of a muon in hydrogen, iron and uranium as a function of the particle energy [5]. For iron, the various radiation contributions are highlighted.

where E_0 is sufficiently small that the result is insensitive to its exact value [10]. This calculation does not take into account the multiple scattering and rage struggling briefly discussed below. At very high energies, where a and b are (essentially) constant, the range formula simplifies to

$$X(E) = \frac{1}{b} \ln\left(1 + \frac{E}{\epsilon_\mu}\right). \tag{1.6}$$

Table 1.1 shows the range X (calculated according to equation 1.5) and the parameters a and b for muons through standard rock ($A = 22\,\mathrm{g\,mol^{-1}}$, $Z = 11$, $\rho = 2.65\,\mathrm{g/cm^3}$) for four different energy values. The data shown were obtained from [10]: in that work the contributions of stopping power and the CSDA range of muons are reported for a wide selection of elements, compounds, mixtures and biological materials for initial energies from 10 MeV to 100 TeV.

The range calculated with the CSDA approximation does not take into account fluctuations in energy loss and will generally correspond to the mean value of the range obtained for muons with initial energy E. The fractional

Table 1.1: Muon range and stopping power parameters calculated for a few energies in standard rock ($A = 22\,\mathrm{g\,mol^{-1}}$, $Z = 11$, $\rho = 2.65\,\mathrm{g/cm^3}$) [10].

E	X	a	b_{brems}	b_{pair}	b_{nucl}	b_{tot}
GeV	$10^5\,\mathrm{g\,cm^{-2}}$	$\mathrm{MeV\,g^{-1}\,cm^2}$	——	$10^{-6}\,\mathrm{g^{-1}\,cm^2}$		——
10	0.05	2.17	0.70	0.70	0.50	1.90
100	0.41	2.44	1.10	1.53	0.41	3.04
1000	2.45	2.68	1.44	2.07	0.41	3.92
10000	6.09	2.93	1.62	2.27	0.46	4.35

range straggling, defined as the ratio of the variance of the range to the range, in copper is around 2.8% to 5.7% from 10 MeV to 10 GeV [10].

Above 100 GeV straggling due to fluctuations in bremsstrahlung losses begins to dominate. Hard losses are indeed more probable in bremsstrahlung than in the other two radiative processes. In these cases it is useful to define the survival probability, $P_s(E, X)$, of a muon of energy E through an opacity X. Some studies of the survival probability of muons, usually handled by Monte Carlo simulations, are reported in [11]. Other references can be found in the description of figure 4.4 of [7]. In [12] the survival probabilities as a function of depth for muons from 1 TeV to 10^6 TeV are shown. The effects of the radiative tail are enormous: at 10^6 TeV only about 15% of the muons reach the CSDA range. At 10 TeV about half of them do, giving some indication of the usefulness of the CSDA ranges.

1.4.2 Multiple scattering

A charged particle passing through a medium is deflected by many small-angle scatter. For muons, the deflection is mainly due to Coulomb scattering from nuclei [5, chapter 33.3]. The overall deflection, if small, thanks to the central limit theorem is generally distributed according to a Gaussian (except for hard scatters that produce non-Gaussian tails). This Coulomb scattering distributions are well described by Molière's theory. Defining θ_0 as:

$$\theta_0 = \theta^{\mathrm{rms}}_{\mathrm{plane}} = \frac{1}{\sqrt{2}}\theta^{\mathrm{rms}}_{\mathrm{space}}\,,$$

where θ_{plane} is the angle of deviation projected on the plane (see figure 1.8) while θ_{space} is the total deflection angle in space, for most applications it is sufficient to use a Gaussian approximation for the distribution of the angle

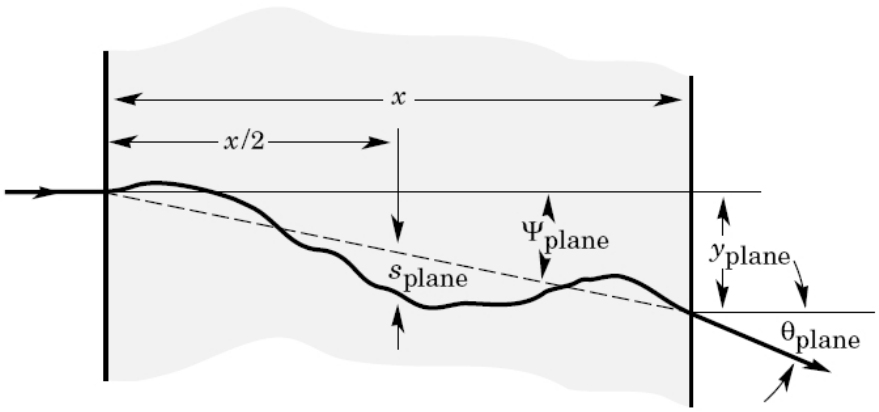

Figure 1.8: Physical quantities used to describe Coulomb multiple scattering [5, chapter 33.3]. The charged particle coming from the left impacts perpendicularly on the layer, and all the physical quantities of deflection are projected on the plane perpendicular to the direction of view.

θ_{plane}, with a standard deviation given by

$$\theta_0 = \frac{13.6\,\text{MeV}}{\beta c p}\, z \sqrt{\frac{X}{X_0}} \left[1 + 0.038 \ln\left(\frac{X z^2}{X_0 \beta^2}\right)\right]. \tag{1.7}$$

Here p, βc and z are the momentum, velocity and charge number of the incident particle, and X/X_0 is the thickness of the scattering medium in radiation lengths. The radiation length X_0, usually measured in $\text{g}\,\text{cm}^{-2}$, is the mean distance over which a high-energy electron loses all but $1/e$ of its energy by bremsstrahlung. The value provided by this formula describes the width θ_0 with an accuracy of less than 11% when $10^{-3} < X/X_0 < 100$. Figure 1.8 shows other quantities used to describe the Coulomb multiple scattering in the case of a charged particle impacting a layer of thickness x. In the figure the following quantities are defined:

- y_{plane} is the distance, projected on the plane, between the point from which the particle leaves the material and the line of incidence on the thickness;
- Ψ_{plane} is defined by the geometry as $\Psi_{\text{plane}} = \arctan \dfrac{y_{\text{plane}}}{x}$ (or in the approximation of small angles $\Psi_{\text{plane}} = \dfrac{y_{\text{plane}}}{x}$);
- s_{plane} is the distance, projected on the plane, between the position of the particle after passing through half the thickness and the midpoint between the entry and exit coordinates of the particle thickness.

For these quantities the following equations hold:

$$\Psi^{\text{rms}}_{\text{plane}} = \frac{1}{\sqrt{3}}\,\theta_0, \quad y^{\text{rms}}_{\text{plane}} = \frac{1}{\sqrt{3}}\,x\,\theta_0, \quad s^{\text{rms}}_{\text{plane}} = \frac{1}{4\sqrt{3}}\,x\,\theta_0. \tag{1.8}$$

The phenomenon of multiple scattering is not considered in the calculation of the muon range presented in paragraph 1.4.1, but this is a rather acceptable approximation. A measure of multiple scattering is provided by the detour factor [10], that is the ratio of the average penetration depth to the average path length for a stopping particle. The detour factor of a 10 MeV muon in uranium is 0.98 (it is one of the worst cases). This ratio increases rapidly toward unity as the energy is increased or if the atomic weight of the absorber is decreased.

1.5 Muography

The muon radiography technique, or muography, exploits the penetration capacity of muons present in cosmic rays to make radiographs of very large targets. As can be deduced from the data reported in table 1.1 on page 22, a 10 GeV muon on average is able to cross about 19 meters of standard rock before being stopped. Muography is a non-invasive technique since it exploits a natural radiation present on the entire surface of the earth.

There are mainly two muographic imaging techniques that are based on two different phenomena of interaction of muons in matter:

muon transmission radiography is based on the loss of energy of muons that will only be able to cross certain opacities based on their initial energy;

muon scattering tomography is based on measuring the deflection of muons in matter due to multiple Coulomb scattering.

As we will see better in paragraph 1.5.1, a small variant of muon transmission radiography is given by muon absorption radiography: in this case, through the use of a veto plane, the absorbed muons are measured instead of those transmitted through the target.

There is another technique that uses muons to study the metrology of structures. Taking advantage of the fact that muons, on average, travel in a straight line, the measurement of the tracks of muons that pass through several detectors allows us to study their relative displacements due to any deformation of the buildings in which they are installed [13].

All of these techniques relies on the detection of muon tracks by means of particle detectors called trackers. Some general reviews can be found in [9, 14, 15].

For the scattering tomography technique, and also in that of absorption radiography, the target must be placed between two detectors and this limits the size of the target itself. On the other hand, with the muon radiography technique for transmission, it is possible to study large and distant targets. However, scattering tomography provides more information and, in cases where it is possible to apply it, this reduces acquisition times.

In the next sections the operation of the two techniques and the areas of use are specified in more detail.

1.5.1 Transmission and absorption radiography

Muon transmission and muon absorption radiography are based on the energy loss (and the eventual decay) of muons when they interact with matter [5, chapter 34.2]. A muon with a given momentum $p_{\min}$, before being stopped, will be able to cross on average a certain opacity X. The relationship between muon momentum and average crossed opacity can be found tabulated in reference [10] and figure 3.3 on page 58 shows an example in the case of muons through standard rock. The higher the opacity of the target, the lower the number (and flux) of muons that have a momentum high enough to cross it. Fixed a certain angular direction (θ, φ) and a certain opacity, the expected value of the flux transmitted through the target can be estimated as the integral from $p_{\min}$ to infinity of the differential flux in that direction (more detailed formulas are shown in section 3.2.3).

For the transmission technique a single tracker is placed downstream the target to detect the transmitted muons, while for the absorption one the object under inspection is placed between the tracker and a veto plane (respectively above and below the target) to identify those muons that have been stopped within the target. Although the two techniques are similar, transmission muon radiography is the most common as it allows to examine very large objects.

The first applications of the technique dates back to the 1950s by Eric George to measure the depth of the overburden of a tunnel in Australia [16]. In the 1970's Luis Alvarez's team excluded the presence of a hidden chamber inside the Chefren pyramid [17]. Following in the footsteps of this pioneering measurement, more recently a hidden chamber inside the Cheops pyramid was discovered by the ScanPyramids collaboration [18]

Transmission muography sees its greatest development in the field of volcanology with research groups of various nationalities (Japanese, French and

Italian). [19–26]. This technique has proved to be particularly suitable in the field of volcanology because it allows to find information that would be inaccessible with the other techniques used (microgravimetry and georadar) allowing to study the targets at a safe distance. The first studies were able to provide a description of the internal architecture of volcanoes and afterwards dynamic studies have been carried out, demonstrating the possibility of monitoring volcanoes in real time so as to prevent the risks associated with an eruptive event.

Apart from volcanology and archaeology there are several other applications in the fields geology, mining and civil engineering. In the field of geology the technique has been employed to determine the shape of the bedrock underneath alpine glaciers in Switzerland [27], while there are numerous uses in the mining sector [28–32].

For all these types of applications the long acquisition time is the greatest limit of the technique and can vary from a few days to about a month. This will depend on the transmitted muon flux (which depends on the opacity of the target and the aiming angle), on the opacity contrast of the anomaly to be observed, and on the size of the detector.

1.5.2 Scattering tomography

The muon scattering tomography technique takes advantage of another phenomena: the deflection of muons from their straight trajectory due to multiple coulomb interactions [5, chapter 34.3]. The deflection angle has null average and depends on velocity and momentum of the particle, and on opacity and atomic number Z of the crossed material (see equation 1.7). The deflection of muons is particularly relevant for low momentum muons and it can constitute a not negligible background for the transmission (absorption) radiography [9]. In [33] a configuration similar to the transmission muography measurements that will be presented in this work was simulated: a muon radiography measurement with a detector placed below 50 m of standard rock. For this simulation an average multiple-scattering angle of 1.5° was obtained, which increases to 5° considering muons with final momentum less than 1 GeV/c.

Scattering tomography allows to directly reconstruct the density and the atomic number of the target by measuring the deflection of muons trough it. To do that two tracking detectors, one upstream and one downstream the target, are needed, thus limiting the size of the objects that can be studied (that is limited also by the fact that the technique is no longer sensitive when multiple deflections occur). Given the higher level of information obtained from these measurements , acquisition times are generally reduced (around a

few minutes) compared to transmission radiography. The first muon tomography measurement was performed at Los Alamos National Laboratory in 2003 [34], showing that the technique is particularly suitable to discriminate materials with an high atomic number, opening applications in the nuclear sector and in homeland security [35–42].

Chapter 2

The MIMA detector

The MIMA muon tracker (Muon Imaging for Mining and Archaeology), developed by the Florence INFN Unit and the Department of Physics and Astronomy of the University of Florence, has been designed to test the application of muography to various case studies, and to develop dedicated data analysis. The MIMA detector is a scaled-down version of the muon trackers developed for the "Mu-Ray" project [23] and the MURAVES experiment (MUon RAdiography of VESuvius) [43], even if, given its compactness, it has some peculiar hardware characteristics.

The MIMA tracker was designed as a light, rugged, low power muon detector. A complete and detailed description of the MIMA detector can be found in [33, 44, 45].

This detector was conceived as a portable apparatus to allow on-field tests of muon transmission radiography in different fields of application, following a multidisciplinary approach. After its construction, completed in the first half of 2017, it has been used for several different measurements [46].

The detector was at first installed in the Bourbon Gallery inside Mount Echia (Naples) where a complicated system of tunnels and cavities have been dug over many centuries, for the most varied purposes. On this site a test measurement was carried out with the Mu-Ray detector which had highlighted the possible presence of some unknown cavities [47]. Then two other measurements were carried out, another one with the Mu-Ray detector and one with the MIMA detector, validating the presence of a cavity by reconstructing its shape and position and highlighting additional empty unmapped volumes [48].

After this measurement, the detector has been used in the Tuscany region, mainly for investigating two possible fields of application: hydrogeological risk assessment and mining activity. In this second case, the detector was used to carry out muography measurements inside the Temperino mine

in Campigla Marittima in the province of Livorno. The results of these measurements were partly presented in [32, 33] and are the object of study of this work (see chapter 5).

In the hydrogeological field, studies of river banks were carried out to try to identify the burrows dug by animals to assess the damage and the associated risks [49]. In a similar context, the analysis of two measures carried out inside the inspection tunnel of an important dam in Tuscany are underway.

This chapter presents some details of the detector and of the analysis of single muographic measurements not presented in the aforementioned works. Furthermore, some aspects already present in the previous works will be defined again (detector structure, reference system, trigger configuration and track reconstruction) which are useful for an understanding of what follows.

2.1 Hardware

This section describes the detector structure, its operation and the external supporting mechanics. With reference to the external structure of the detector, a local reference system is defined, useful for illustrating the procedure for reconstructing the tracks, and a global one that allows to describe the position and direction of pointing of the detector. Then two reference systems are defined: a local one, which refers to the external structure of the detector and is useful for illustrating the procedure for reconstructing the tracks, and a global one that allows describing the position and pointing direction of the detector. Finally, the chosen trigger configuration is described, which in turn determines the geometric acceptance of the detector.

2.1.1 Detector structure

The MIMA detection system, shown in figure 2.1, is composed of six tracking planes, each of which assembled as an array of 21 scintillator strips with triangular section, read at both ends by silicon photomultiplier sensors (SiPM). Each plane has an active surface of $(40 \times 40)\,\mathrm{cm}^2$. The particular shape of the section of the strips allows the use of a barycenter algorithm for the reconstruction of the muon passage coordinates. This gives much better spatial resolution than what could be done using a digital algorithm.

Each plane is able to reconstruct one of the coordinates of a muon track. Planes measuring the same coordinate, at different heights, are part of the same view (X or Y). The six planes are then arranged in adjacent pairs to form three XY modules.

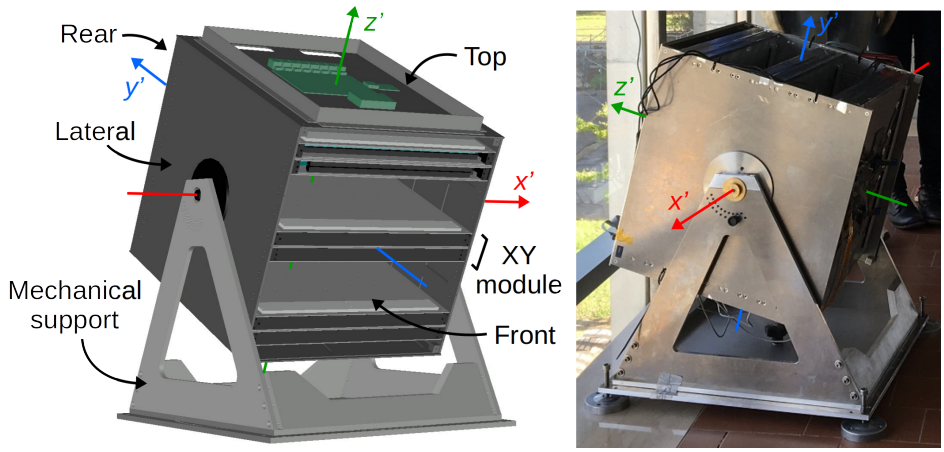

Figure 2.1: Structure of the MIMA detector. On the left an XY module is indicated, consisting of two tracking planes. Then the rotating support base and the faces of the external mechanics are highlighted. Both in the schematic drawing and in the photograph the local reference system, described in section 2.1.1, is shown: in the left image the detector points in a direction close to the vertical while in the one on the right it points in an almost horizontal direction.

The front-end electronics, the read-out circuits and the master board controlled by a Raspberry PI computer, have been inherited from the MURAVES experiment with few modifications.

The MIMA detector can be set in data taking mode by simply providing the power supply. An Ethernet line can be used for remote control and data quality check. The total power consumption is about 30 W, thus allowing the apparatus to be powered up using a small photo-voltaic system, if no mains electricity is available.

The tracking modules are housed in a protective aluminum box, a cube of side 50 cm, which defines the following six surfaces:

top the face on which the master board and the Raspberry are mounted. These devices are protected by an additional cap mounted on top.

bottom the face opposite to the top one.

two lateral these faces have two hubs that allow the detector to be rotated by means of a specific aiming mechanism.

front on this side, beyond the aluminum surface, all the connection cables between the slave boards and the master board are placed.

rear it is the opposite face to the front one and from this side, at the height of the master cap, the Ethernet cable and the power supply cables come out.

The tracking planes are numbered in ascending order from 1 to 6 going from the top to the bottom.

The MIMA detector is placed on an altazimuth mount, consisting of a fork arranged on a rotating horizontal platform, which allows the pointing direction of the detector to be varied. The MIMA detector is placed with the lateral hubs located in the appropriate slots of the fork. This mechanism allows one to vary the elevation of the telescope pointing direction. The elevation can be varied by rotating the detector in steps of 5° in one direction only, so that the front face is gradually turned downwards. Then the fork, together with the detector, can be rotated on the horizontal platform around the vertical axis. This allows one to vary the aiming azimuth. Finally, the base is equipped with four adjustable screw feet that allow one to correctly level the entire plane of the detector.

The opacity of the detector itself will influence the minimum momentum a muon requires to cross the detector. In the case a muon crosses all the detector, perpendicularly to the tracking planes, it will pass through 12 cm of polystyrene ($\rho = 1.06\,\mathrm{g/cm^3}$) and 1.8 cm of aluminum ($\rho = 3.97\,\mathrm{g/cm^3}$) that overall[1] corresponds to an opacity of $X_{\mathrm{MIMA}} = 17.6\,\mathrm{g\,cm^{-2}}$. The detector opacity doubles if we consider tracks that cross all six planes with an angle of incidence of 60° with respect to the normal to the planes. At the same time, as will be discussed in paragraph 2.1.2, muons crossing only two of the three tracking modules can also be detected. A particle of this type with a direction close to normal to the planes will have to pass through an opacity roughly equal to $\frac{2}{3}X_{\mathrm{MIMA}}$.

Local and global frames of reference

Referring to the detector structure presented above, we can define a local Cartesian coordinate system whose axes (x', y', z') will be aligned with the main axes of the mechanics and will have the origin positioned in the centroid of the detector sensors (see figure 2.1).The axes will be directed as follows:

x' axis parallel to the axis passing through the two hubs of the lateral faces and oriented in such a way as to form a right-handed triad with y' and

[1] As we will see in section 3.2.3, it is not that easy to calculate the overall opacity of a structure made up of multiple layers of different material, such as the MIMA tracker. In this case, given the reduced thickness of the detector, it would not have made much difference if we had considered it to be composed entirely of aluminum or polystyrene.

z';

y' axis perpendicular to the x' and z' axes and exiting from the rear face of the detector;

z' axis perpendicular to the tracking planes and upwards (along the direction from plane 6 to plane 1).

After defining the local reference system, it is necessary to define a global one to localize the detector and the target in space and to reconstruct the direction of the tracks of the detected muons, regardless of the specific pointing direction of MIMA. We therefore consider the Cartesian coordinate system whose axes (x, y, z) are directed as follows:

x axis towards the Geographic East;

y axis heading Geographic North;

z axis vertically.

In the case of a single muon radiography measurement the center of the reference frame will be placed again in the centroid of the detector sensors. The choice of the direction of the x and y axes is made in such a way as to be consistent with the UTM (Universal Transverse Mercator) coordinate system: this reference system, commonly used for geographic maps, divides the surface of the Earth into 60 zones and projects each of them on the plane to reconstruct their coordinates.

Given the choice made for the global reference frame and given the definitions of the counterclockwise zenith angle φ and that of the clockwise astronomical zenith angle φ_A reported in paragraph 1.1.1, the two angles are correlated from the equation $\varphi_A = 90° - \varphi$.

The following describes how to switch from the local to the global reference system (and vice versa) for a generic pointing direction of the detector. Consider initially the case in which the local reference frame coincides with the global one: this means that the detector will be pointed vertically with the front facing South. Starting from this configuration it is possible to vary the orientation of the detector (and therefore also of the local reference system) by modifying the elevation and azimuth of pointing through two rotations around the two axes of the supporting mechanics. While for a rigid body in space generally three angles of rotation must be defined to fix its orientation, for our telescope it is sufficient to adjust two of them: in fact, in every measure it is always required that the local x' axis is arranged horizontally, reducing by one the number of degrees of freedom of the system. This

condition is verified during all detector installations by means of a bull's eye level with a precision of about 0.3°.

Once the detector is aimed at will, we will define φ_{aim} as the angle from the x axis to the x' axis in an anticlockwise direction and θ_{aim} as the positive angle between the z and z' axes.

Let us consider a generic vector $\boldsymbol{r}' = (x', y', z')$ in the local reference frame. In the global coordinate system, the same vector will appear to have been rotated and will have coordinates $\boldsymbol{r} = (x, y, z)$ given by the following equation:

$$\boldsymbol{r} = R_z(\varphi_{\text{aim}})\, R_x(\theta_{\text{aim}})\boldsymbol{r}', \tag{2.1}$$

where R_x and R_z are the usual rotation matrices which can be expressed as:

$$R_x(\alpha) = \begin{pmatrix} 1 & 0 & 0 \\ 0 & \cos\alpha & -\sin\alpha \\ 0 & \sin\alpha & \cos\alpha \end{pmatrix}, \quad R_z(\alpha) = \begin{pmatrix} \cos\alpha & -\sin\alpha & 0 \\ \sin\alpha & \cos\alpha & 0 \\ 0 & 0 & 1 \end{pmatrix}.$$

By inverting equation 2.1 it is possible to obtain $\boldsymbol{r}'$ starting from $\boldsymbol{r}$ as follows:

$$\boldsymbol{r}' = R_x^{-1}(\theta_{\text{aim}})\, R_z^{-1}(\varphi_{\text{aim}})\boldsymbol{r} = R_x(-\theta_{\text{aim}})\, R_z(-\varphi_{\text{aim}})\boldsymbol{r}. \tag{2.2}$$

Through the equations 2.2 and 2.1 and also using the systems of equations 1.1 on page 7, that allows to pass from the Cartesian to the spherical coordinate system, it is possible to convert a generic direction (θ', φ') measured in the local reference system (for example the direction of a muon track) in the equivalent direction (θ, φ) seen in the global reference system and vice versa.

2.1.2 Trigger configuration

The trigger configuration was chosen in such a way as to reconstruct the track of those muons passing through any two modules. This means that a muon passing through all three modules or at least two modules (usually one of the external ones and the central one) can be detected. In this second case, only the minimum information necessary to reconstruct the muon track is available and it is not possible to determine the accuracy of the alignment of the reconstructed points, which is done for tracks that cross three planes of the same view. However, this choice of trigger has considerable advantages compared to the case in which a trigger signal was always required from all six planes of the tracker. In this way, in fact, it is possible to give an estimate of the efficiencies of the tracking planes and it is possible to increase the acceptance of the detector up to approximately 70° from the pointing direction

2.1.3 Geometrical factor and effective area

The coincidence counting frequency of any particle telescope, such as the MIMA tracker, depends upon the geometry of the active parts of the detector as well as the intensity of radiation and the sensor efficiencies. The experimentalist's task is to compute the intensity of radiation (which does not depend on the specific instrument in use) given the coincidence counting rate and the geometrical parameters of the telescope [50].

Taking inspiration from the formula of the counting rate of a generic telescope reported in [50], we get that the number of total muons N_{tot} detected from the MIMA detector will be given by:

$$N_{\text{tot}} = t_{\text{ACQ}} \int_{2\pi} d\Omega \int_{S(\Omega)} d\boldsymbol{\sigma} \cdot \hat{\mathbf{r}} \int_{p_{\text{MIMA}}}^{\infty} dp\, \phi(\Omega, p)\, \varepsilon \tag{2.3}$$

where t_{ACQ} is the total active acquisition time (with all the dead time subtracted), 2π is half of the total solid angle oriented in the pointing direction of the detector, $d\Omega = d\varphi\, d\theta\, \sin\theta$ is the element of the solid angle, Ω indicate the direction (θ, φ), $d\boldsymbol{\sigma}$ is the element of area of the central module, $\hat{\mathbf{r}}$ is the unit vector in direction Ω so that $d\boldsymbol{\sigma} \cdot \hat{\mathbf{r}}$ is the effective element of area looking into Ω, $S(\Omega)$ is the domain of $d\boldsymbol{\sigma}$ for tracks coming from direction Ω and it is limited by the other modules of the detector, p_{MIMA} is the threshold momentum given by the opacity of the detector itself and in principle it depends on both Ω and $d\boldsymbol{\sigma}$, p is the muon momentum, $\phi(\Omega, p)$ is the differential muon flux and ε is the global detector efficiency which in theory depends on all the integration variables. The choice to integrate the muon flux on the central module of MIMA is due to the fact that all the reconstructed tracks, both those passing through three modules and those crossing only two of them, must pass through the central one.

In particular, the equation 2.3 is valid after making the following assumptions:

1. $d\boldsymbol{\sigma}$ and $S(\Omega)$ are time independent, since the detector stands still;
2. the detector modules are mathematical surfaces with no thickness;
3. the muon trajectory is a straight line;
4. no muon decay occurs inside the detector;
5. the particle differential flux $\phi(\Omega, E)$ it is constant[2] and does not depend on the impact coordinate on the detector.

[2] We have seen in paragraph 1.3.2 that the free-sky muon flux has temporal dependencies (due for example to variations in atmospheric pressure) that we will neglect for this purpose.

After further assuming that both the detector efficiency, ε, and the threshold momentum p_{MIMA} are constant and independent of Ω and $d\boldsymbol{\sigma}$ (the validity of this second hypothesis is discussed in paragraph 3.2.3 on page 60), the equation 2.3 simplifies to:

$$N_{\mathrm{tot}} = t_{\mathrm{ACQ}}\,\varepsilon \int_{2\pi} d\Omega\, A_{\mathrm{eff}}(\Omega)\,\Phi(\Omega)\,, \tag{2.4}$$

where $A_{\mathrm{eff}}(\Omega)$ is the effective area pointing in the Ω direction and is defined as $A_{\mathrm{eff}}(\Omega) = \int_{S(\Omega)} d\boldsymbol{\sigma}\cdot\hat{\mathbf{r}}$. The calculation of the effective area, if performed in the local reference system of the detector, is simplified as follows:

$$A'_{\mathrm{eff}}(\Omega') = \int_{S'(\Omega')} d\boldsymbol{\sigma}'\cdot\hat{\mathbf{r}}' = \int_{S'(\Omega')} d\sigma'\cos\theta' = S'(\Omega')\cos\theta' \tag{2.5}$$

where the second equality is due to the fact that $d\boldsymbol{\sigma}'$ is parallel to the z' axis.

Let us consider the tracks coming from direction Ω' that have passed through at least two detector modules (according to the trigger coincidence condition): these tracks will also cross the central module within the portion of the surface $S'(\Omega')$. As shown in figure 2.2, after having translated the MIMA modules along the Ω' direction in such a way that all three are coplanar, the surface $S'(\Omega')$ will correspond to the overlapping area of at least two modules. From the figure 2.2 we obtain an analytical formulation for $S'(\Omega')$ given by the following equation:

$$S'(\Omega') = \begin{cases} 0, & \text{if } b_x < 0 \vee b_y < 0 \\ 2b_x b_y - (b_x - a_x)(b_y - a_y), & \text{if } b_x > \frac{L}{2} \wedge b_y > \frac{L}{2} \\ 2b_x b_y, & \text{otherwise} \end{cases} \tag{2.6}$$

where $b_i = L - a_i$ (with $i = x, y$), $a_x = d\tan\theta'|\cos\varphi'|$, and $a_y = d\tan\theta'|\sin\varphi'|$, $L = 40\,\mathrm{cm}$ is the side of the tracking planes and $d = 17\,\mathrm{cm}$ is the distance between two adjacent modules. The second and third cases of the previous equation correspond to the two examples shown in figure 2.2 (respectively the one on the left and the one on the right). In particular, the second case of equation 2.6 differs from the third for a term that corresponds to the hatched area in figure 2.2 which must not be counted twice.

Equation 2.4 can be written as

$$r_\mu = \int_{2\pi} d\Omega\, A_{\mathrm{eff}}(\Omega)\,\Phi(\Omega)\,,$$

where r_μ is the muon rate defined as $r_\mu = N_{\mathrm{tot}}/(\varepsilon\, t_{\mathrm{ACQ}})$. From the measurement of the integral muon flux presented in equation 3.5 on page 56 and using

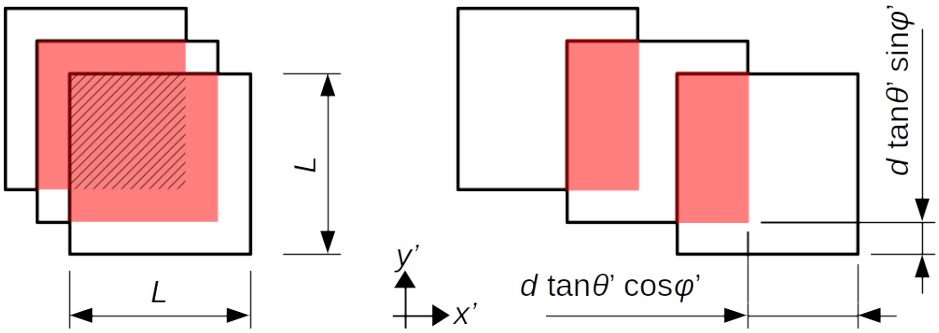

Figure 2.2: The schematic image shows the result of the translation of the MIMA modules in order to make them coplanar, for two different directions Ω' (the left image corresponds to a direction closer to the normal to the modules than the right one). The direction of view is along the z' axis. The area highlighted in red represents the surface $S'(\Omega')$, θ' and φ' are respectively the polar and azimuth angle corresponding to the direction Ω', L is the side of each tracking plane and d is the distance between two adjacent modules. For both cases, the surface S' is obtained by multiplying by two the overlapping area of the central module with only one of the external modules. For the left-hand case, however, it is also necessary to subtract the hatched area to avoid counting it twice.

the parameterization of the effective area from equation 2.5, the muon rate is estimated for a free-sky measurement with the detector pointed vertically, obtaining $r_\mu = 20\,\mathrm{Hz}$. This simulated value is slightly lower, but compatible as an order of magnitude, with the rate of particles actually measured under the conditions indicated above (about 24 Hz as reported in paragraph 2.2.6). In part this may be due to the presence of a low-energy electron background detected in the measurement and not simulated (see section 3.2.4) or to random coincidences, which could be relevant for tracks reconstructed from only four tracking planes.

In the hypothetical case in which the integral flux could be considered isotropic (which is not true), the previous equation would simplify in $r_\mu = G\,\Phi$, where G is the geometrical factor defined as

$$G = \int_{2\pi} d\Omega\, A_{\mathrm{eff}}(\Omega).$$

Using the parameterization of the effective area from equation 2.5, for the MIMA detector a geometrical factor of $G = 3.5 \cdot 10^3\,\mathrm{cm}^2\,\mathrm{sr}$ is calculated, which is greater than that reported in all the previous works ($G = 10^3\,\mathrm{cm}^2\,\mathrm{sr}$), since in that case only muons traversing all the three tracking modules were

considered.

2.2 Analysis procedures

This section briefly describes the analysis processes that can be applied to a measurement made with the MIMA detector, regardless of whether it was carried out in the free-sky configuration or with the detector pointed towards the target of interest. Initially, the reconstruction process of the muon tracks is described. Once this is done it is possible to equalize the gains of each channel and evaluate the inefficiencies of the tracking planes and of the detector. The effect of the variation in atmospheric pressure on the number of reconstructed tracks is then evaluated. Finally, after having reconstructed the angular distribution of the muon tracks, its dependence on the azimuth angle due to the East-West asymmetry is studied.

2.2.1 Track reconstruction

The muon track reconstruction procedure is described in detail in [33, 44] and briefly summarized below. The tracking algorithm is based on the reconstruction for each trigger event of the partial tracks in the X and Y view separately.

To reconstruct the partial track for the X view for each of the three plane, all the possible clusters are identified. A cluster is a group of adjacent strip on the same plane (usually one or two) with a signal above a certain threshold. Using a barycenter algorithm, the (x', z') coordinates of the clusters, which lie on the contact surface of the adjacent bars (see figure 6.3 in [44]), are reconstructed.

For each possible triad of clusters, one for each plane of the view, the residual on the central plane,$\Delta x'_{\text{res}}$, is evaluated. The residual is defined as the difference between the cluster coordinate of the central plane x'_2 minus the coordinate extrapolated from the clusters of the external planes. Since the clusters of the outer planes are equidistant along z' from the central plane, the residual will be calculated as[3]

$$\Delta x'_{\text{res}} = x'_2 - \frac{x'_1 + x'_3}{2}\,, \tag{2.7}$$

[3]Actually the algorithm for calculating the residuals also takes into account the coordinates z'_1, z'_2, z'_3 of the three clusters which will not be exactly equidistant in z' since, as previously mentioned, the cluster coordinates, (x', z') are reconstructed on surfaces with variable z'. However, formula 2.7 is a good approximation.

where x'_1, x'_2, and x'_3 are the x' coordinates of the clusters for the upper, middle, and lower planes.

If the absolute value of the residual is less than a certain threshold (i.e. the clusters are sufficiently aligned) there is a candidate partial track for the X view. If there is ambiguity between several partial tracks, the event is discarded. If there are no triples of clusters, an attempt is made to reconstruct the partial track with only two clusters of two different planes. In this case it is not possible to calculate the residual and in case there is an ambiguity (more than one pair of clusters possible) the event is discarded.

The partial track is reconstructed by a linear regression of the coordinates of the triad of clusters (or of the pair of clusters). In this way we obtain the passage coordinate on the plane $z' = 0$, x'_0, and the angle, $\alpha_{x'}$, that the partial track forms with the z' axis ($\tan\alpha_{x'} = \frac{\partial x'}{\partial z'}$).

Then the same procedure is repeated for the Y view. Combining the two partial tracks you get the overall track.

2.2.2 Equalization of gains

In this section a procedure is presented which simplifies the evaluation of the gains of each channel already presented in [44] and which therefore allows to improve the spatial (and therefore also the angular) resolution of the detector. This procedure is performed after calculating the muon tracks and, after the equalization, the tracks are recalculated.

Consider for example two adjacent scintillator strips (A and B) belonging to the X view with coordinates of the central vertices x'_A and x'_B ($x'_B - x'_A = l = 2\,\mathrm{cm}$). Let us consider tracks of muons that cross the two strips in a direction perpendicular to the x' axis ($\alpha_{x'} \approx 0°$) at the point of coordinate x' ($x'_A \leq x' \leq x'_B$). A schematic drawing of the geometry is shown in figure 2.3.

On average, the signal released for each channel ($\tilde{S}_A$ and $\tilde{S}_B$) will be proportional to the traversal length of the track inside the scintillator by means of a gain factor, G. Given the geometry of the scintillator strip, on average:

$$\tilde{S}_A = G_A(x'_B - x')/\cos\alpha_{y'},$$
$$\tilde{S}_B = G_B(x' - x'_A)/\cos\alpha_{y'}.$$

The two channels will be characterized by two different gains, G_A and G_B, which will depend on various factors (the optical quality of the scintillator and its surfaces, the optical coupling with the SiPM, the gain of the SiPM, the electronics, etc.). The signal S is defined as $S = \tilde{S}\cos\alpha_{y'}$ and the sum

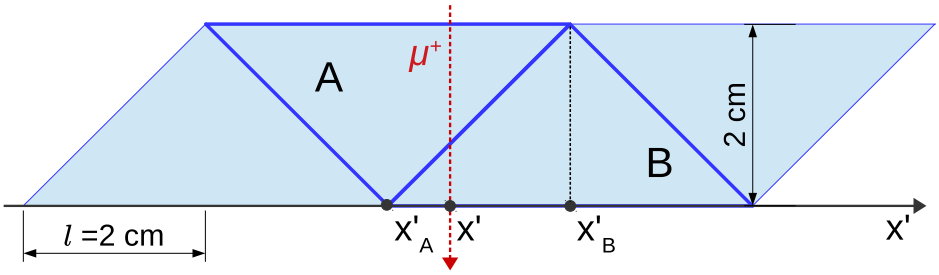

Figure 2.3: Schematic geometry of the configuration described in the text. Four adjacent strips are seen in section. In particular, we consider strips A and B which have a central vertex with coordinates x'_A and x'_B. The track of a muon passing through x' in a direction perpendicular to the x' axis ($\alpha_{x'} \approx 0°$) is shown in red.

signal, S_{tot}, as

$$S_{\text{tot}} = S_A + S_B = G_A x'_B - G_B x'_A + x(G_B - G_A).$$

Consequently we will have that $S_{\text{tot}}(x' = x'_A) = G_A\, l$ and $S_{\text{tot}}(x' = x'_B) = G_B\, l$ and the sum signal, S_{tot}, if G_A is different from G_B, depends on x'.

This is what can be observed in figure 2.4a, where, for each reconstructed track with $\alpha_{x'} \approx 0°$, the scatter plot of S_{tot} and x' is reported. This and most of the images below were made with ROOT, a data analysis framework commonly used in high-energy physics [51]. Unlike what previously discussed, this image shows the distribution of the S_{tot} signal for all 20 pairs of adjacent strips. The distribution of the S_{tot} signal is very large due to the fluctuations of the energy loss process in the scintillator. However, by averaging the S_{tot} signal for each bin in x', the points with measurement errors in blue are obtained. As expected, these points have a trend that is proportional to x' and the linear fit in red (the lines have been shifted up of 10 AU to better show the blue points) provides a measure of the ratio of the gains of the adjacent channels.

Once the signal of each channel has been divided by its own gain and repeating the previous procedure, we obtain the graph in figure 2.4b. Now the distribution of the S_{tot} signal, taking each pair of adjacent strips individually, no longer depends on the x' coordinate. Some pairs of strips still have a slightly higher signal but this can be justified by assuming that the two relative scintillator bars are slightly closer than normal and therefore slightly more overlapping. Vice versa if the S_{tot} signal is lower. To justify these variations, it is sufficient to shift the vertices of the bars of about 1.5 mm, which is absolutely plausible (but as we will see relevant if compared to the

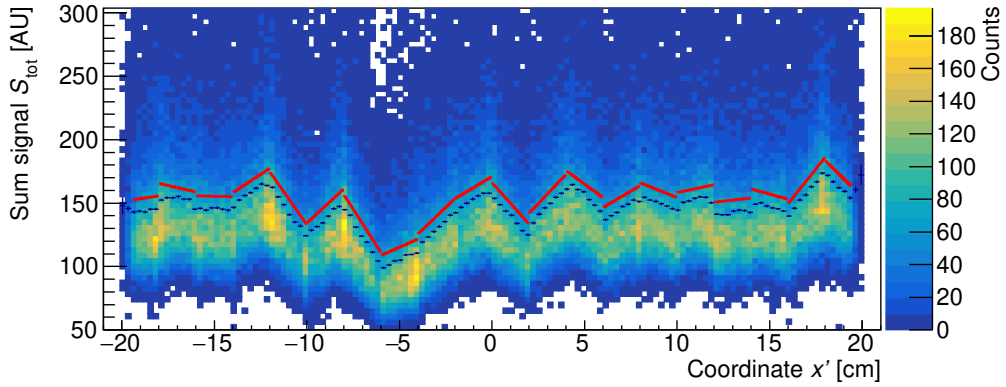

(a) No gain equalization.

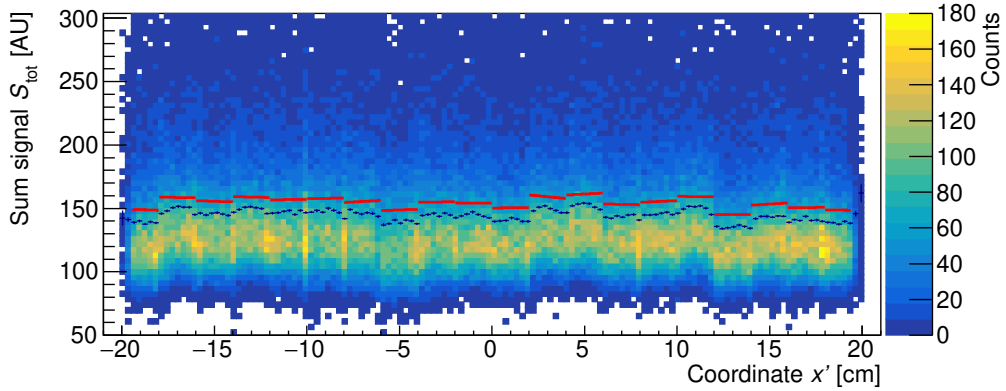

(b) With gain equalization.

Figure 2.4: Scatter plot of the sum signal, S_{tot}, and of the passage coordinate of the track, x', for $|\tan\alpha_{x'}| < 0.01$. Dots with error bars indicate the mean value of S_{tot} for each bin in x'. The red lines show the linear fit of the mean value of S_{tot} for each pair of adjacent strips. The fitted function has been shifted up by 10 AU to allow the display of the average S_{tot} values. Figure (a) shows the result assuming that all channels have unity gain, while figure (b) is obtained after equalizing the gains.

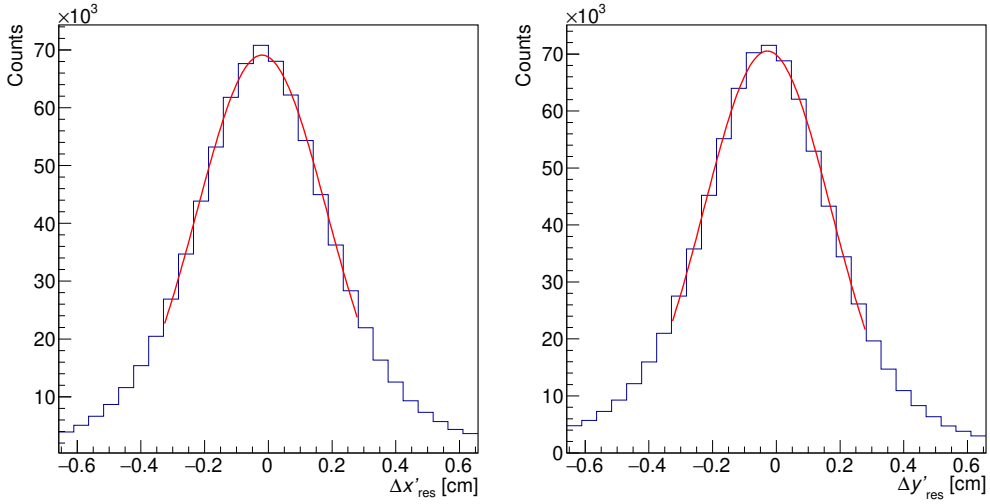

(a) X view: $\sigma_{x,\mathrm{res}} = 2.05\,\mathrm{mm}$ (b) Y view: $\sigma_{y,\mathrm{res}} = 2.0\,\mathrm{mm}$

Figure 2.5: Distribution of the residuals ($\Delta x'_{\mathrm{res}}$ and $\Delta y'_{\mathrm{res}}$) for the two views. The histograms are fitted with Gaussian distributions whose sigma is shown in the description.

spatial resolution). The same procedure is then automatically applied to the other tracking planes.

Thanks to this correction and other software and hardware improvements of the detector it was possible to refine the spatial and angular resolution of the instrument.

2.2.3 Detector resolution and multiple scattering

The spatial resolution of the detector can be determined from the distribution of the residual, $\Delta x'_{\mathrm{res}}$. From the propagation of the error applied to formula 2.7, we obtain that the measurement error on the residual, $\sigma_{x,\mathrm{res}}$, is equal to

$$\sigma^2_{x,\mathrm{res}} = \sigma^2_x \left(1 + \frac{1}{4} + \frac{1}{4}\right) = \frac{3}{2}\sigma^2_x, \tag{2.8}$$

where σ_x is the spatial resolution of the tracking planes of the X view, i.e. the measurement error on x'_1, x'_2 and x'_3. Inverting the previous equation we obtain that $\sigma_x = \sqrt{2/3}\,\sigma_{x,\mathrm{res}}$. Similar equations hold for the Y view.

Figure 2.5 shows the distributions of residuals for the X view and for the Y view, obtained by considering tracks that crossed all three modules. From the Gaussian fit of the two distributions we obtain that $\sigma_{x,\mathrm{res}} \approx \sigma_{y,\mathrm{res}} \approx 2.0\,\mathrm{mm}$.

From these it can therefore be deduced the spatial resolution of each plane in the two views: $\sigma_x \approx \sigma_y \approx 1.6\,\mathrm{mm}$.

As shown in [44], the angular resolution obtained for each partial track of the two views is given by $\sigma_{\alpha,x} = \sqrt{2}\,\sigma_x/D$ (and the analogue for y) where $D = 34\,\mathrm{cm}$ is the distance between two external tracking modules. In conclusion we get $\sigma_{\alpha,x} \approx \sigma_{\alpha,y} \approx 6.7\,\mathrm{mrad}$.

The improvement obtained, due to the optimization of the track reconstruction algorithms, is evident if we consider that in all the previous works worse resolutions are reported: $\sigma_{x,y} = 3.3\,\mathrm{mm}$ and $\sigma_{\alpha,x,y} = 14\,\mathrm{mrad}$.

Being more precise, the angular resolution of the detector is limited by the multiple scattering of muons in the planes of the detector itself. The multiple scattering angle has a zero mean and a root mean square value, θ_0, which depends on the number of crossed planes, on the propagation direction, and on the particle momentum as expressed in formula 1.7 on page 23. The angle θ_0 for muons crossing a single module in a direction perpendicular to the tracking planes is evaluated below.

Each module, as described in [44], is composed of layers of aluminum ($l_A = 8\,\mathrm{mm}$; $\rho_A = 2.7\,\mathrm{g/cm^3}$) and a polystyrene-based scintillator ($l_P = 4\,\mathrm{cm}$; $\rho_P = 1.06\,\mathrm{g/cm^3}$). The two materials have radiation lengths, X_0, respectively equal to $X_{0A} = 24.01\,\mathrm{g/cm^2}$ and $X_{0P} = 43.79\,\mathrm{g/cm^2}$. As reported in formula 34.27 of [5, chapter 34.4], the radiation length, X_0, in a compound material may be approximated by

$$1/X_0 = \sum_i w_i/X_{0i}, \tag{2.9}$$

where w_i and X_{0i} are the fraction by weight and the radiation length for the ith element. The weight fraction of the ith element is given by $w_i = X_i/X$, where X_i is the opacity of the ith element and X is the total opacity ($X = \sum_i X_i$). Substituting the definition of w_i into equation 2.9 we obtain the equation $X/X_0 = \sum_i X_i/X_{0i}$, useful for evaluating equation 1.7 for a muon through a tracker module. Substituting the values given above, for a single module we therefore obtain $X/X_0 = 0.187$.

Now it is possible to evaluate the angle $\theta_0(p)$ as a function of the muon momentum, p, using formula 1.7. To estimate an average value for the multiple scattering angle for a free-sky measurement, θ_{MS}, the following formula is used

$$\theta_{\mathrm{MS}} = \frac{\int_{p_{\mathrm{MIMA}}}^{\infty} dp\,\theta_0(p)\,\phi_V(p)}{\int_{p_{\mathrm{MIMA}}}^{\infty} dp\,\phi_V(p)} \approx 6.4\,\mathrm{mrad},$$

where $\phi_V(p)$ is the differential spectrum of muons in the vertical direction whose measurement is described in paragraph 3.2.1 and p_{MIMA} is the threshold momentum given by the opacity of the detector itself.

On page 55 of [44], it is shown that the root mean square of the multiple scattering angle trough the whole detector is due to the scattering on the first two modules of the tracker and is equal to $\frac{\sqrt{5}}{2}\theta_{\mathrm{MS}} \approx 7.2\,\mathrm{mrad}$. It is obtained that the overall contribution of multiple scattering is greater than the angular resolution of the detector ($\sigma_{\alpha,x,y} = 6.7\,\mathrm{mrad}$) and therefore it is not necessary to further refine the muon track reconstruction algorithms while it could be useful to decrease the opacity of the detector thus reducing the effect of multiple scattering.

Moreover, given the effect of multiple scattering, the spatial resolution (and therefore also the angular resolution) of the detector is better than that estimated above. In fact, the residual measurement uncertainty, $\sigma_{\mathrm{res}} \approx 2.0\,\mathrm{mm}$, includes the effect of the multiple scattering on the central module of the tracker [4] , $\sigma_{\mathrm{res,MS}}$. This term can be estimated as

$$\sigma_{\mathrm{res,MS}} = \frac{D}{4}\tan\theta_{\mathrm{MS}} \approx 0.5\,\mathrm{mm},$$

and must be subtracted in quadrature from the previously obtained value for the residual measurement uncertainty, obtaining the new value $\sigma_{\mathrm{res}} \approx 1.94\,\mathrm{mm}$. Consequently, the spatial resolution also improves slightly.

2.2.4 Detector efficiency

The detection efficiency of the tracker will be defined as the probability that a muon that has fully crossed at least two modules of the tracker is actually detected. This efficiency will depend on the number of planes traversed: by way of example, let's consider the simplified case obtained by reporting in a two-dimensional space the calculation of the efficiencies for the MIMA detector as shown in figure 2.6. In particular, we want to calculate the efficiency of the detector for the tracks that pass through the two lower modules (type A) and for those that cross all the tracking planes (type B). Each planes will be characterized by its own efficiency ε_i with $i = 1, 2, 3$. Since to detect the particle and reconstruct its track it is sufficient to measure at least two impact points, the detector efficiencies for the two types of tracks are equal to:

$$\begin{aligned}
\varepsilon_A &= \varepsilon_2\varepsilon_3 \\
\varepsilon_B &= \varepsilon_1\varepsilon_2\varepsilon_3 + (1-\varepsilon_1)\varepsilon_2\varepsilon_3 + \varepsilon_1(1-\varepsilon_2)\varepsilon_3 + \varepsilon_1\varepsilon_2(1-\varepsilon_3) > \varepsilon_A
\end{aligned}$$

[4] The effect of multiple scattering on the first module of the tracker limits the correct reconstruction of the muon track, but does not influence the measurement of the residual, $\Delta x'_{\mathrm{res}}$.

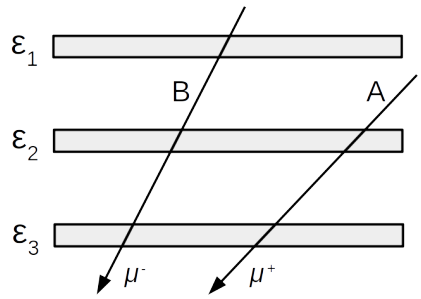

Figure 2.6: Two-dimensional schematic representation for the calculation of the detector efficiencies for two different types of track. In case A the track intercepts only the lower planes while in case B the particle crosses all three planes. The values of the efficiencies are indicated alongside each plane.

It is worth noting that the detection efficiency for the tracks of type B is higher than that for type A, thanks to the use of an additional tracking plane. In the real three-dimensional case, the efficiency of the detector will still be given by the sum of the product of the efficiencies and inefficiencies of the planes crossed by the particle. In addition, the efficiency of each plane ε_i will not be constant but will depend precisely on the coordinate of the impact point and, to a lesser extent, on the inclination of the track (due to the release of energy in each scintillator). The exact calculation of the detector efficiency should be part of the analysis of the muographic data, however, this calculation is complicated by the non-trivial case studies obtained by correctly schematizing the problem in three dimensions. For this reason, for the muography analysis carried out with the MIMA detector, we limited ourselves to evaluating the detection efficiencies of each tracking plane, so as to be able to possibly discard the data associated with malfunctions highlighted by an evident reduction of one of those efficiencies. Once we checked that the data were free of these anomalies it was assumed that the overall efficiency of the detector was constant and equal to one.

The detection efficiency of the ith plane (with $i = 1, 2, \ldots, 6$) was evaluated by considering the subset of events that satisfy the following conditions:

- the other five planes revealed the particle;
- the reconstructed track intersects the median plane of the ith plane at a distance greater than 2 cm from the edge.

This second condition was imposed to avoid underestimating the efficiency: consider for example a muon that intersects the first five planes of the detector and whose reconstructed tracks impacts the last plane in a marginal way

Table 2.1: The table shows the inefficiencies of the tracking planes, multiplied by a factor of 10^4, with the detector pointing upwards and downwards respectively. The inefficiency error was calculated as the square root of the variance of the inefficiency as presented in [52]. It can be observed that the reported values remain substantially unchanged in the two cases except for the external planes of the detector.

	$(1-\varepsilon_i)\cdot 10^4$	
i	Upwards	Downwards
1	16.0 ± 1.3	44.7 ± 1.1
2	0.80 ± 0.03	5.5 ± 0.4
3	13.9 ± 1.2	11.5 ± 0.6
4	1.4 ± 0.4	0.94 ± 0.17
5	3.7 ± 0.6	2.3 ± 0.3
6	49 ± 2	21.9 ± 0.8

(near the edge of the plane itself). Due to the multiple scattering in the penultimate plane, the particle could be deflected out of the detector and this event would be mistaken for an inefficiency of the lowest plane.

The efficiency ε_i was calculated as the ratio between the number of times that the ith plane revealed the passage of the muon and the total number of events of the previously defined set. Typically, to check the correct functioning of the detector, it is possible to study the graph of the efficiencies of the various planes as a function of the number of files (currently each file contains the data relating to 1000 trigger events) in order to identify any evident reductions in the efficiency value. In this case, for simplicity, the values of the global inefficiencies $(1-\varepsilon_i)$ multiplied by a factor of 10^3 are shown in table 2.1. As you can see from the second column, which refers to a standard acquisition with the detector pointed vertically, the plane efficiencies are all close to one and the plane number 6, the lowest one in this case, is the one with the greatest inefficiency (about $5 \cdot 10^{-3}$). However, this value could be overestimated due to some false inefficiency events: an example can be given by those events in which a low energy muon, with momentum close to the threshold momentum of the detector itself (see paragraph 3.2.3 on page 60), coming from above the detector, is fully stopped after passing through the first five tracking planes. In this case this event would be wrongly interpreted as an inefficiency of the last plane. To verify this hypothesis, the measurement was repeated by overturning the detector (see the data shown in the right column) and an increase in the efficiency of plane 6 and a corresponding decrease in that of plane 1 was correctly observed.

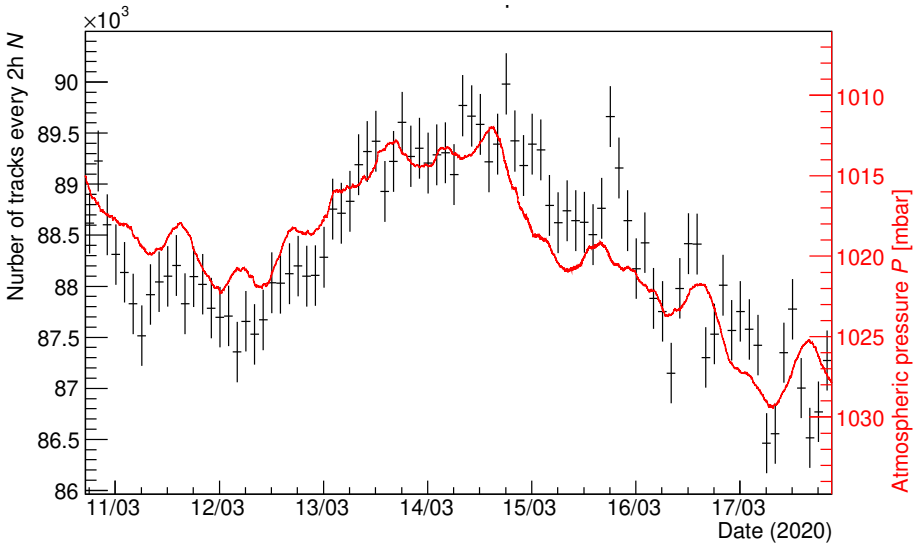

Figure 2.7: The graph shows the anticorrelation between the number of detected muons (black points with error bars), in this case at intervals of two hours, and atmospheric pressure (red line) for a free-sky measurement. The pressure axis on the right is upside down. Although in this measure the detector was directed vertically, the muon rate does not match with what was seen previously (around 20 Hz) because a tracking plane was not working.

2.2.5 Atmospheric pressure variation

As described in section 1.3.2 on page 18, the flux of cosmic rays can vary, not only due to magnetic phenomena, but also due to atmospheric effects that influence the thickness of the atmosphere. For low energies the most evident effect is linked to the variation of atmospheric pressure.

Figure 2.7 shows the variation of the muon flux detected by MIMA for a free sky measurement. The points with error in black correspond to the number of tracks reconstructed every two hours, N, while the graph in red indicates the atmospheric pressure, P. The measurement of the atmospheric pressure, as well as the ambient temperature, is carried out by means of an Enviro board connected to a dedicated Raspberry Pi [53]. From figure 2.7 it is possible to observe the anticorrelation between the number of identified particles and the atmospheric pressure (the red pressure axis is reversed).

To better fit the two graphs and quantitatively evaluate the relationship between the pressure and the number of detected muons, a linear regression was performed, as reported in figure 2.8. From the reduced Chi-square value and from the graph of figure 2.7 it is however observed that there will be residual dependencies of the muon flux from other environmental variables

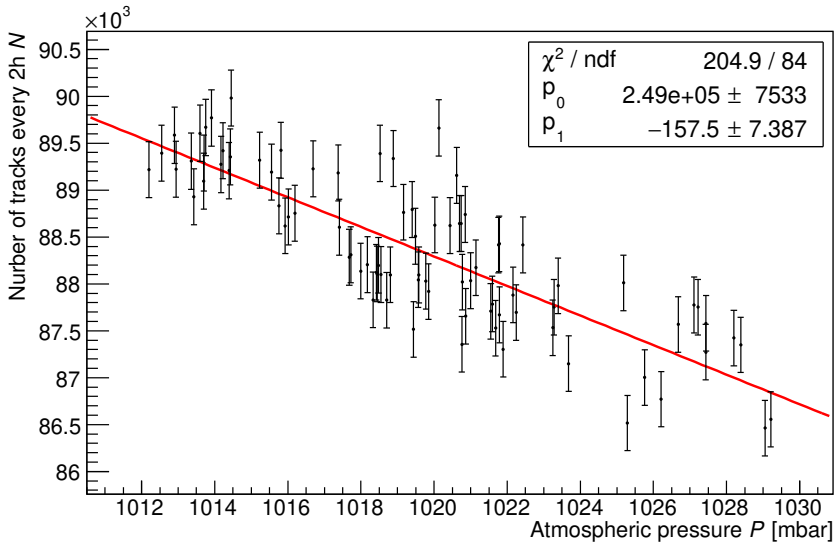

Figure 2.8: The result of the linear regression of the number of tracks detected every two hours, N, is shown as a function of atmospheric pressure, P. The function used for the fit is: $N = p_0 + p_1 \cdot P$. To calculate the parameter $\alpha_{\mu P}$, the parameters $\frac{\Delta N}{\Delta P} = p_1 = -157.5\,\mathrm{mbar}^{-1}$ and $N = \bar{N} = 88354$ are used.

as discussed in paragraph 1.3.2.

From equation 1.2 we have that the muon pressure coefficient, $\alpha_{\mu P}$, can be calculated as

$$\alpha_{\mu P} = -\frac{\Delta\Phi_\mu}{\Phi_\mu}\frac{1}{\Delta P} = -\frac{\Delta N}{N}\frac{1}{\Delta P}\,.$$

Using the parameters obtained from the previous linear regression we get a measure of the aforementioned coefficient of $\alpha_{\mu P} \approx 1.78 \cdot 10^{-3}\,\mathrm{mbar}^{-1}$ which is in excellent agreement with the value reported in the literature ($\alpha_{\mu P} \approx 1.61 \cdot 10^{-3}\,\mathrm{mbar}^{-1}$).

The dependence of the integral muon flux as a function of atmospheric pressure decreases as the energy of the particles increases and for this reason the same correlation is not observed in the case of measurements in which the detector is shielded by a thick target. Given the above, in order to compare flux measurements made at different times, especially if in the open air, it is necessary to normalize the measured flux to a nominal pressure value.

2.2.6 Track angular distribution

Once the muon tracks have been reconstructed, it is possible to compute their angular distribution. The number of tracks detected in a solid angle $d\Omega$

around direction (θ, φ), $N(\theta, \varphi)$, are obtained by differentiating equation 2.4 and will be equal to:

$$N(\theta, \varphi) = t_{\mathrm{ACQ}}\, \varepsilon\, A_{\mathrm{eff}}(\theta, \varphi)\, \Phi_M(\theta, \varphi)\, d\Omega \tag{2.10}$$

where t_{ACQ} is the active acquisition time (with the dead time subtracted), ε is the detector efficiency, $A_{\mathrm{eff}}(\theta, \varphi)$ is the effective area of the detector for direction (θ, φ) and $\Phi_M(\theta, \varphi)$ is the measured integral flux in the same direction. Remember that the angles (θ, φ) are respectively the polar angle and the zenith angle defined in paragraph 1.1.1.

To properly represent the angular distribution of the number of reconstructed tracks (along with all the other quantities measured with a single muographical measurement) we first have to define and choose an angular frame of reference. In the muography research group of Florence usually two possible reference systems are used (they are both Cartesian coordinate systems):

zenithal the abscissa is represented by the clockwise azimuth φ_A ($\varphi_A = 90° - \varphi$) and the ordinate is given by the elevation α_E ($\alpha_E = 90° - \theta$);

polar the abscissa is given by $\theta \cos \varphi$ and the ordinate equals $\theta \sin \varphi$ where θ is expressed in degrees.

In the polar reference frame the zenith angle, θ, represents the distance from the center of the map[5] (the center corresponds to the vertical direction) and the azimuth angle, φ, is the counterclockwise angle from the East pointing to the right on the map. In this way, it is easier to maps that use this reference frame with the cartographic ones.

An example of those two reference frames is shown in figure 2.9. These are maps of the angular distribution of the number of tracks reconstructed for a free-sky measurement (without obstacles in front of the tracker) made at INFN in Florence. For this measurement the detector was pointed vertically with the front facing the magnetic North and the total acquisition time, without the contribution of the dead time, was approximately 15 d and 18 h, with an average particle rate of 24 Hz.

[5] A possible variant of the polar reference system is given by the Lambert azimuthal equal-area projection which is a particular mapping from a sphere to a disk. In this case the distance from the origin of the reference system is equal to $2 \sin \frac{\theta}{2}$. As the name implies, it is a mapping that preserves the area: regions on the map with equal areas correspond to solid angles of equal width. Using this type of projection, the calculation of the solid angle associated with each pixel, $d\Omega$, which can be useful for evaluating the formula 2.10, becomes trivial, while in the case of the polar reference system, numerical integrations must be used.

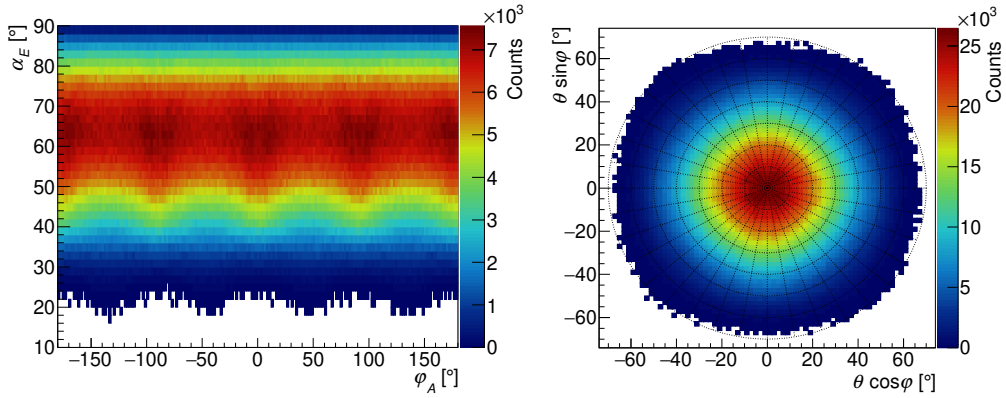

(a) Zenithal reference frame (b) Polar reference frame

Figure 2.9: Angular distribution of reconstructed muon tracks for the free-sky measurement pointed vertically with two different reference frames.

The zenithal reference frame is easily understood and looks similar to a photograph of the target when it is observed for small elevation angles. However, for directions close to the vertical, this reference system has some disadvantages. As can also be seen in figure 2.9a, the number of muon counts per pixel, beyond 60° of elevation, decreases as one approaches the vertical. This is because, as expressed by the formula 2.10, the number of muon counts is proportional to the solid angle $d\Omega$, and, since for the zenith reference system $d\Omega_Z = \sin\theta\, d\theta\, d\varphi$, we have that $d\Omega_Z(\theta = 0°) = 0$. For this reason the zenithal reference frame is preferable in case we are interested in muon radiography measurement pointing close to the horizontal direction (studies of volcanoes and river embankments) whilst the polar one has to be chosen when the detector is pointing close to the vertical direction. As we will see later, in this work the polar reference system was used since the measurements presented are directed vertically.

In both track distributions of figure 2.9 one can observe the decreasing in the number of the detected tracks for increasing the zenithal angle (decreasing the elevation angle). This effect is due to the fact that both the measured flux, Φ_M, and the effective area of the detector will decrease getting away respectively from the vertical direction and the detector pointing direction (which are the same for this specific case).

The reference systems presented have been defined in such a way as to be independent of the specific pointing direction of the detector. This allows you to compare these measurements with other geophysical surveys in a more direct way than would be possible with other reference systems. However, it

must be said that, since muography is a radiographic projection technique, the maps obtained from a single measurement must be interpreted based on the relative position of the detector with respect to the target in question.

2.2.7 East-West effect

As described in section 1.3.1 on page 17, East-West asymmetry manifests as an excess in the flux of cosmic rays from the West. This effect is relevant for particles with energy smaller than 10^2 GeV.

From the free-sky measurements made with the MIMA detector it is possible to highlight this effect. To do this, for each measurement, the map of the muon counts in polar coordinates was obtained. Then the left-right specular map was created, reflecting each track through the vertical aiming plane of equation $x' = 0$. From the ratio of the two previous maps, the polar map of the reflection ratio is obtained. Figure 2.10 shows the maps of the reflection ratio for four free-sky measurements with different aiming angles $(\theta_{\text{aim}}, \varphi_{\text{aim}})$. The white dashed lines indicate the symmetry axis of the maps, as well as the projection in polar coordinates of the reflection plane $x' = 0$.

All the maps highlight the effect of the East-West asymmetry by reporting values of the ratio greater than one towards the West or less than one towards the East. It can also be observed that this asymmetry is more evident for high zenith angles, where a 20% asymmetry is measured, while it becomes less relevant for directions close to the vertical.

A precise quantitative simulation of this asymmetry as a function of the momentum of the detected particles is rather complicated. For this reason, it is preferred to reduce this effect directly from free-sky measurements, so as to be able to neglect dependence of the muon flux on the azimuth angle. To do this, the free-sky measurements are symmetrized with respect to the plane $x' = 0$: the previously described reflection is applied to half of the reconstructed tracks.

The East-West asymmetry, given its dependence on the energy of the detected particles, will be negligible in muography measurements in which the detector is completely shielded by a thick target (as for measurements inside a mine) which will impose a momentum threshold such to reduce the asymmetry effects (see paragraph 3.2.3 on page 57 for the momentum-opacity relationship). More complicated is the case of measurements with thin targets or in which the open sky is partially visible. If on the one hand the symmetrization procedure strongly limits the dependence of the flux on the azimuth angle, on the other hand a bias will remain due to a global normalization factor: a free sky measurement facing West, even if symmetrized, detects a greater flux of particles of an eastward measurement.

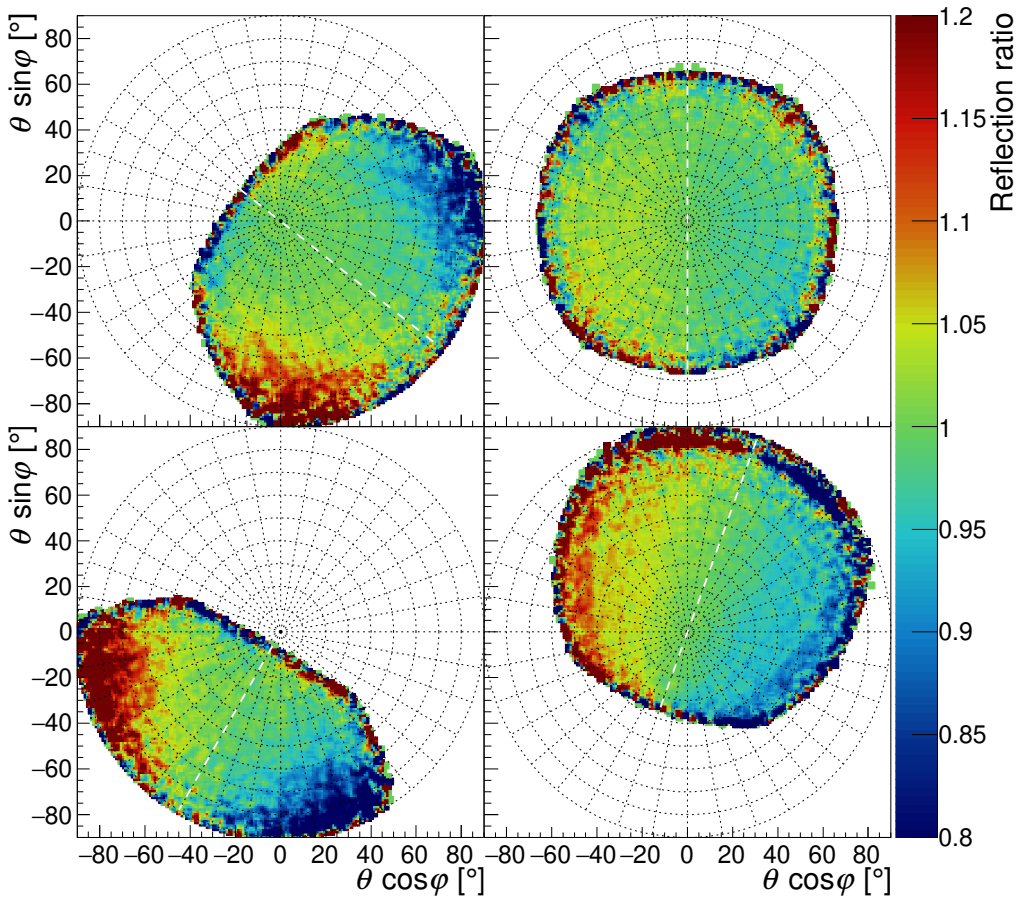

Figure 2.10: Reflection ratio maps (original map to reflected map) for four free-sky measurements with different aiming directions. The dashed white line corresponds to the polar projection of the reflection plane $x' = 0$. For each map, two points symmetrical with respect to the white line will have ratio values that are the inverse of each other.

Chapter 3

Muon transmission radiography

3.1 Transmission

To get any quantitative information from a muographical measurement we should transform the track distribution maps (presented in figure 2.9 for a free-sky measurement) in such a way to remove the dependencies from the specific characteristics of the detector in use, as expressed in equation 2.10. To pursuit this goal is necessary a detailed knowledge of the geometrical acceptance of the detector. An approximate analytical expression of the effective detector area in the local reference system, $A'_{\text{eff}}(\theta', \varphi')$, is provided by equations 2.5 and 2.6. To obtain the effective area in the global reference system, $A_{\text{eff}}(\theta, \varphi)$, it is necessary to convert the local measurement direction, (θ', φ'), to the equivalent direction in the global system as expressed at the end of section 2.1.1 on page 31.

To avoid borrowing with these studies is possible to perform a free-sky calibration measurement with the detector pointed in the same direction of the target measurement. In this way, two measures are used: one in front of the target to be studied and one in the open air without obstacles in the acceptance of the detector. Once done that, the muon measured transmission T_{M} for direction (θ, φ) can be defined as:

$$T_{\text{M}}(\theta, \varphi) = \frac{\Phi_{\text{M,tar}}(\theta, \varphi)}{\Phi_{\text{M,free}}(\theta, \varphi)} \tag{3.1}$$

where $\Phi_{\text{M,tar}}$ is the muon flux reaching the detector in the target configuration and $\Phi_{\text{M,free}}$ is the measured flux in the free-sky configuration. In this way the transmission can be interpreted as the probability for a muon to reach the detector from the direction (θ, φ) before crossing the target.

Taking into account equation 2.10, the measured transmission formula

can be rewritten as follows:

$$T_{\mathrm{M}}(\theta,\varphi) = \frac{N_{\mathrm{tar}}(\theta,\varphi)}{N_{\mathrm{free}}(\theta,\varphi)}\frac{t_{\mathrm{free}}}{t_{\mathrm{tar}}}, \tag{3.2}$$

where N_{tar} and N_{free} are the numbers of tracks detected in a solid angle $d\Omega$ around direction (θ,φ) for the target and for the free-sky configuration respectively and t_{tar} and t_{free} are the acquisition times (with dead time subtracted) for the two configurations. The above equation is valid assuming that:

- the efficiencies of the tracking planes have remained unchanged or in any case undergo negligible variations compared to other statistical errors involved. This is generally true if the detector is properly operating.

- the pointing direction of the detector has remained unchanged and consequently the term of effective area $A_{\mathrm{eff}}(\theta,\varphi)$ is simplified in the previous ratio. Even small rotations of the order of a degree can lead to non-negligible variations in the measured transparency [49].

Examples of transparency maps are given in section 5.2 for the measurements presented in this work.

It must be said that the use of a free-sky calibration measure and consequently the use of the transparency can lead to additional errors. Generally statistical errors are not a problem, as for free-sky measurements, given the much higher muon rate, a much higher statistic is generally obtained than for target configuration. However, there may be systematic errors caused by various effects. The first is the fact that often the two measurements (target and free-sky) cannot be carried out simultaneously. In this way it will be possible to have temporal variations of the muon flux (such as those indicated in sections 1.3.1 and 1.3.2 on page 18) which are different for the two measurements. In some experiments, including those at volcanoes, a portion of the sky is also visible in the target measurements and this allows to have a reference to perform an additional normalization. The same thing cannot be done for measurements made inside a mine, like those presented in this work.

Furthermore, there may be systematic effects due to variations in the low energy spectrum of muons that are present only in the free-sky measurement. This is for example the case of the East-West asymmetry, which can be partially mitigated by the symmetrization of the free-sky measurements as shown in section 2.2.7.

As a future development these and other effects can be simulated to try to limit systematic effects. In any case, the definition of the measured transparency is useful to limit any systematic effect that is present in equal measure in the target and in the free-sky configurations. For example, if a tracking plane had a low but constant efficiency, the measured transparency would not change.

3.2 Simulations

3.2.1 Experimental muon spectra

To correctly interpret the results of a measurement it is necessary to make a comparison with simulations based on the knowledge of the muon spectrum at ground level. In paragraph 1.3 on page 16 there are references to measurements and an analytical parameterization of the differential muon flux at sea level for $p_\mu > 10\,\mathrm{GeV}/c$.

At the muon radiography group in Florence, the simulation are based on muon spectra measurements made with the ADAMO magnetic spectrometer [54], prototype for the Pamela experiment [55]. With this instrument, measurements were made of the differential flux of cosmic muons for various values of the zenith angle, θ, and of the particle momentum, p, as shown in figure 3.1: the data collected are divided into 8 bins in the polar angle from 0° to 80° and in 15 equally spaced bins in the logarithm of the momentum with a momentum from $0.1\,\mathrm{GeV}/c$ to $130\,\mathrm{GeV}/c$. The use of these spectrum measurements has considerable advantages over those present in the literature. First of all, these measurements were made in Florence and therefore correctly describe the muon flux in regions with similar geographic (latitude, longitude and altitude) and geomagnetic characteristics. Furthermore, the measurements made with the ADAMO spectrometer extend for low values of the particle momentum and this is particularly useful for simulating measurements in the free-sky configuration or with thin targets.

To calculate the differential flux for each pair of values (p, θ) it is necessary to parameterize its dependence on these two variables[1]. Generalizing the formula for the proton spectrum given on page 114 of [56], given a certain zenith angle θ, the differential muon flux is parameterized as a function of the particle momentum as

$$\phi(p;\theta) = \phi(p;\boldsymbol{a}(\theta)) = a_0(p + a_1 e^{-a_2 p})^{-(a_3+a_4)} p^{a_4}. \tag{3.3}$$

[1] As already partially mentioned and as described below, these measurements and the resulting simulations do not take into account the dependencies of the spectrum on the azimuth angle.

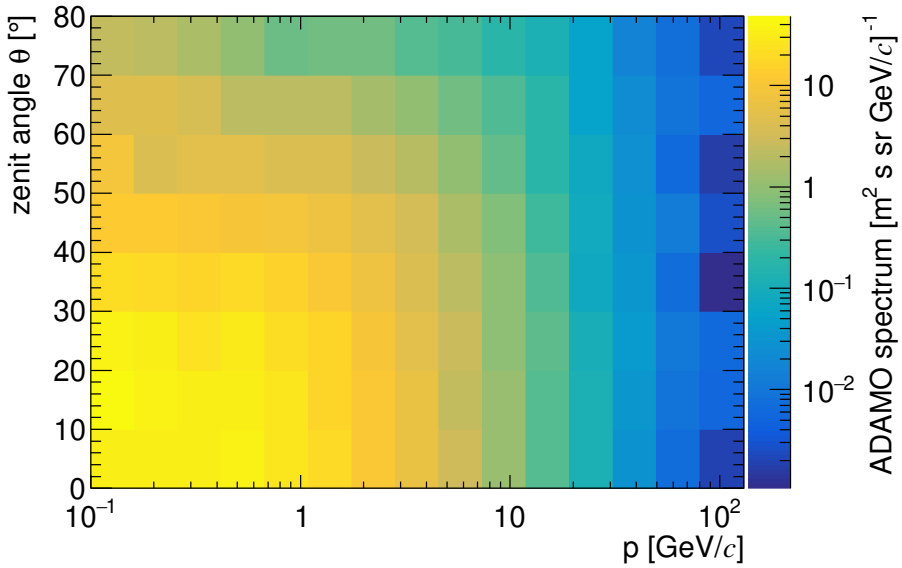

Figure 3.1: Differential flux of muons as measured by the ADAMO magnetic spectrometer. The data are divided into 8 bins in the zenith angle from 0° to 80° and in 15 bins in the muons momentum from 0.1 GeV/c to 130 GeV/c.

For the dependence of the differential muon flux as a function of the zenith angle for a given momentum p, inspiration was drawn from the formula[2] on page 372 of [7], obtaining

$$\phi(\theta; p) = \phi(\theta; \boldsymbol{b}(p)) = b_0(\cos\theta)^{b_1}. \tag{3.4}$$

In the previous equations the parameters a_i depend on the zenith angle while the parameters b_i depend on the momentum.

Figure 3.2 shows the result of the data fits as a function of the momentum for all angular bins with function 3.3. These fits were made by excluding the first four bins in momentum ($p < 0.667\,\mathrm{GeV}/c$), given that the low-momentum spectra follow a different trend due to the presence of an electron component that has not been discriminated by the magnetic spectrometer. This is consistent with the values of the electron spectrum found in the literature, reported in section 1.3.

To determine the differential muon flux for a generic pair $(\tilde{p}, \tilde{\theta})$, one proceeds as follows: for all 15 bins in momentum, a fit is performed according to function 3.4 and the 15 values of the differential flux are extrapolated for the angle $\tilde{\theta}$. Then these values are fitted with equation 3.3 obtaining the fit

[2] It should be noted that the cited formula expresses the dependence of the integral flux as a function of the zenith angle.

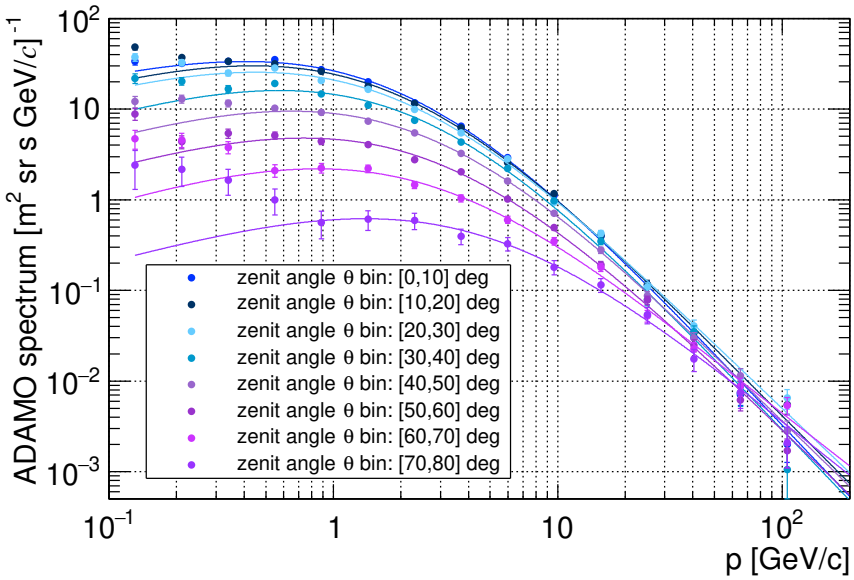

Figure 3.2: The differential flux data are divided into the various angular bins and are fitted as a function of the muon momentum using function 3.3. Low momentum measurements are excluded from the fit as they have a different trend that can be attributed to an electron component.

function $\phi(p;\tilde{\theta})$, which is therefore similar to those shown in figure 3.2. From this last function we can extrapolate the value of the differential flux sought $\phi(\tilde{p};\tilde{\theta})$ and we can obtain the integrated flux with minimum momentum $\tilde{p}_{\min}$ in the $\tilde{\theta}$ direction as:

$$\Phi(\tilde{p}_{\min},\tilde{\theta}) = \int_{\tilde{p}_{\min}}^{\infty} \phi(p;\tilde{\theta})\, dp. \tag{3.5}$$

The measurements of the differential flux made with the ADAMO detector have been carried out for a single azimuth direction, and therefore both these and the resulting simulations do not take into account the East-West effect. This effect can be partly neglected after having taken care to symmetrize the free-sky measurements, as described in section 2.2.7.

3.2.2 Geant4 simulation

Geant4 (GEometry ANd Tracking) [57] is a simulation toolkit for the passage of particles into matter using Monte Carlo methods, developed by an international collaboration that includes CERN. It is a tool widely used in various fields of physics (high energy, nuclear, medical applications and as-

trophysics) and in the case of muon radiography it is useful for comparing measurements with complete simulations. This software allows you to:

- define the target under investigation with a geometric structure and precise physical characteristics;
- define a detector (in this case the MIMA tracker) in sufficient detail;
- generate muons from a certain surface according to known particle spectrum;
- simulate the propagation of particles through the target material;
- record the points of interaction with the detector.

To obtain sufficient statistics, simulations of this type can take a long time. To reduce the computational time necessary to carry out these simulations, some tricks are used. From the generation surface, muons are generated in all directions according to the measured differential flux, but only the muons that initially point in the "vicinity" of the detector are propagated. The precise selection of the muons that are propagated is determined by the study of the particle deviation from its initial trajectory due to the multiple Coulomb scattering. In the event that the detector is completely inserted in the target to be studied (as for the measurements inside a mine), muons with too low a momentum will not be able to reach the detector, and can be excluded from the propagation process.

For some particular applications the use of the PUMAS library (Semi Analytical MUons -or taus- Propagation, backwards) is particularly advantageous. This is a C99 library for the transport of μ or τ in backward Monte-Carlo [58]. This tool has proved to be particularly useful in the case of muon radiography of volcanoes, with extremely high opacity (and therefore with extremely reduced transmitted muon flux). In this case, the background signal due to low energy muons deflected from the mountain flank (because of multiple scattering) can become relevant. For this kind of simulations, a reduction of the computation times by a factor of 10^3 was achieved using the PUMAS software, compared to traditional forward Monte Carlo simulations.

3.2.3 Range-based simulations

As we have already seen in section 1.4.1 on page 19 muons lose energy crossing materials according to formula 1.3. For this reason muons with a greater energy (or momentum) will be able to cross a target with grater opacity. This relationship is highlighted by the data shown in figure 3.3: this graph

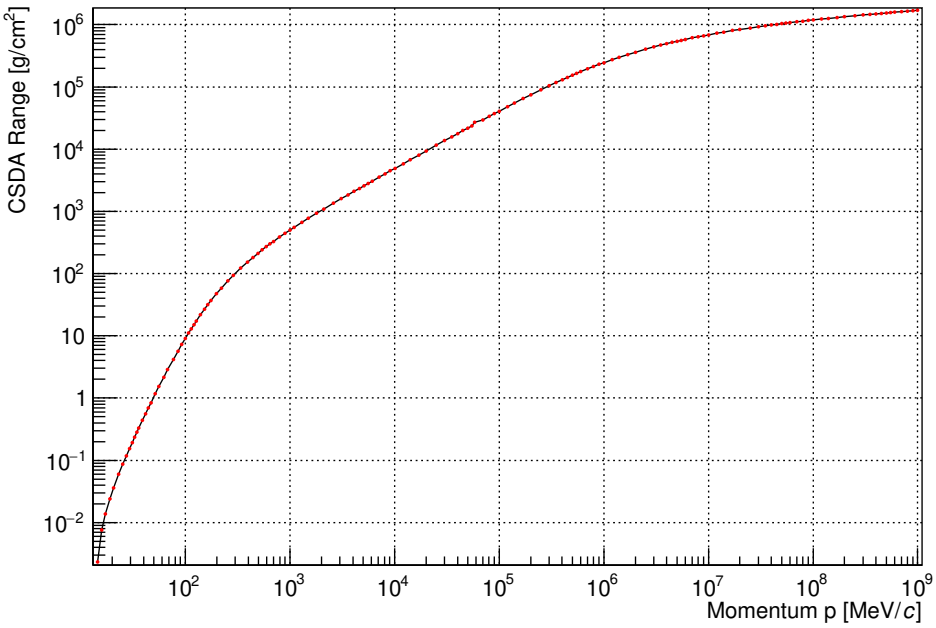

Figure 3.3: Average CSDA range for a muon in standard rock as a function of particle momentum [10].

shows the average range of muons in standard rock as a function of the momentum, according to the CSDA approximation (see equation 1.5) [10].

Although the values shown in figure 3.3 for the muon range are only average values, it can be observed that there is a bijective correspondence between the muon's momentum and the opacity it is able to pass through (in formula $X = X(p_{\min})$ and $p_{\min} = p_{\min}(X)$): as the opacity of a target increases, the minimum momentum that muons must have to pass through the material increases and the muon transmitted flux, i.e. the flux integrated with a momentum greater than $p_{\min}(X)$, decreases (see formula 3.5).

Given the above, the integral flux of muons transmitted through an opacity X at a polar angle θ can be expressed by the relation

$$\Phi(X, \theta) = \int_{p_{\min}(X)}^{\infty} \phi(p'; \theta)\, dp' \,, \tag{3.6}$$

where $p_{\min}(X)$ expresses the relationship between momentum and opacity shown in figure 3.3.

The previous equation is the one actually used in the analysis presented in this work. However, a better approximation would be obtained by using the muon survival probability P_s (presented in section 1.4.1 on page 19) as

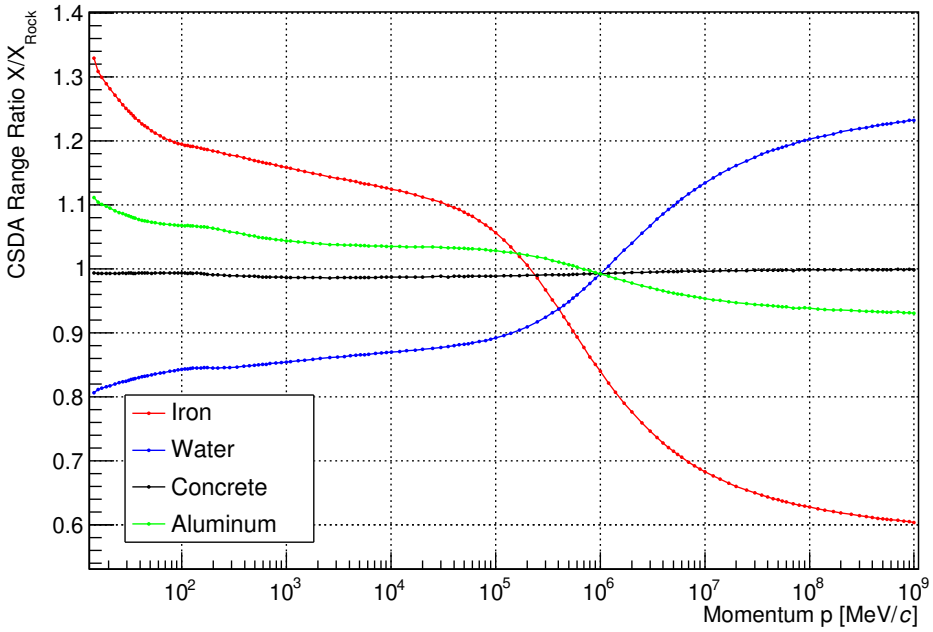

Figure 3.4: Muon CSDA range for various materials divided by the standard rock range as a function of the muon momentum. The data were taken from [10].

follows

$$\Phi(X,\theta) = \int_{p_0}^{\infty} P_s(p',X)\,\phi(p';\theta)\,dp'\,.$$

In the formula, $P_s(p',X)$ is the probability that a muon with initial momentum p' will be able to pass through an opacity X and p_0 is a sufficiently small momentum such that $P_s(p_0,X)=0$. The integrand of the previous equation (the product of the muon differential spectrum by the survival probability) is reported in [7] at figure 4.5 for three opacity values: the effect of this correction is more evident for large opacities (and therefore for large momenta) where the radiative fluctuations become relevant.

The muon CSDA-range slightly depends on the target material and in figure 3.4 the ranges for various materials divided by the standard rock range are reported. The range in concrete differs from that in rock by less than 2% while for water (both in liquid and solid form) the difference can reach 20%.

In the case of muon radiography measurements of targets with different compositions (rock, water, etc.), the calculation of the overall opacity and of the threshold muon momentum is therefore more complicated than in the case of materials with uniform composition. Appendix A describes an analytical method for calculating the threshold moment of muons crossing targets

composed of layers of different material according to the continuous slowing down approximation. These effects can be relevant for muography measurements at alpine glaciers [27] and at an embankment dam, while they will be negligible for measurements at a mine without large metal deposits such as those presented in this work. In these cases, it is still possible to perform analytical simulations that make use of the opacity-momentum conversion tables.

In [59] simulations are presented aimed at assessing the sensitivity of muographic measurements to the hydrogeological perturbations of the rock with variation of the water content.

muRange simulation

The muRange simulation software, already used in [32, 33, 49], is briefly presented below. The principles of its operation are quickly outlined, therefore, starting from the following paragraph, a generic simulation used for this work is presented which was in any case created with the muRange software.

The advantage of muon range-based simulations is that they are analytical simulations which are therefore extremely faster and more practical than those made with software that simulate the passage of particles in matter (such as Geant4) and consequently there are no problems related to low statistics. On the other hand, these simulations do not take into account the phenomenon of multiple scattering which in certain applications can be an important phenomenon. Another disadvantage (not relevant for the application presented in this work) is that these simulations currently assume that the detector is point-like.

The various steps of the muRange simulation are described below. Initially, a model of the target is created in order to calculate the material thickness map $L(\theta, \varphi)$ seen from the center of the detector. Then multiplying the thickness map by a certain average density $\bar{\rho}_0$, an opacity map $X(\theta, \varphi; \bar{\rho}_0)$ is obtained which is converted into a minimum momentum map $p_{\min}(\theta, \varphi; \bar{\rho}_0)$ according to the momentum-opacity conversion table for the selected material (for example for standard rock we will consider the graph of figure 3.3). Finally, the integrated flux map for the target configuration $\Phi_{\mathrm{S,tar}}(\theta, \varphi; \bar{\rho}_0)$ is calculated from the minimum momentum angular map thanks to equation 3.6. Similarly to what is done for the measurements, the simulation is repeated in the free-sky case: the free-sky integral flux map is obtained from an equation similar to 3.5 which is obtained by substituting the threshold momentum given by the opacity of the detector, p_{MIMA}, in place of $p_{\min}$.

Expressing this in formula we obtain:

$$\Phi_{\mathrm{S,free}}(\theta) = \int_{p_{\mathrm{MIMA}}}^{\infty} \phi(p,\theta)\, dp. \tag{3.7}$$

where p_{MIMA} is the minimum momentum required to detect muons in the free-sky configuration, estimated at about $130\,\mathrm{MeV}/c$, because of the opacity of the detector itself (see X_{MIMA} at chapter 2.1.1) i.e. $p_{\mathrm{MIMA}} = p_{\mathrm{min}}(X_{\mathrm{MIMA}})$. To be more precise, X_{MIMA} is the overall opacity of the six tracking planes in the direction perpendicular to the planes and will correspond to an average value of the detector opacity for the various possible directions. The opacity will slightly increase considering a muon crossing the six planes in an inclined direction and will decrease for those particles crossing only four of the six tracking planes (these tracks are revealed according to the chosen trigger configuration). In this second case, for example, the minimum momentum will be slightly smaller ($p_{\mathrm{min}} \approx 115\,\mathrm{MeV}/c$). Anyway the consequent relative variation on the vertical integrated flux ($\Phi_{\mathrm{S,free}}(\theta = 0°)$) will be negligible, been smaller of 1%.

Now it is possible to specify that, also for the target simulation, the detector opacity is actually added to the total opacity map of the target: in the lower bound of the integral 3.6, we will have that $X = X_{\mathrm{MIMA}} + X_{\mathrm{tar}}(\theta,\varphi)$.

Similarly to what was done in equation 3.1, the simulated transparency can now be defined as:

$$T_{\mathrm{S}}(\theta,\varphi;\bar{\rho}_0) = \frac{\Phi_{\mathrm{S,tar}}(\theta,\varphi;\bar{\rho}_0)}{\Phi_{\mathrm{S,free}}(\theta)}\,. \tag{3.8}$$

To create the average density map, simulated transparency maps are calculated for various values of $\bar{\rho}_0$. Then, for each direction (for each pixel of the angular maps), the average density value $\bar{\rho}$ is sought for which the simulated transparency is equal to the measured one, i.e. $T_{\mathrm{S}}(\bar{\rho}) = T_{\mathrm{M}}$. By interpolating the densities of the two simulated transparency maps that are closest to the measured transparency value, the average density value $\bar{\rho}$ for the selected direction is obtained.

Once the average density map $\bar{\rho}(\theta,\varphi)$ has been obtained, it can be multiplied by the material thickness map $L(\theta,\varphi)$ to finally obtain the measured opacity map $X(\theta,\varphi)$, which is needed as an input for tomographic inversion algorithms.

As we have seen, for the muRange simulation it is necessary to introduce from the beginning a model of the shape of the target to be studied. However, as we will see from the next paragraph, muon radiography allows to directly determine the opacity of the system under observation without

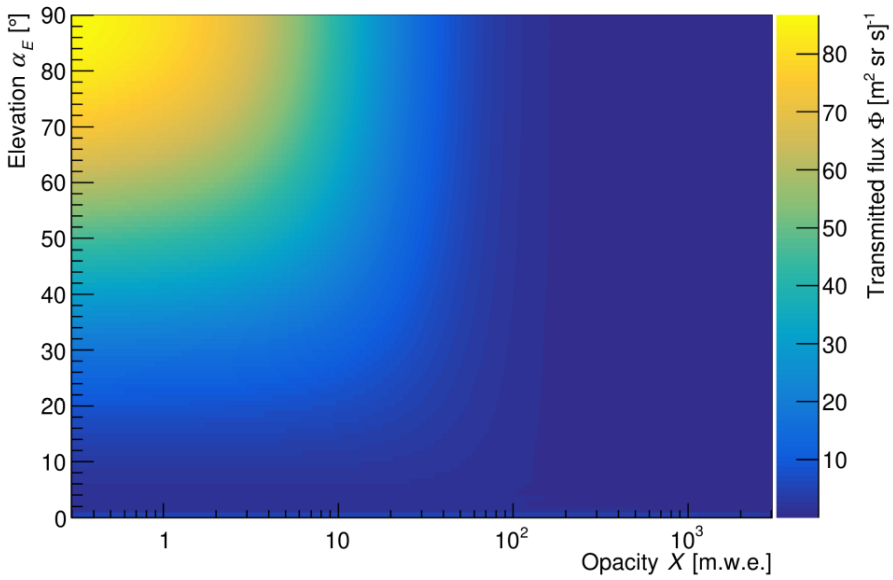

Figure 3.5: Transmitted muon flux through standard rock as a function of the crossed opacity (from 0.3 m.w.e. to 3000 m.w.e.) and of the elevation angle (from 0° to 90°). The opacity unit, m.w.e., stands for meter water equivalent, and the following equivalence holds: 1 m.w.e. = $10^2\,\mathrm{g\,cm^{-2}}$.

further information, while the model of the target shape can be introduced later on the basis of the geometric characteristics of the 3d inversion problem. In addition to this, all the relevant information of a simulation can be condensed into a single two-dimensional histogram that can be used to create multiple simulation.

Simulation with conversion map

As shown in equation 3.6, the muon transmitted flux in target configuration, to a good approximation, depends only on the traversed opacity, X, and on the polar angle, θ, or on the elevation angle, $\alpha_E = 90° - \theta$. This relationship is represented in the histogram of figure 3.5 for muons in standard rock. This histogram summarizes most of the relevant information needed in muon transmission radiography. However, as we saw in section 3.1, it is more convenient to use transmission instead of transmitted flux. Once the simulated integral flux in the free-sky configuration is known, the simulated transmission can be obtained from the ratio of the simulated flux in the two configurations (target over free-sky) as indicated in equation 3.8. In figure 3.6 the simulated transmission is represented as a function of the elevation angle and the crossed opacity in standard rock.

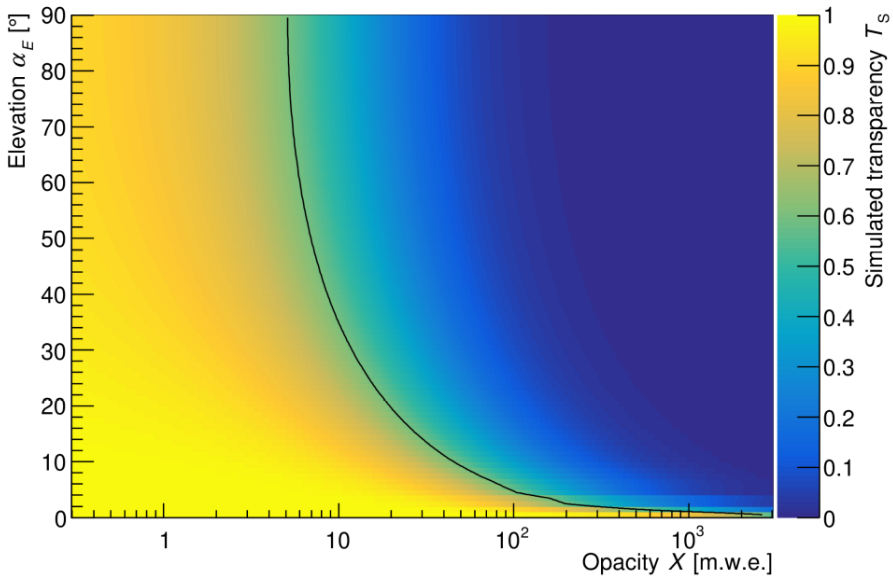

Figure 3.6: Simulated transmission as a function of the crossed opacity (from 0.3 m.w.e. to 3000 m.w.e.) and of the elevation angle (from 0° to 90°). The conversion to the International System of Units for the opacity axes is 1 m.w.e. = 100 g cm^{-2}. As a reference the contour line $T_S = 0.6$ has been drawn.

Using the two previous conversion maps, an opacity measurement can be converted into a measure of transmitted flux or into a transparency measurement. For example, for any pair of elevation and opacity values (α_E, X), the corresponding value of transmission can be obtained by a bilinear interpolation of the four pixels adjacent to the point (α_E, X) of the map in figure 3.6.

Furthermore, the conversion map also allows the measured transparency to be directly converted into an opacity measurement (with the respective measurement errors). Let's suppose a transmission T_{M0} has been measured at a given elevation α_{E0}. As a first approximation, to obtain the corresponding opacity value X_0, it is sufficient to scroll horizontally the histogram in figure 3.6 in correspondence with the elevation value α_{E0}, stop when the T_{M0} transmission is encountered and read the corresponding opacity on the abscissa axis. Usually, to make the most of this calibration simulation and improve the accuracy of the conversion, the opacity X_0 is calculated as the abscissa of the intersection point of the contour line corresponding to the transmission value $T_S = T_{\mathrm{M0}}$ with the $\alpha_E = \alpha_{E0}$ line.

In this way it is directly possible to convert a measured transparency map $T_{\mathrm{M}}(\theta, \varphi)$ into the corresponding opacity map $X(\theta, \varphi)$. Eventually the opacity

map can be divided by target depth map to get the more familiar average density map.

Estimation of measurement uncertainty

Having defined the crossed opacity as a function of the measured transparency and the elevation angle, in formula $X = X(T_{\mathrm{M}}, \alpha_E)$, and since T_{M} and α_E are independent, the measurement uncertainty on the opacity is computed as [60]

$$\sigma_X = \sqrt{\left(\frac{\partial X}{\partial T_{\mathrm{S}}}\sigma_{T_{\mathrm{M}}}\right)^2 + \left(\frac{\partial X}{\partial \alpha_E}\sigma_{\alpha_E}\right)^2}, \tag{3.9}$$

where the elevation error σ_{α_E} is equal to the variance of the elevation for each angular pixel, but, in a precautionary manner, we consider the linear dimension of the pixel ($\sigma_{\alpha_E} = 2°$), and the transparency error is given by

$$\sigma_{T_{\mathrm{M}}} = T_{\mathrm{M}}\sqrt{\frac{1}{N_{\mathrm{free}}} + \frac{1}{N_{\mathrm{tar}}}}. \tag{3.10}$$

The previous equation is derived from the propagation of the statistical error of the formula 3.2, since the number of detected muons per pixel N_{free} and N_{tar} follow the Poisson distribution. The contribution to the uncertainty due to the acquisition time is negligible.

Formula 3.9 gives a good estimate of the measurement errors and is the one actually used in this analysis, but a complete discussion would involve taking into consideration further contributions listed below (some of these are described in more detail later):

1. errors on the elevation;
   (a) angular resolution of the tracker (for each view $\sigma_{\alpha,x} \approx \sigma_{\alpha,y} \approx 0.4°$);
   (b) systematic error in the pointing direction ($\sigma_{\theta_{\mathrm{aim}}} \approx 0.3°$);
   (c) misalignments between the active part of the detector and the mechanics used for leveling ($\sigma_{\theta_{\mathrm{misal}}} \approx \frac{1\,\mathrm{mm}}{37\,\mathrm{cm}}\sqrt{2} \approx 0.2°$);
2. errors on measured transparency;
   (a) systematic errors due to the temporal variation of the muon flux (in the free-sky it is mainly due to the variation of atmospheric pressure);
   (b) residual systematic errors due to East-West asymmetry (mainly in free-sky measurement);

(c) systematic error in the azimuth pointing direction for the target measurement φ_{aim};

(d) systematic error in the zenith pointing direction for the free-sky measurement with respect to the target one θ_{aim};

(e) background from low-energy electrons (see the following section), that could also be attributed to an error on the simulated transparency;

3. errors on the calculation of the simulated transparency;

   (a) propagation of ADAMO's measurement uncertainties;

   (b) integration limits of $\phi(p)$

      - p_{MIMA} depends on the number of crossed planes (1% variation between 4 and 6 planes);
      - $p_{\text{max}} = 10\,\text{TeV}\,c^{-1} \neq \infty$ (negligible contribution given the material thicknesses involved);
      - use of a minimum momentum, p_{min}, instead of the survival probability $P_s(p, X)$;

   (c) systematic error due to multiple scattering;

   (d) double fit procedure (in θ and then in p) to evaluate the differential flux.

A complete and detailed evaluation of all contributions to error presented is beyond the scope of this work. In the previous chapters we have already tried to estimate the effect that some of the terms presented could have on the total error (East-West effect, pressure variation, variation of the minimum momentum for the free-sky measurement p_{MIMA}, etc.), while some of the other terms will now be specified and estimated..

All the terms presented in point 1, relating to the error on the elevation measurement, are smaller or much smaller than the error considered for the elevation measurement (remember that they should be added in quadrature). Moreover, as already said, σ_{α_E} has been cautiously evaluated as equal to the angular dimension of the pixels used, while the standard deviation of the elevation for each pixel would be lower.

The term 2c refers to a possible misalignment of the azimuth direction of the target measurement estimated as $\sigma_{\varphi_{\text{aim}}} \approx 1^\circ$ while, for the free-sky measurement, after the symmetrization process, it is assumed that there is no dependence on the azimuth angle. This bias will contribute to the transparency uncertainty with a term $\frac{\partial T_{\text{M}}}{\partial \varphi} \cdot \sigma_{\varphi_{\text{aim}}}$ to be added to $\sigma_{T_{\text{M}}}$ in

quadrature. Consequently, for those directions where transparency does not change much as a function of φ (on scales of the order of $\sigma_{\varphi_{\rm aim}} \approx 1°$), this term will be negligible.

Finally, an estimate is provided for the term 2d relating to a possible misalignment (estimated as $\sigma_{\theta_{\rm aim}} \approx 0.3°$) between the polar pointing direction of the free sky measurement with respect to that of the target. The polar misalignment of the target measurement is taken into account by the term 1b. We therefore suppose that the target measurement is pointed vertically ($\theta_{\rm aim,tar} = 0°$) while the free-sky one is slightly pointed North ($\theta_{\rm aim,free} = \sigma_{\theta_{\rm aim}}$). We can parameterize the free-sky integral flux as $\Phi_{\rm free} = A \cos^2\theta$. By deriving the previous equation, and taking into account that $d\Phi_{\rm free}/\Phi_{\rm free} = dN_{\rm free}/N_{\rm free}$, we obtain an additional term to the error on $N_{\rm free}$ equal to $\sigma_{N_{\rm aim}} = 2\, N_{\rm free}\, \tan\theta\, \sigma_{\theta_{\rm aim}}$. This expression is valid only for pixels that are along the North-South direction. In fact, in the perpendicular direction the hypothesized misalignment will leave the elevation measurement unchanged, leading to a zero contribution to the error. Furthermore, given that $\sigma_{N_{\rm aim}}(\theta = 0°) = 0$ (because of the $\tan\theta$ factor), we will evaluate this systematic error for $\theta = 45°$. Taking as reference the map of the muon counts of figure 2.9b, where $N_{\rm free}(\theta = 45°) \approx 7 \cdot 10^3$, we have that $\sigma_{N_{\rm aim}} = 73$ which is slightly smaller than the Poissonian statistical error on the counts for the same region $\sigma_{N_{\rm free}} = \sqrt{N_{\rm free}} = 84$. As we will see later, however, generally $N_{\rm free}$ will be much greater than $N_{\rm tar}$ (see figures 2.9b and 5.5 for comparison), since the muon rate in this second case is generally significantly lower. Consequently, the contribution to the error given by $N_{\rm tar}$ will be the predominant one in equation 3.10, thus making the correction just discussed of little relevance.

3.2.4 Soft electron background

Until now we have assumed that the tracks measured by the MIMA detector were almost exclusively due to the passage of muons. In reality, as we have seen previously both in section 1.3 on page 15 and in the graph of the ADAMO spectrum (see figure 3.2 on page 56), at low energy there is a non-negligible component of electrons. In particular from figure 3.2 it can be observed that this component becomes more relevant as the zenith angle increases. In the field of muon radiography, the background due to low energy electrons is well documented (see for example [9]).

We have seen that for a muon the opacity of the detector, $X_{\rm MIMA}$, implies a momentum threshold $p_{{\rm MIMA},\mu} = 130\,{\rm MeV}/c$. However, for electrons the same opacity corresponds to the momentum threshold $p_{{\rm MIMA},e} \approx 40\,{\rm MeV}/c$. To obtain the indicated value, reference was made to the work [61]: in bib-

liography there is a link to the ESTAR databases which reports the tables of the stopping-power and the CSDA range for electrons with various energies. The momentum value reported above is obtained both for electrons in aluminum and for electrons in polystyrene (the main materials of which the detector is made).

If on the one hand the simulations are able to exclude the muon component, limiting the fit to the most energetic part of the spectrum (see figure 3.2), the same thing cannot be done by the MIMA detector which will also measure the flux of electrons, which moreover have a threshold momentum lower than that of muons.

We now give an estimate of the contribution of electrons for the integral flux measured by MIMA in the free sky configuration. Let us consider the worst case of a measurement with $\theta = 75°$. Consequently we will refer to the data with θ from 70° to 80° of figure 3.2.

For simplicity we choose to parameterize the electron spectrum as $\phi_e(p) = p^{-\gamma_e}$. Therefore the data indicated above have been fitted with a function equal to the sum of the spectrum of electrons plus that of muons (reported in equation 3.3 on page 54). In this way it was obtained that the integral flux of electrons with momentum from $0.4\,\mathrm{GeV}/c$ to $1\,\mathrm{GeV}/c$ is about $1.3\,\mathrm{m}^{-2}\,\mathrm{s}^{-1}\,\mathrm{sr}^{-1}$ while that of muons with momentum greater than $130\,\mathrm{MeV}/c$ is equal to about $6\,\mathrm{m}^{-2}\,\mathrm{s}^{-1}\,\mathrm{sr}^{-1}$. In conclusion, in the direction close to the horizontal, a systematic error is made in the calculation of the free sky flux, and also in the measured transparency, of about 20%. This effect decreases by reducing the zenith angle and is neglected in the remaining analysis in which the detector is aimed vertically.

It must be said that this evaluation is based only on the calculation of the flux integrated from the threshold momentum for the two kind of particles. In the future it will be necessary to evaluate more accurately the relevance of this background, also considering the selection that is made in the process of track reconstruction.

A solution to solve this bias could be to simulate the contribution of electrons as well. Another simpler solution could be to increase the momentum threshold needed to detect particles. This could be done by adding a further plane consisting of a Cerenkov threshold detector, as studied in [33], or by using an additional plane with a lead layer to allow the exclusion of soft electrons, as already discussed in section 1.3 on page 15. This second option had already been adopted for the free-sky measurements with the MuRay detector for the muography of the Bourbon Gallery [48] and is currently used for the MURAVES detector [24].

Chapter 4

Muon transmission tomography

While muon scattering tomography is naturally a three-dimensional imaging technique, muon transmission radiography provides bidimensional maps of density integrated on the radial direction from the point of view of the detector. Nonetheless, similar to what is done in computed tomography (CT) in medical physics, combining multiple muon radiography measurements from different positions, it is possible to obtain the tree-dimensional distribution of density of the target. The aim of this thesis is the development of tomographic inversion techniques and algorithms to be applied to muon transmission radiography.

Algorithms of this type are already widely used in medical CT. However, in the field of muon radiography, there are a series of problems, absent in the field of medical physics, due to logistical, temporal and resolution limits intrinsically linked to the muography technique. Below are listed some complications that can be encountered in the realization of a tomography through muon radiography measurements carried out inside a mine (such as those presented in section 5.2):

1. The number of measurements is severely limited (a few units) given the time required to perform a single muon radiography.

2. In a muon radiography measurement the observation directions are all converging towards the detector which can generally be considered as point-like with respect to the target. Consequently, some portions of the volume under investigation are observed from a single measurement, and can significantly affect each measure independently.

3. All measurements are carried out from a lower altitude than the target and generally must not be too distant (and therefore too inclined) to

avoid increasing the acquisition times and introducing further regions of unknown volume.

4. The position of the detector installation points is limited by the logistics of the accessible spaces below the target (in the case of mine measurements, it depends on the geometry of the installation tunnels).

5. The resolution of the opacity measurements progressively deteriorates for directions approaching the acceptance limit of the detector.

Some tomographic reconstructions using muon radiography have already been carried out and each has its own peculiarity which depends on the system under observation [28–31, 33, 48, 62–66]: unlike the work presented here, some of these reconstructions involve a combination of muographic and gravimetrical measurements [31, 64, 65]. Furthermore many of them use regularization terms based on a priori information to reduce the non-uniqueness typical of these problems [28, 29, 31, 63, 64].

In this tomography work the methods of the aforementioned publications were used and compared. The software used in those works is the property of the collaborations that developed it and therefore also for the research group in Florence it was necessary to develop and implement these algorithms. The aim of this work is therefore to develop such tomographic inversion algorithms with particular attention to the detection and reconstruction of cavities and voids.

The works previously cited generally focus on the reconstruction of density distribution without excessive discontinuities and only a few have been developed for the identification of cavities and voids (therefore associated with large discontinuities in the density value): among these there is [30], with a very peculiar geometry of the inversion problem, [48], in which the shape and size of an unknown cavity was reconstructed even without fully using the quantitative information of the muography measurements, and [33], where a precise reconstruction of some cavities was obtained through a back-projection technique using a single muographic measurement.

4.1 Inversion problem

In all these reconstructions the inspected volume, from now on World, is modeled as a 3D grid of Voxels, $J_1 \times J_2 \times J_3 = J$ in number, usually cuboids in shape (except in [30]) with unknown uniform density. Then the muographic information is organized in a series of Solid Angle Rays, or simply Rays, each characterized by an opacity measurement, $X_i \pm \sigma_{Xi}$, and by geometrical

limits: in case the tracker can be considered point-like, as in our case, each Ray will correspond to a precise solid angle. Supposing to have I Rays and J Voxels, after this discretization process, from the opacity definition ($X = \int \rho \, dL = \bar{\rho} \, L$) the following system of equations is obtained:

$$X_i = \sum_{j=1}^{J} L_{ij} \rho_j = \boldsymbol{L}_i \cdot \boldsymbol{\rho} \,, \qquad i = 1, 2, \ldots, I, \tag{4.1}$$

where X_i is the opacity of the ith Ray, ρ_j is the density of the jth Voxel, L_{ij} is the average intersection length between the ith Ray and the jth Voxel, $\boldsymbol{\rho}$ is the vector of the densities of all Voxels and $\boldsymbol{L}_i$ is the vector of the intersection lengths of all the Voxels with the ith Ray. For a given Ray, just a few Voxels will be intersected and will contribute with their density to the Ray's opacity and therefore L_{ij} is an element of a sparse matrix ($\mathbf{L}$). The goal will be to determine the density values that solve the system of equations 4.1.

4.1.1 Non uniqueness and regularization methods

Tomographic inversion, like other inversion problems, is a ill-posed problem: the same muon radiography measurements can be obtained from multiple density distributions, even very different from each other. Figure 4.1 shows an example of a pathological case: consider a certain number of muon radiography measurements carried out from a tunnel below a hill, so that the acceptance of each measurement intersects two horizontal layers of equal thickness and placed below the surface of the hill. Once a solution to the tomographic inversion problem has been found, it will be sufficient to vary the density of the two layers in the opposite way, to obtain other infinite solutions of the inversion problem. This indeterminacy, generally not present in medical CT, is due to the fact that it is not possible to carry out a muon radiography measurement in a completely horizontal direction.

Given the above, various regularization methods will have to be applied to make the problem solvable such as those indicated below:

- require that the density distribution does not deviate too much from a certain initial model;
- require continuity in the density of neighboring Voxels;
- consider a limited set of possible density values;
- take advantage of any symmetries of the target;
- choose a particular geometry for the shape of the Voxels;

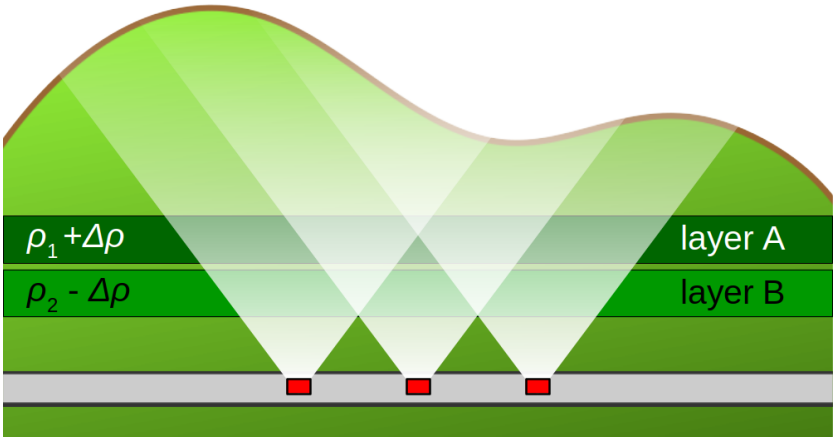

Figure 4.1: Example that illustrates why tomographic inversion is an ill-posed problem. The detectors (in red) are installed at the same height inside a tunnel and the muographic measurements entirely intersect two internal layers of the hill (A and B) of equal thickness. Given a solution for the tomographic reconstruction problem, there will be infinite other solutions which are obtained by varying the density of the two layers in the opposite way.

- combine muography with other geophysical methods (e.g. gravimetry).

4.2 Inversion algorithms

The algorithms implemented and employed in this work are presented below. Some of these have been chosen as they are usually used in the field of muon tomography while others are being used here for the first time.

4.2.1 Minimum of Chi-squared

In the case of real measures affected by errors, a solution to the system of equations 4.1 will not necessarily exist (if instead the system is indeterminate, there will be an infinite number of solutions). In this case, taking into account the opacity uncertainty, σ_{Xi}, it will be necessary to find the density vector that minimizes the Chi-squared on the opacity, χ^2_X, shown below:

$$\chi^2_X = \sum_{i=1}^{I} \left(\frac{X_i - \boldsymbol{L}_i \cdot \boldsymbol{\rho}}{\sigma_{Xi}} \right)^2 . \tag{4.2}$$

As already discussed in the previous paragraphs, the minimization of the opacity Chi-square is not enough to solve the inversion problem because there may be pathological configurations, such as the one represented in figure 4.1, which make the problem not solvable in a univocal way. Following the work presented in [28, 29, 31, 64], the optimal solution is obtained by minimizing the following global objective function χ^2_{TOT},

$$\chi^2_{\mathrm{TOT}} = \chi^2_X + \sum_i \alpha_i \chi^2_i, \tag{4.3}$$

which is the sum of the opacity misfit function, χ^2_X , and other regularization functions, χ^2_i, that ensures smoothness. In the previous equation α_i is a trade-off parameter that find the balance between model complexity and how well the recovered model reproduces the observed data. Usually the first regularization term introduced correspond to the following volume term, that emphasize the solution closeness to the reference model:

$$\chi^2_V = \sum_{j=1}^{J} \left(\frac{\rho_j - \rho_j^{\mathrm{mod}}}{\sigma_j^{\mathrm{mod}}} \right)^2, \tag{4.4}$$

where ρ_j^{mod} is the density of the jth Voxel according to the reference model and σ_j^{mod} is the density accuracy given by the model. Another regularization term, used in the works cited above, is the following surface term:

$$\chi^2_S = \sum_{j=1}^{J} \sum_{w=x,y,z} \alpha_w \left(\frac{\partial \rho_j}{\partial w} \right)^2 \tag{4.5}$$

where α_w is a constant that penalizes roughness in each of the main directions, $w = x, y, z$. Unlike what is reported in some of the aforementioned articles, in this case there is no reason to hypothesize a different smoothness for the three directions and therefore the term α_w will be constant and can be reabsorbed in the variable α_S. In the case of cubic Voxels, equation 4.5 simplifies as follows

$$\chi^2_S = \sum_{j,j' \text{ adjacent}} (\rho_j - \rho_{j'})^2, \tag{4.6}$$

since the derivative of the density is proportional to the difference between the densities of the adjacent Voxels $(\rho_j - \rho_{j'})$ and the scale factor, constant for each direction and equal to the distance between the two Voxels, has been incorporated again in α_S. Two Voxels are considered adjacent if they have a common face.

Now consider the example of a tomography of a hill with uniform density, with unknown voids inside it: the initial model will correspond to the hill without cavities. The explanation of the names of functions χ_V^2 and χ_S^2 can now be understood: in this case these terms will be respectively proportional to the volume and the surface of the unknown cavities.

The regularization terms presented above can be useful for reconstructing a rather uniform density distribution and in case a target density model is actually present. However, in the case in which a tomography of voids inserted in a homogeneous medium (with density ρ_0) is to be performed, as for the measurements in the mine presented below, both terms can be counterproductive: the surface term limits the abrupt transitions of density that occur at the edges of the cavity and the volume term, for each Voxel, will favor a single density value (which cannot be zero and ρ_0 at the same time). In section 5.3.2 on page 105, a variant of the volume regularization term will be presented, which will solve this problem.

4.2.2 The ART family algorithms

Given the usually high values for I and J (see section 5.3.1 for example) the minimization of the Chi-squared defined in equation 4.3 is computationally expensive. To reduce the computational time and still achieve a good result, iterative methods can be used. ART (Algebraic Reconstruction Technique) is an iterative algorithm commonly used in medical physics (see [67] for instance) that allows to solve systems of linear equations even with a large number of unknowns and equations [68]. The vector of unknown densities of dimension J can be represented as a point in a J-dimensional space, while the system of I equations reported in 4.1 can be thought as I hyperplanes in the same space, since each equation is expressed as a linear combination of the Voxels densities. In an ideal problem, without any uncertainties, the solution will correspond to the intersection of the hyperplanes, while in a real case the hyperplanes will not intersect in a single point. In the ideal case the ART algorithm allows to converge to the solution by sequentially projecting the point-solution on each hyperplane-equation at each iteration. Expressing this in formula, projecting on the ith hyperplane, the vector of the density variation will be given by

$$\Delta\boldsymbol{\rho}_i^{\mathrm{ART}} = \frac{X_i - \boldsymbol{L}_i \cdot \boldsymbol{\rho}}{|\boldsymbol{L}_i|^2}\,\boldsymbol{L}_i. \tag{4.7}$$

From the formula it can be deduced that, for a given Ray, the Voxels that have a greater intersection length L_{ij} will be modified more by the ART algorithm.

Interesting convergence properties can be found in literature also in the case of real measurements affected by errors [68] and the ART algorithm has been already used to perform a tomographic reconstruction of nuclear reactor using muography synthetic data [62]. Nonetheless two aspects are not fully satisfactory: the order chosen for projecting the solution on the hyperplanes can determine the convergence speed and, secondly, there is no way to take account of opacity uncertainty of each Ray.

SART

The SART (Simultaneous ART) algorithm is a small variant of the ART algorithm [68]: each single iteration corresponds to the average of the variations that would be obtained by projecting the point on each hyperplane using the ART algorithm. In this way it is possible to disengage from the order of projection and a bigger relevance can be given to the more precise opacity measurements. To do this, a weighted average will be used with weights w_i inversely proportional to the squared opacity uncertainty. In formulas the density variation vector can be expressed as:

$$\Delta\boldsymbol{\rho}^{\mathrm{SART}} = \frac{\sum_{i=1}^{I} w_i \Delta\boldsymbol{\rho}_i^{\mathrm{ART}}}{\sum_{i=1}^{I} w_i}, \qquad w_i = \left(\frac{X_i - \boldsymbol{L}_i \cdot \boldsymbol{\rho}}{\sigma_{Xi}}\right)^2. \tag{4.8}$$

In the previous formula a global normalization was used: the denominator of the density variation is constant for all the Rays. Moreover, it corresponds to the Chi-square of the opacity defined in formula 4.2. In this way, on average the density of a Voxel is varied proportionally to the number of Rays that intersect it: considering the ith Ray and the jth Voxel, the numerator is different from zero only if $\Delta\rho_{ij}^{\mathrm{ART}} \neq 0$ i.e. only if $L_{ij} \neq 0$. Alternatively, a local normalization can be chosen: for each Voxel only the weights w_i for which the numerator is not zero are added to the denominator (i.e. only for the Rays that intersect that Voxel for which $L_{ij} \neq 0$).

This algorithm has already been used successfully to carry out the tomographic reconstruction of a target consisting of lead blocks arranged in a non-trivial geometry, with the muon absorption radiography technique [66].

DART

The DART algorithm (Discrete ART), a further variant of the ART algorithm, exploits the a priori knowledge of the composition of the target, assuming that the Voxel density is limited to a finite number of discrete values $\tilde{\boldsymbol{\rho}} = (\tilde{\rho}_1, \ldots, \tilde{\rho}_n)$. It is a heuristic algorithm without guaranteed convergence, but it represents an evolution of the algorithms of geometric tomography

(where only the shape of binary images is reconstructed, with only two density values) and of discrete tomography (where the number of Voxels and the number of gray levels are small) [69].

The technique iteratively alternates continuous reconstruction processes (SART iterations) with discretization phases. The goal of each cycle is to gradually adjust the margins of regions with uniform density and possibly introduce regions with different densities not previously present.

In the case of a mine measurement where it is assumed there are only two possible values for density (the average density of the rock and the zero density of a vacuum) this algorithm could be a useful quantitative complement to the triangulation algorithm presented below.

4.2.3 Triangulation

The triangulation is the process of determining the location of an object by forming triangles to it from known points. This is not a real tomographic algorithm but it allows to identify the shape and position of volumes with anomalous densities observed from several points of view.

This technique has already been applied in the field of muon radiography in the works [33, 48] (in [33] part of the measures presented also in this work have been used). For both studies, regions with anomalous signals, associated with the presence of a cavity, are sought in the angular maps of the muography measurements. These angular regions are then used to carry out the actual triangulation. To do this, after defining a Voxel grid (which for this work will correspond with the World presented previously), those Voxels that are observed by all the measurements in an angular region with an anomalous signal are identified. These Voxels are then interpreted as consisting of air.

In the article [48] the anomalous regions are identified as clusters with high relative transparency (the relative transparency is equal to the ratio between the measured transparency and the simulated one): for each measure the seeds (i.e. the starting angular regions) are determined by imposing a minimum threshold on the relative transparency. Then each cluster is increased by merging the adjacent pixels that exceed a second minimum threshold (lower than the previous one) in the relative transparency value. This algorithm thus makes it possible to identify well-defined signal regions for each measurement, excluding isolated regions with high relative transparency, due to noise fluctuations. However, the analysis reported in this paper is based on the study of relative transparency, a physical quantity that depends on the presence of empty volumes, but does not allow to give direct quantitative information on its dimensions.

In the work presented in [33], on the other hand, average density maps are used and therefore it is possible to evaluate the thickness of the identified cavities (even if no clustering algorithm is used). However, in both works the cuts use constant thresholds and do not depend on the thickness of the material crossed. As we will see below, however, the presence of a void of a fixed size will have a different effect, in terms of average density, based on the total thickness of the material. Moreover, in both cases, the error for the relative transparency or average density measurements is not considered.

A triangulation algorithm was therefore developed that took the best of the aforementioned works. To begin with, it is assumed that the target density is generally uniform and equal to ρ_0, and that the anomalies in the average density value are exclusively due to the presence of voids with zero density (the validity of these hypotheses will be discussed later also in the light of the results obtained). Assuming that in a certain direction (θ, φ) there is a void with a thickness $L_V > 0$, and that the target has a total thickness equal to $L(\theta, \varphi)$ (including the void thickness L_V), the average density expected by the model will be equal to

$$\bar{\rho}_V(L_V, \theta, \varphi) = \rho_0 \left(1 - \frac{L_V}{L(\theta, \varphi)}\right).$$

Let's now define the criterion for identifying the seed of the clusters in the density maps. Suppose the measurement of the average density in the same direction, $(\bar{\rho} \pm \sigma_{\bar{\rho}})$, is smaller than the value expected by the model. After omitting the angular dependencies, if

$$\bar{\rho} < \bar{\rho}_{\text{seed}} = \bar{\rho}_V(L_V) - n_{\text{seed}} \cdot \sigma_{\bar{\rho}}\,, \tag{4.9}$$

the void thickness will be greater than L_V with a confidence level of n_{seed} sigma. The previous criterion defines the seeds of the clustering algorithm. Then, as already seen above, the cluster is grown by incorporating the adjacent pixels that satisfy the condition 4.9, but with $L_V = 0$ and changing n_{seed} into n_{clu} as follows:

$$\bar{\rho} < \bar{\rho}_{\text{clu}} = \bar{\rho}_V(L_V = 0) - n_{\text{clu}} \cdot \sigma_{\bar{\rho}} = \rho_0 - n_{\text{clu}} \cdot \sigma_{\bar{\rho}}. \tag{4.10}$$

The same equations translated in terms of opacity become

$$X_V(L_V, \theta, \varphi) = \rho_0 \left(L(\theta, \varphi) - L_V\right), \tag{4.11}$$

$$X < X_{\text{seed}} = X_V(L_V) - n_{\text{seed}} \cdot \sigma_X, \tag{4.12}$$

$$X < X_{\text{clu}} = \rho_0 \cdot L(\theta, \varphi) - n_{\text{clu}} \cdot \sigma_X, \tag{4.13}$$

where the equation 4.12 identifies the Rays which are seeds of clusters and 4.13 defines the criterion for growing a cluster. The triangulation method is then applied to the identified clusters as explained above.

As highlighted in [48], the triangulation technique, since it is applied to extended cavities, identifies as voids even those Voxels that in a projection appear in the shadow of the cavity (both front and back), rather than inside. The halo could be reduced by moving away the position of the measurements so as to observe the cavity from more diversified angles, but in this case additional portions of targets observed by a single measurement would be introduced, complicating the tomographic reconstruction. The DART algorithm, presented in paragraph 4.2.2 on page 74, could be used to limit the halo of the cavity.

Chapter 5

Muography of the Temperino mine

This chapter describes some muon radiography measurements taken inside the Temperino mine at the San Silvestro Archaeological park. The park is first described, then the geometry and physical characteristics of the installation site and the measurement target are described. After that, the results obtained from the analysis of muon radiography measurements are shown which, combined together, allow to create a tomographic reconstructions of the mine. The analysis carried out focus particularly on the identification and reconstruction of the cavities present in the mine.

5.1 The Temperino mine at the San Silvestro park

5.1.1 The Archaeological park

The Archaeological Mining Park of San Silvestro, located in Campiglia Marittima (LI), takes its name from the medieval fortress located inside of it. The park was founded in 1996 with the aim of witnessing the millennial history of mining that has taken place in this area and to enhance the great archaeological heritage of the etruscan and medieval times.

The mining activities of the area have always been centered on the search for a hard and dense rock called skarn in which there are metallic sulphides of Cu, Ag, Pb, Zn, Fe (chalcopyrite, argentiferous galena, blenda and pyrite). The mineralization is embedded in the marble and is generally associated with veins of porphyry, mafic and acid, which follow the Apennine trend in a NW-SE direction [70, 71]. The typical densities of the rocks present in the

Table 5.1: Typical rocks present in the mine with their theoretical and measured densities [32, 33]. The measured densities were obtained from rock samples taken from the Temperino mine.

Rock	Density [g/cm^3]	
	Theoretical	Measured
Pure massive hedenbergite	3.6	
Pure massive ilvaite	4.0	
Skarn (hedenbergite + ilvaite)	3.3–3.5	3.08 ± 0.07
Skarn rich in Cu-Fe sulfides	3.5–3.7	
Marble	2.7	2.70 ± 0.06
Acid porhyry	2.5–3	2.41 ± 0.07
Mafic porhyry		2.62 ± 0.08

mine are reported in table 5.1.

The first mining activities date back to the etruscan period and then resume in the medieval period and, in this second case, are witnessed by the development of the mining village of San Silvestro inhabited from the 10th to the 14th century. The etruscan and medieval mining techniques are very similar: the excavations are developed in tortuous tunnels and narrow wells that follow the skarn veins. Already inside the mine a sorting was made: the most mineralized rock was brought outside, while the sterile materials (the gangue) were accumulated in the tunnels already exploited, so as to avoid useless work and in order to close dangerous voids. In this way, fillings are created whose rocky fragments, with the passing of the centuries and with the action of water, are welded to form a sort of artificial rock.

Cosimo I de' Medici relaunched the mining activity in the mines of Campiglia in the mid-16th century by calling expert German miners, called Lanzi, who started large open-pit excavations and sculpted huge underground rooms (such as the Gran Cava). However, the results were not satisfactory: the lack of water, the scarcity of minerals in the veins and the limitations of technologies, still unsuitable to separate the metals from the gangue, were some of the problems encountered that led to the closure of the mines after just five years of activity. In the 1800s and 1900s various mining companies (first French and then British) sought fortune in these territories with huge investments, but without success. With the flotation process, in the second half of the twentieth century, the extraction work became convenient, but the harsh working conditions and the competition from Latin American and Asian mines made every activity close permanently in 1983.

5.1.2 The target: the Temperino mine and the Gran Cava

The Temperino mine, one of the mines of the San Silvestro park, is an underground labyrinth of shafts, tunnels and descents. Figures 5.1a and 5.1b show the structure of the Temperino mine in vertical section and plan respectively: the Temperino mine is divided into five levels, with increasing depths, and, at the most superficial level, a 360 m long tourist route has been created, where it is possible to compare ancient mining techniques with modern ones. Modern excavations, dug horizontally, intercept the ancient tunnels, so as to use them as accesses to new mining areas. Sometimes modern excavations encounter an ancient well filled with waste materials (the filling described above) which may indicate the presence of an ancient extractive void placed higher up. Inside the mine the humidity is very high and the temperature is around 14 °C throughout the year (as also measured by the detector's environmental sensors.).

The so-called Gran Cava is an extraction void from the Medici era, then expanded in modern times, which intercepts ancient excavations. This cavity can be roughly schematized as a cylinder with a diameter of about ten meters which extends for about 40 meters in the NW-SE direction. The tunnel faces the outside through two main openings: on the North side there is the entrance to the excavation while on the opposite side there is a very large vertical opening which today appears as a collapse. Two photos of the interior of the Gallery are shown in figure 5.2.

This tunnel has always been involved in intense mining activity: at the beginning of the 20th century the miners dug a pit that reached a depth of 125 m connecting all the underground levels (see figure 5.1a). In the past, the Gran Cava was probably also connected to other secondary tunnels: today there is only one other connection with the outside through a tunnel that departs from the main void after thirty meters from the entrance on the North side and continues in a direction parallel to the Gran Cava (see figure 5.1b). At the end of this tunnel there is a wooden beam and therefore we will refer to this excavation section as the "beam tunnel".

It is in this varied context that some muon radiography measurements have been made. This work focuses on the analysis of the measurements made in the area of the Temperino mine located below the Gran Cava. The presence of this large extractive void, placed above a gallery easily accessible with the measurement instrumentation, has made this site an important scientific laboratory for the muographic research group of Florence: it allowed the team to develop analysis algorithms and validate the muography technique by studying a partially known target with optimal geometric char-

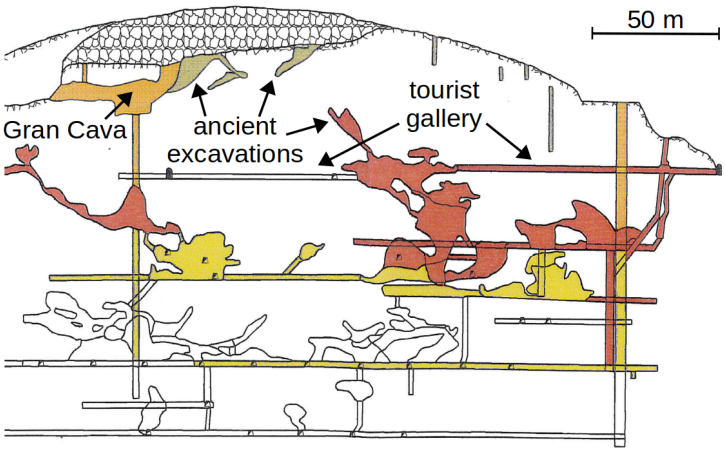

(a) Vertical section in the NW-SE direction of the Temperino mine.

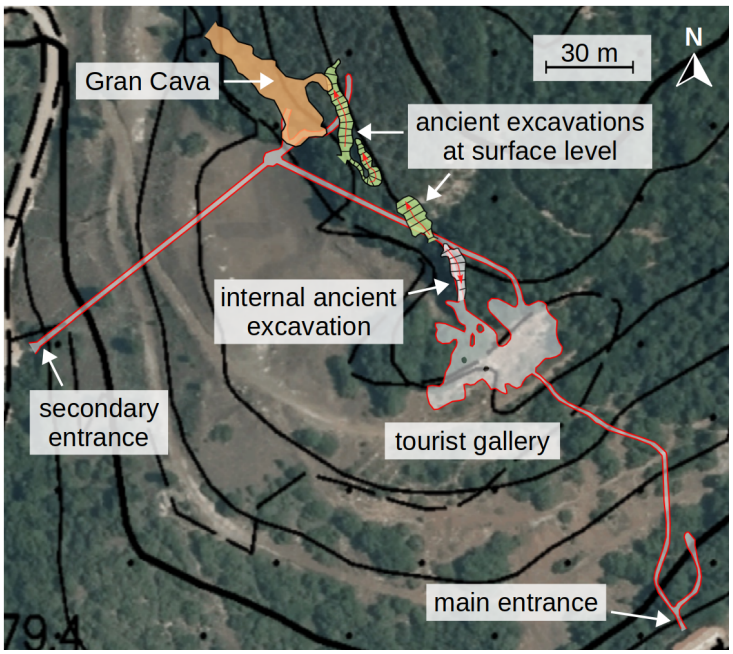

(b) Plan map of the first level of the mine and of the known excavations on the surface.

Figure 5.1: As shown in figure (a), the mine consist of multi-level tunnels and the shallowest one corresponds with the tourist route. The maps show the Gran Cava (in orange) and some ancient tunnels accessible from the surface of the hill (in green), including the beam tunnel connected to the Gran Cava. Figure (b) shows some contour lines of the hill above the mine which indicate the slope of the hill towards Southwest.

(a) Entrance to the Gran Cava towards the North West.

(b) Collapse of the Gran Cava towards the South East.

Figure 5.2: The Gran Cava seen from the inside: in figure (a) the entrance is observed while in (b) the collapse can be identified. The masonry works were carried out by the mining companies in the early 1900s. Above it is visible an ancient mining well (the black cavity) cut horizontally by the modern excavation. These photos are taken from [72].

acteristics. Furthermore, the site of archaeological interest has many ancient and unmapped tunnels that can be identified thanks to the muography technique. The presence of materials with different densities inside the mine complicates and enriches the study.

5.1.3 Geometric structure of the target

In order to correctly interpret the various muon radiography measurements taken inside the Temperino tourist gallery, it is necessary to define the geometry of the problem as precisely as possible.

Lidar of the hill and of the Temperino mine

As we have seen, muon radiography measures opacity in a certain direction and therefore, to obtain the average density of the target, it is necessary to know the thickness of material crossed by the muons before reaching the detector. This information was obtained using the airborne lidar reliefs[1]

[1]Lidar is a method for measuring distances by illuminating the target with laser light and measuring the reflection with a sensor. By measuring the delay of the reflected signal

of the hill above the mine. Data were obtained from the following source: Ministero dell'Ambiente e della tutela del Territorio e del Mare –"Rilievi Lidar". The lidar data is organized as a series of altitude values, expressed for a grid of points $(x, y) \equiv (\text{East}, \text{North})$ equally spaced in both directions in steps of one meter. If necessary, through an appropriate interpolation, it is possible to express the altitude of the hill as a continuous function of parameters x and y.

In order to calculate the thickness of the material crossed, it is not enough to know the shape of the target, but it is also necessary to georeference the telescope. In particular, for each measurement the position of the detector and its pointing direction must be known. To do this, it is first necessary to know the installation environment in terms of position, orientation and geometry. It is easy to obtain this information for outdoor measurements, thanks to the use of satellite maps available online, while it is not trivial in the case of an underground tunnel. For this reason, the collaboration with the researchers of the Department of Earth Sciences (DST) of the University of Florence was fundamental: they carried out a series of lidar measurements with extremely precise instruments (with a resolution of less than one cm). Using a backpack-wearable laser scanner, a full scan of the entire tourist gallery was carried out in one working day. This survey was then extended to the outside, both from the entrance and from the exit of the tunnel, where it was georeferenced by scanning some reflectors (usually 5 for each end in order to have some additional safety constraints) whose position was measured with a satellite GPS with resolution of a few centimeters. The constraints imposed on the positioning and orientation of the tunnel scans were found to be in agreement with an overall uncertainty of about 10 cm: this is therefore an extremely accurate measure if we consider that the tunnel is articulated in a complex way and develops along a route about 360 m long.

Position and orientation of the detector

The internal scanning of the tunnel allowed us to determine the position and orientation of the detector for each installation. In particular, it is easy to calculate the spatial position of a specific detector point by measuring its distance from at least four known reference points[2] with a laser pointer. The

compared to the emitted one, it is possible to calculate the distance to the target. In the case of airborne lidar measurements, the position of the aircraft is known through GPS measurements and it is thus possible to trace the coordinates of the scanned points.

[2]Actually, once the distance of the desired point, which we will call A, has been measured from three appropriately chosen reference points, there are only 2 points in space that satisfy the required conditions: the pair of points is obtained from the intersection

reference points, whose position is provided by the laser scanner surveys, were chosen in such a way that they were easily identifiable in the laser scanner surveys themselves, thanks to the density of the points detected and also thanks to the information on the reflectance of the laser (the edge of an electric box, the crossing of a railing, the reinforcement pegs on the vault of the gallery, etc.).

In this way, after having estimated the orientation of the detector (see below), the position of its centroid can be determined with a resolution of a few centimeters. This accuracy is more than sufficient for our purposes, given the size of the target to be inspected.

The positions of the four installations have been chosen in such a way as to have a stereoscopic view of the Gran Cava, while leaving the detector pointed vertically ($\theta_{\text{aim}} = 0°$) in order to reuse a single free-sky measurement. Furthermore, more angled measurements made from more distant points, if on the one hand they increase the stereoscopic vision, on the other they are influenced by portions of the mine not observed by the other measurements, thus introducing further unknowns. In any case, the choice of installation points was constrained by the shape of the gallery and it was avoided to hinder the tourist itinerary of visitors, instead enhancing the installations as a further step of the guided tour.

Table 5.2 shows the distances along the main axes[3] (x, y, z) of the MIMA center for the four installations in the mine with respect to the arbitrary point P: this point is defined by the coordinates $\boldsymbol{r}_P = (631\,400, 4\,770\,440, 180)$ m of the zone 37T of the UTM reference system. The measures have been sorted in ascending order by the x coordinate and each has been marked with a letter (A to D) as shown by the first column of the table. The same column also indicates the temporal order in which the measurements were carried out.

To get the pointing direction of the tracker, the angles θ_{aim} and φ_{aim} described in paragraph 2.1.1 on page 31 must be measured. The polar angle of the detector is measured with accuracy to a few tenths of a degree (more than sufficient for such measurements) using a bull's eye level, while it is more difficult to measure the aiming azimuth with the same accuracy. To measure this angle, a compass can be used, the accuracy of which can be limited to a few degrees due to the influence of any ferromagnetic materials

of the three spheres centered in the relative reference points. With this information it is sometimes possible to uniquely identify point A (the other point could be discarded because it is not accessible) and in any case another scalar information (vertical distance from the ground, or from another reference) is sufficient to constrain completely the point sought.

[3]See paragraph 2.1.1 on page 31 for the definition of the global reference system used.

Table 5.2: The table shows the coordinates of the MIMA center scaled with respect to the arbitrary point P defined in the text, the aiming azimuth angle (as defined in paragraph 2.1.1 on page 31), the acquisition time (with the dead time subtracted) and the muon rate for the four installations in the Temperino mine presented in this work. The first column also reports an ordinal number indicating the actual order in which these measurements were made. The 2nd and 4th measures are missing because these were carried out in other sites of the mine which are not of interest for this study.

Measures	$x - x_P$ [m]	$y - y_P$ [m]	$z - z_P$ [m]	φ_{aim} [°]	t_{ACQ}	r_μ [Hz]
A (3rd)	69.93	0.40	5.37	46	59 d 11 h	0.53
B (1st)	76.9	7.1	5.3	179	53 d 10 h	0.51
C (6th)	84.04	5.08	5.14	-74	55 d 20 h	0.46
D (5th)	94.21	9.28	4.98	120	67 d 6 h	0.43

placed nearby or by the detector itself, which lead to a change in the Earth's magnetic field. The measurement will then be corrected for the magnetic declination to obtain the direction of the geographic North. The aiming measurement can also be performed with known references present inside the tunnel: in this case the alignment will improve as the distance from the reference increases. Using both methods, on average, overall accuracy better than one degree is achieved. The azimuth pointing angles, φ_{aim}, for the four installations are shown in table 5.2.

The same table also shows the acquisition time (with the dead time subtracted) and the particle rate for each of the four measures. As we will see later, it is no coincidence that the rate decreases passing from measure A to D.

The scanning of the installation tunnel, in addition to what has been said previously, also serves to evaluate the thickness of the air above the detector which will be subtracted from the total length of material obtained from the lidar reliefs.

Finally, using a terrestrial laser scanner, the DST researchers scanned a portion of the hill above the installation points and the entire interior of the Gran Cava and then georeferenced the point clouds acquired. The measurements made with the terrestrial laser scanner allowed to validate the the airborne lidar reliefs of the hill since the two measurements are on average in agreement within an error of about 30 cm.

All the measurements and the reliefs made are represented in a synthetic way in figure 5.3: the scanned points of the tourist gallery are shown in

black, while the installation points are identified by the white squares and the letters from A to D. The remaining points are colored in based on their height with respect to the installation point A ($z - z_{\mathrm{A}}$). Moving from the bottom to the top, one encounters the scan of the floor of the Gran Cava and of the beam tunnel, and lastly the lidar relief of the hill, which slopes towards the South-West. We now understand why the muon rate, reported in table 5.2, decreases passing from measurement A to D: the thickness of the hill above increases causing a decrease in the number of transmitted muons.

Mesh of the known cavities and depth maps

The Gran Cava survey (and that of the beam tunnel) is useful for obtaining a reference on where to expect the cavity signal in the muography maps. To do this, we considered the volume of air contained inside the Gran Cava, approximately delimited at the level of the accesses of the cavity by the surface of the hill (defined by the lidar). To obtain this volume, we started from the Gran Cava point cloud and calculated the normals using the CloudCompare software [73]. With the same program we have generated a triangular polygon mesh[4] using the Poisson Surface Reconstruction algorithm [74].

Once the mesh of the Gran Cava was obtained, it was studied how this volume is observed by the various muography measurements in the polar reference system. The procedure that follows is partially presented in [49]. Using the C++ library CGAL (Computational Geometry Algorithms Library) the angular maps of the air thickness of the Gran Cava seen from each installation point were created. After applying the same procedure to the beam tunnel, the angular maps of the sum of the cavity thicknesses, shown in figure 5.4, were obtained. To obtain these angular maps, for each pixel (or solid angle) of the map, the straight line defined by the central direction is considered. Then the coordinates of the points of intersection of this line with the mesh are calculated. The number of intersection points will be even, given that the mesh is closed (except for the unlikely cases in which the line is tangent to a face of the mesh), and each intersection will alternatively correspond to the outside-inside and inside-outside transitions with respect to the selected volume. Adding the length of all segments within the mesh determines the thickness of air for the selected direction.

Since all the measurements presented in this work are directed vertically, the polar reference system is always used to show any angular map. The angular maps obtained in this way are similar to the plan image of figure 5.3 (it is possible to observe a similarity in the shape of the Gran Cava) and

[4] A polygon mesh is a collection of vertices, edges and faces (in this case triangles) that defines the shape of a polyhedral object.

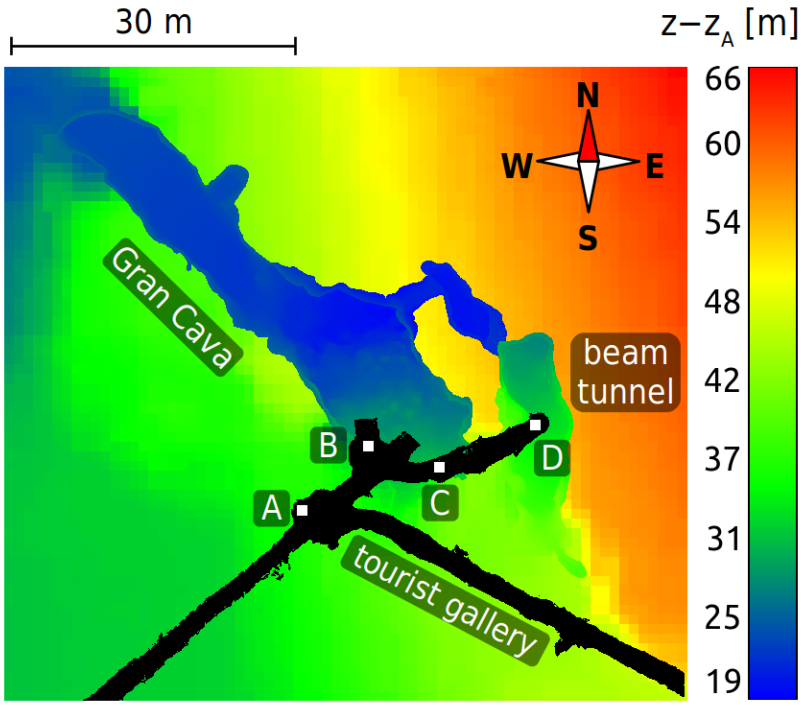

Figure 5.3: Plan view of the geometry of the tourist tunnel, the installation points, the Gran Cava and the hill. Moving from the bottom up, you will find the tourist gallery (in black), the MIMA installation points (white squares with the letters from A to D), the excavations of the Gran Cava and the beam tunnel (the laser scan of their floor), and the airborne lidar of the hill. The various layers that make up the image have been ordered to show all the elements at the same time. The color of the tunnels (except for the tourist gallery) and of the lidar indicates the altitude with respect to installation point A. After the installation point D, the the excavation of the tourist tunnel (in black) continues North for about 15 m, but this section has not been represented to make the beam tunnel more visible. This image was created with CloudCompare software (a 3D point cloud and mesh processing software) [73].

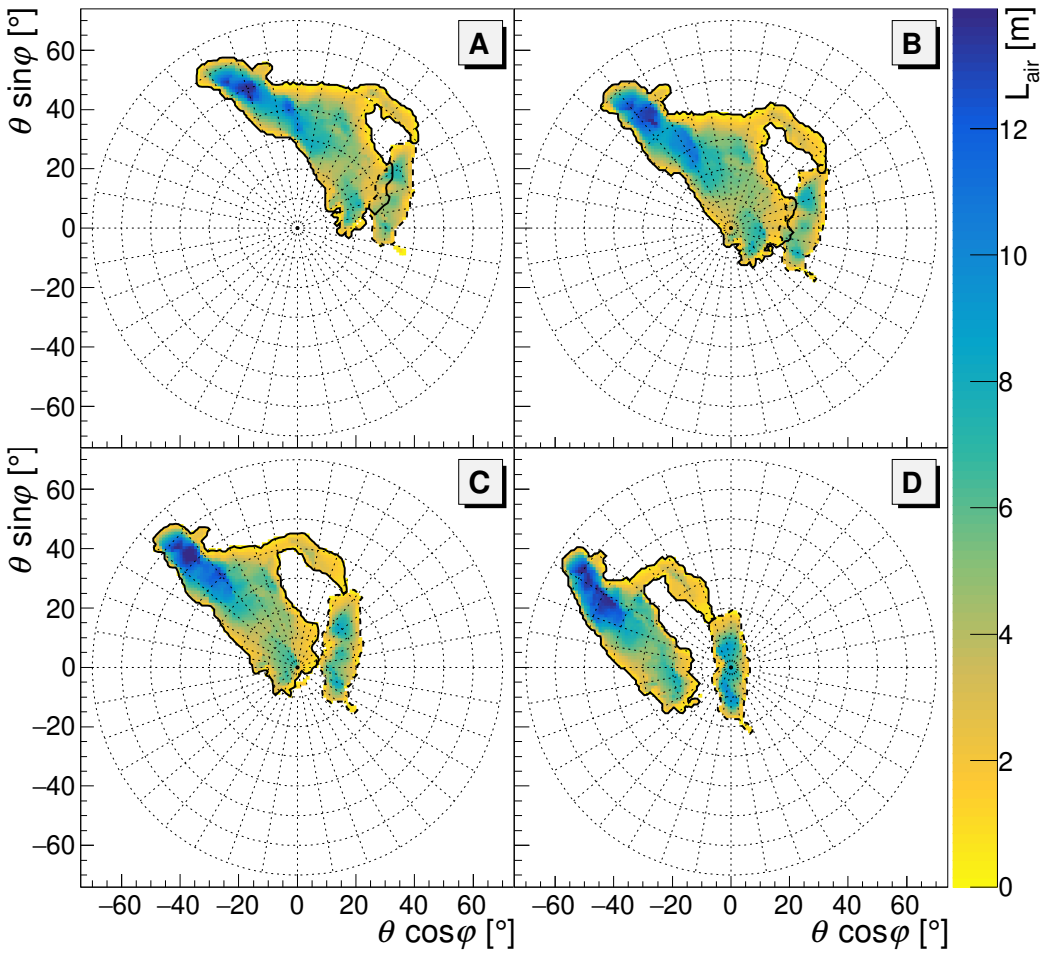

Figure 5.4: Maps of the sum of the air thickness of the Gran Cava and the beam tunnel, from the point of view of the four installation points (A to D) in polar coordinates. The regions with an air thickness greater than zero are delimited by a solid line for the Gran Cava and by a dashed line for the beam tunnel.

are oriented in the same way with respect to the cardinal points (North up, East left, etc.). However, the dimensions of the beam tunnel, which can be observed from the thickness maps in figure 5.4, appear larger than those highlighted in figure 5.3. This is because the mesh of the beam tunnel includes also a portion of the air volume that is already known from the airborne lidar measurements.

As can be seen from figure 5.4, passing from measurement A to D, thus moving in an East-Northeast direction, the relative position of the cavities moves in the opposite direction. As we will see later, the contour lines of the two cavities shown in the figure will be used as a reference for the other muography maps.

A mesh was also created for the tourist gallery where the detector installations were placed, but in this case an angular map of air thickness is not graphically relevant as it would be non-zero in all directions and therefore would not provide information on the arrangement of the gallery itself, since it is seen from the inside. In any case, this analysis allows to correctly evaluate the thickness of the material for each direction (subtracting that of the air in the tunnel) and is therefore necessary to create accurate average density maps.

As can also be seen from the map in figure 5.1b, next to the beam tunnel, there is the entrance to a U-shaped tunnel that initially descends towards the South-East and then reverses direction. Also for this tunnel some surveys were carried out with a 3d scanner for tablet but, given the small size of the initial part of the tunnel, the acquisition did not produce usable results, due to the difficulties encountered in scanning the environment continuously from the external.

5.2 Muon radiography measurements

As described in section 2.2.6, the free-sky measurement was carried out at the INFN in Florence with the detector front pointing towards geographic North. Although the acquisition time for the free-sky measurement (15 d and 18 h) is shorter than the target ones (see table 5.2), for the first one a higher statistic is obtained, given the much higher muon rate, so as to make its contribution to the statistical error negligible.

The reconstructed tracks were symmetrized (see section 2.2.7) in order to eliminate the asymmetry due to the East-West effect. In this way, it was possible to use a single free-sky measurement to obtain the transparency maps for each installation point.

For this work, it was not possible to evaluate the systematic effects due

Table 5.3: The table shows the inefficiencies of the planes (with i from 1 to 6) for the four target measurements and for the free-sky measurement. The inefficiency has been multiplied by a factor 10^4.

Measures	Scaled inefficiency $(1-\varepsilon_i)\cdot 10^4$					
	$i=1$	$i=2$	$i=3$	$i=4$	$i=5$	$i=6$
Free-sky	39.2	0.95	5.1	1.37	5.86	90.4
A	2.29	0.51	15.5	0.82	2.98	16.5
B	1.72	0.53	13.8	0.96	1.66	16.1
C	2.48	1.19	152	1.08	4.99	13.6
D	2.53	0.63	32.7	1.41	1.86	22.7

to the variation in atmospheric pressure: at the time of the free-sky measurement, which will be the most affected by these effects (see section 2.2.5), the detector was not equipped with the measurement system of environmental variables (pressure and temperature).

Table 5.3 shows the inefficiencies $(1-\varepsilon_i)\cdot 10^4$ of each tracking plane i and for all five measurements. These values were obtained after excluding any periods of detector malfunction, associated with a high inefficiency of the tracking planes (for the free-sky measurement a period of about 44 h was excluded). The corresponding data were then excluded from the acquisition time calculation already presented and from the remaining analyses. As can be seen from the reported values, the inefficiencies of the tracking planes are negligible (around 10^{-3} to 10^{-4} for all cases). The highest inefficiency was obtained in measure C for plane 3 where $(1-\varepsilon_3)|_C = 1.52\cdot 10^{-2}$. However this value is still small, so all plans have always been approximated as perfectly efficient.

5.2.1 Muon count maps

Figure 5.5 shows the maps of the muon counts in the polar reference system for all four target measurements. The angular dimension of the pixels ($2^\circ \times 2^\circ$) was chosen according to the following compromise: increasing the pixel size on the one hand improves the resolution in the opacity measure of each pixel, but on the other hand it worsens the angular resolution of the measurements (consequently decreasing the number of Rays).

From the angular distributions of the muon counts in the target configuration, as already discussed for the free-sky map, we observe the decrease in the number of reconstructed tracks as we move away from the vertical due to both the decrease in the transmitted flux and the decrease in the effective

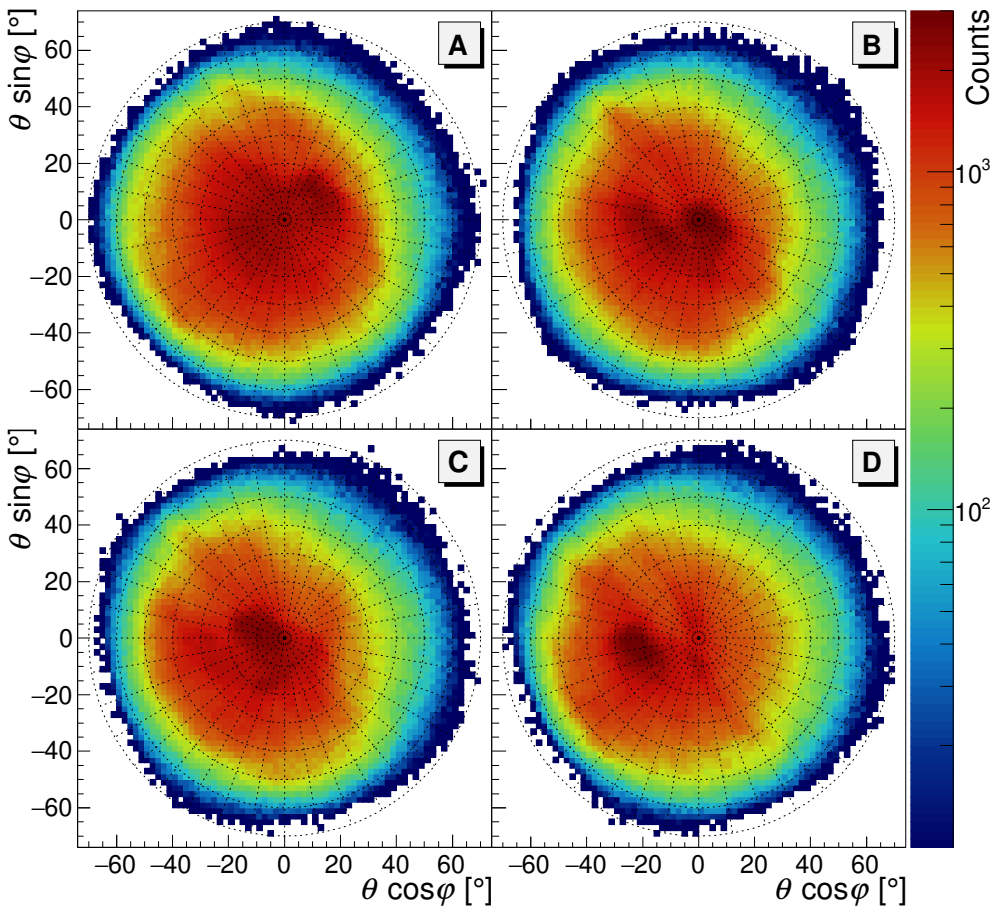

Figure 5.5: Polar maps of the number of reconstructed tracks for the four target measurements.

area of the detector. The slightly squared shape of the maps is due to the geometrical acceptance and it is in agreement with the orientations of the detector shown in table 5.2. Already from these maps, some anomalies related to the shape of the hill and to the presence of the collapse of the Gran Cava can be glimpsed.

5.2.2 Transparency maps

The measured transparency maps (or transmission maps) shown in figure 5.6 were obtained by dividing the maps of the muon counts in the target configuration by the one obtained in the free-sky configuration appropriately rotated and normalizing them for the acquisition times, as expressed in equation 3.2.

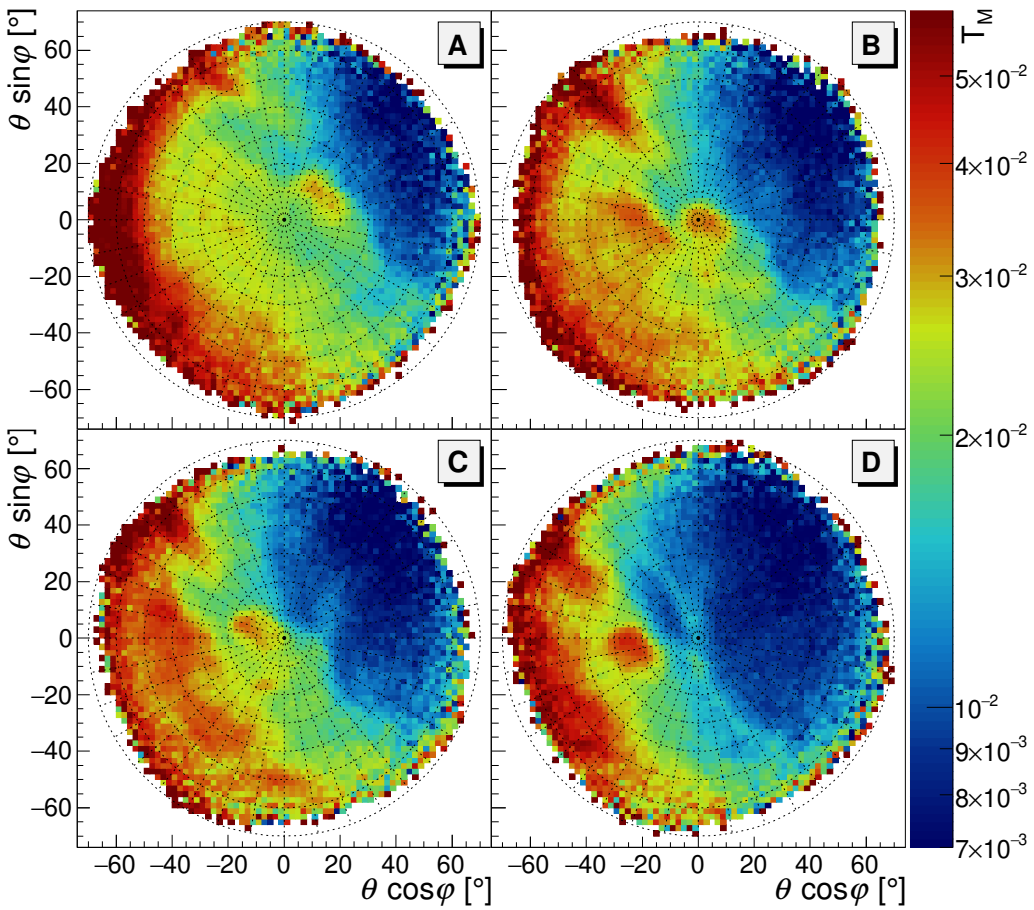

Figure 5.6: Measured transparency maps for the four installations. We observe the increase in transparency in the South-West direction, where the thickness of the hill decreases, and the signal of high transparency of the Gran Cava (in particular of the vertical collapse).

From these images we can clearly observe the increase in transparency in the South-West direction coherently with the decrease in the thickness of the hill in the same direction. In addition to this, however, anomalies related to the conformation of the hill itself and the presence of the Gran Cava (especially its collapse in the South-East) can be seen.

5.2.3 Opacity maps

Using the procedure presented in paragraph 3.2.3 on page 62, the transparency maps were converted to measured opacity maps. In addition to

these, the maps of the measurement uncertainty on opacity were also calculated as expressed by equation 3.9 on page 64. These maps constitute the input for the tomographic inversion algorithms presented in section 4.2, however, since they are more difficult to interpret than the angular distribution of transparency and of average density, they are shown in the appendix B on page 121 in figures B.1 and B.2.

5.2.4 Average density maps

Finally, as an additional two-dimensional analysis, the mean density maps reported in figure 5.7 were created. To present these maps an average filter was used which reduces the fluctuations by highlighting the signals. This filter was not used in the previous maps because it would greatly complicate the calculation of the measurement error for each pixel, but it is presented for density maps that are not part of the tomographic analysis process. In the angular regions where there is a low statistic (usually at the edge of the angular acceptance), this filter can lead to the creation of apparent signal zones due to statistical fluctuations.

These maps are easier to interpret and directly show anomalies associated with cavities or high-density volumes, regardless of the specific shape of the hill. In fact, a decrease in the average density can be observed in correspondence with the directions with a significant air thickness of the known cavities. As a reference, the contour lines of the known cavity thickness maps (see figure 5.4) were superimposed, which effectively delimit regions of low average density.

To obtain the maps described above, the thickness map of the hill was calculated from the lidar, having also subtracted the air thickness of the installation tunnel.

Repeating the same procedure, but also subtracting the air thickness of all the known tunnels (Gran Cava and beam tunnel), we obtain the average density maps shown in figure 5.8, in which the signal due to the main volume of the Gran Cava disappears. At the same time, low-density regions (probably due to further cavities) and high-density regions (intercepting dense rock volumes such as skarn) are still visible.

In these latest maps there is always a residual low-density signal in correspondence with the collapse of the Gran Cava: this effect is probably due to a portion of the volume of air of the Gran Cava that is missing in the simulations. In fact, in the laser scanner surveys, since they were not carried out from the outside of the collapse, the points of the wall facing South of the vertical exit of the Gran Cava are missing. Both the meshes of the Gran Cava and the lidar of the hill are missing a portion of air which is therefore

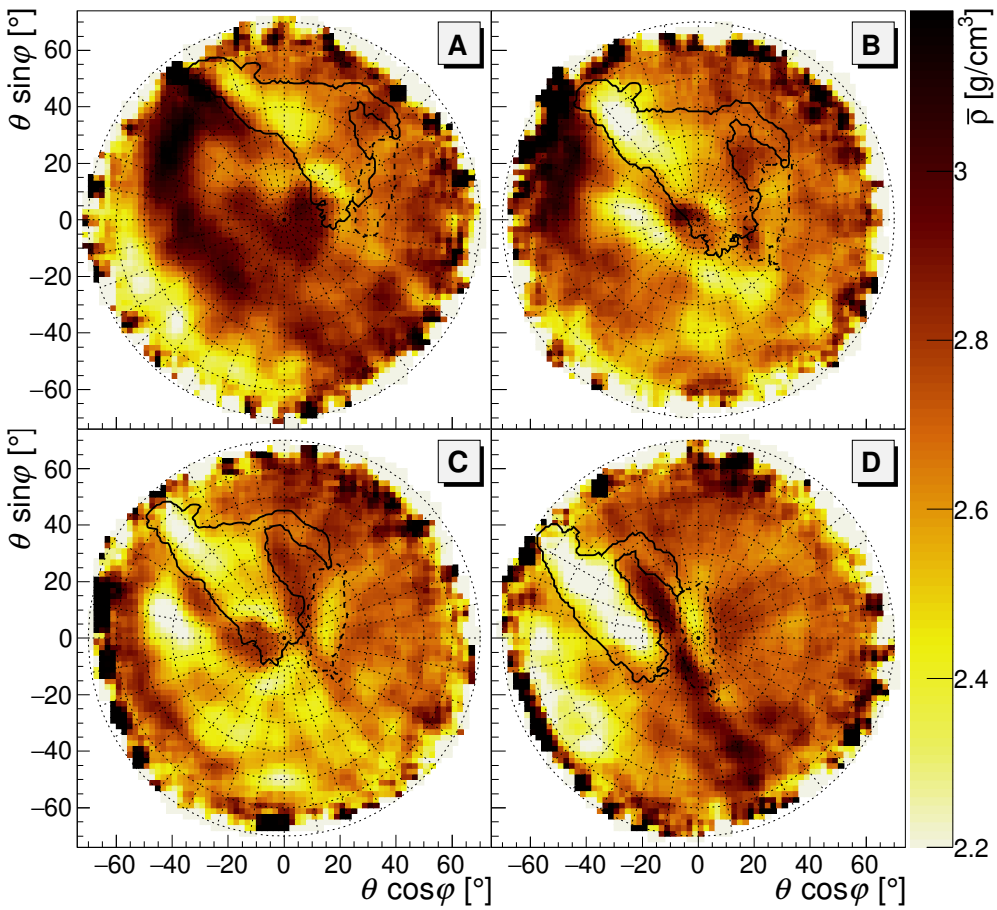

Figure 5.7: Average density maps in the polar reference frame. The contours of the Gran Cava and of the beam tunnel are also shown, as obtained in figure 5.4. It is observed that the contour lines actually delimit angular regions of low average density. A smoothing filter was used for these maps: the content of each pixel is replaced by the average of the 9 adjacent pixels.

correctly interpreted as a cavity. This signal is less visible in measurement B due to the use of the filter and to the relative measurement position.

The use of these average density maps already presupposes the knowledge of the geometric model of the target and in particular of the thickness maps of the material crossed by the muons. For this reason, the density maps are not suitable to be used for tomographic inversion algorithms (which instead use opacity maps): in each tomographic reconstruction, the subdivision of the World into finite-sized Voxels involves small variations in the material thickness maps that must be recalculated based on the specific configuration.

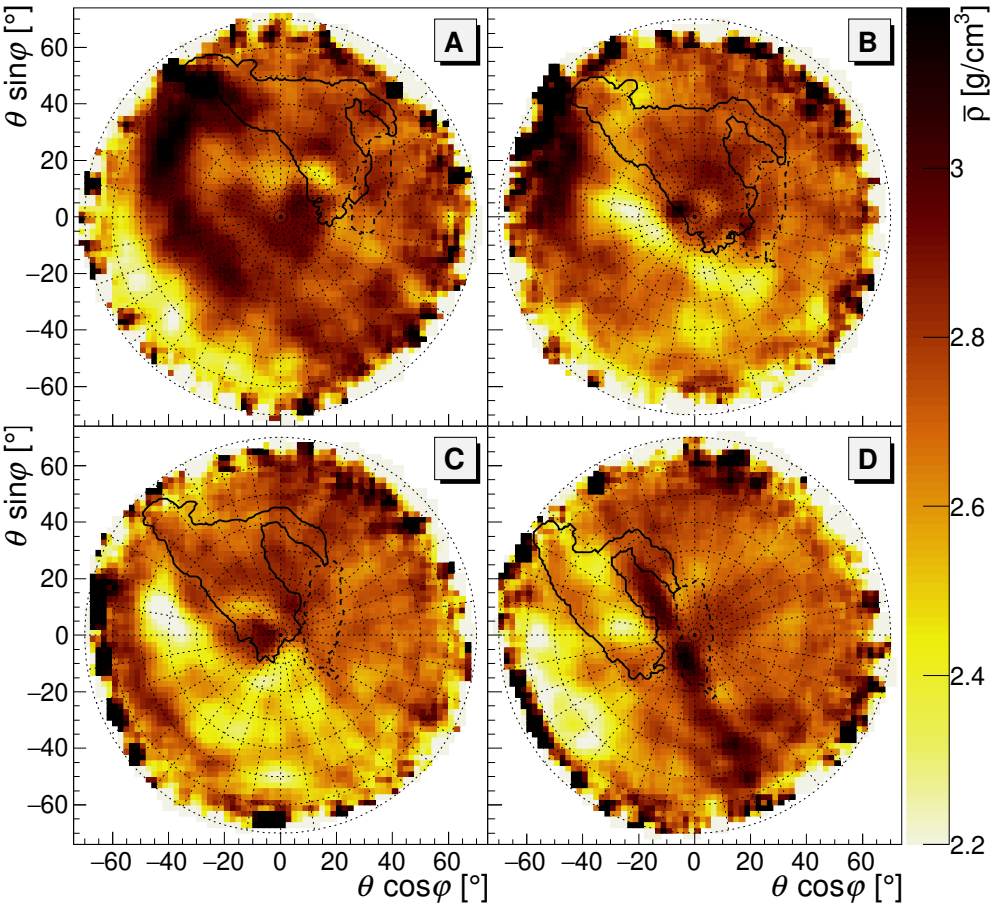

Figure 5.8: Average density maps (with smoothing filter) obtained by subtracting the known air thickness of the Gran Cava and the beam tunnel to the total material thickness. The contours of the Gran Cava and of the beam tunnel are shown, but, comparing with the maps of the previous figure, most of the low density signals relative to the two cavities have correctly disappeared. In any case, various low-density angular regions remain which can be associated with the presence of further unmapped cavities.

5.3 Tomography reconstruction

The objective of the measurements presented above is to carry out a tomographic study of this portion of the Temperino mine. In particular we will focus on the reconstruction of the Gran Cava in order to test the algorithms presented above and then we will focus on identifying other unknown cavities of which we have indications from a previous work [33].

5.3.1 Initialization of the problem: World, Voxels and Rays

First of all, the Rays are defined: each pixel of the opacity maps presented above corresponds to a Ray and defines the geometry of the associated solid angle and the opacity measure. To eliminate problems related to excessive statistical fluctuations, Rays with an average zenith angle greater than 60° are excluded.

Then the dimensions and position of the World are established, which depend on the geometry of the measurements and that of the hill. The World has the shape of a rectangular parallelepiped, or cuboid, with the faces parallel to the x, y and z axes of the global reference system (see paragraph 2.1.1 on page 31 for the definition of the global reference system). To completely define the World, with the exception of its internal division, it is sufficient to define two opposite vertices of the World (its bounding box). Once this is done, the size of the Voxels is established, which will have the shape of a cuboid (but usually they are cubic), and the World is divided into the corresponding Voxels[5].

The knowledge of the morphology of the hill above the mine and of the installation tunnel, which are not the objective of the investigation, is then introduced. Those Voxels that are made of air are identified (the procedure is explained below) and they are assigned a constant zero density. At this point we calculate the intersection length of the Rays with all the Voxels that are not made of air. This procedure is explained in more detail in paragraph 5.3.1 on page 100.

The dimensions of the World, and consequently the choice of the two vertices that define it, must be large enough: the lower surface of the World must be at a lower altitude than the minimum altitude of the MIMA installations, and it is required that the Rays always cross a portion of air before

[5]If, for a certain direction (x, y or z), the dimension of the World is not divisible by that of the Voxel, the dimension of the World is increased to the first integer multiple of the Voxel length.

exiting the World itself (the last intersected Voxel must be made of air), otherwise the dimensions of the World must be increased.

A slicing method is presented below to create sections of the tomographic reconstruction that allow to illustrate what has been discussed so far. After that the algorithm for selecting the Voxels in air and for calculating the lengths of the Ray-Voxel intersection are described in more detail.

3D slicing

For this work, a slicing tool was developed to slice the World and show some characteristics of the selected Voxels. The sections are perpendicular to the directions of the axes of the global reference system and the software allows you to interactively scroll the position of the slice.

For each Voxel, based on what has already been discussed above, the following characteristics are defined, which can be shown with the slicing tool:

- whether the Voxel is made of air or not;
- whether the Voxel is part of the tomographic reconstruction;
- the reconstructed density, ρ_j;
- the density provided by the model, ρ_j^{mod} (if a model exists for the Voxel densities);
- the number of measurements from which a certain Voxel is observed;
- the number of Rays from which a certain Voxel is intersected.

For the slicing software, the origin of the global reference system (x, y, z) has been chosen to coincide with the measurement point A. In the slices presented, the installation points are marked by black triangles ordered from A to D in the x direction (eastward).

The slice in figure 5.9 shows the number of measurements from which each Voxel is observed. In this case, cubic Voxels with 3 m edge have been chosen. The vertical sectioning plane has equation $y = 6$ m and is observed in the North direction. The image shows the acceptance cones of the measures, which have been reduced to an angular half-opening of 60° with respect to the vertical. In this figure, as in all those that we will see later, the morphology of the hill is highlighted: the Voxels that have been identified as made of air (see paragraph 5.3.1 on page 99) are excluded from all analysis processes. In this way we can observe the shape of the hill that slopes towards the West

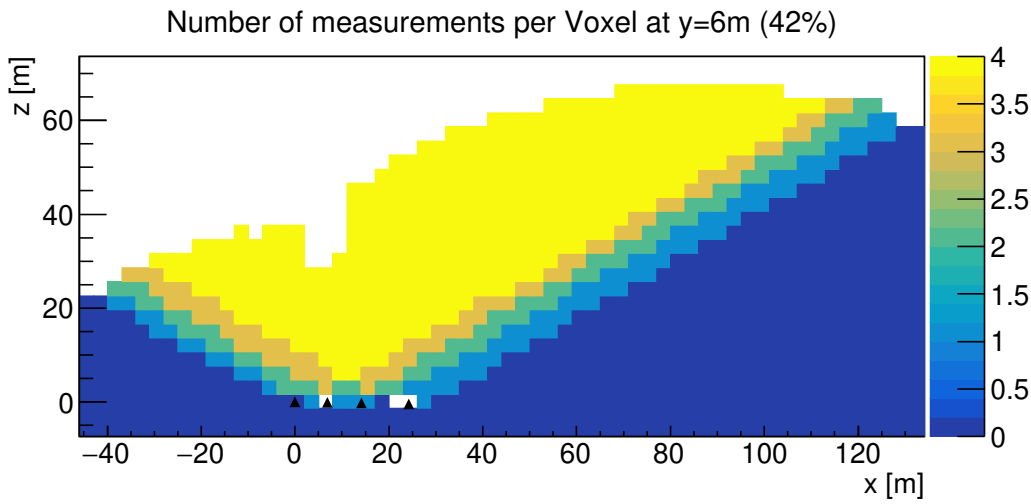

Figure 5.9: The slice shows the number of measurements from which each Voxel is observed. Cubic Voxels with a 3 m edge were chosen. The black triangles indicate the location of the four installations and point A (the first triangle from the left) was chosen as the origin of the reference system (x, y, z). The sectioning plane is vertical and has equation $y = 6$ m and is view towards the North. The morphology of the hill (collapse of the Gran Cava and decreasing altitude towards the West) and the acceptance cones for the four measures can be noticed.

(or in the negative direction of the x axis) and the collapse at the exit of the Gran Cava, which is correctly placed above measure B (the second triangle from the left in figure).

Selection of Voxels and Rays

As can be seen from figure 5.9, some Voxels are observed only by a single measure and there will be some Rays that cross only Voxels of this type. These Rays are not useful for carrying out a real tomographic reconstruction and will therefore be excluded.

The selection process chosen, however, is even more strict and its result is shown in figure 5.10 (the characteristics of the Voxels and the slice are the same as in figure 5.9 to ease the comparison): only the Rays that have crossed at least one Voxel observed by all four measurements are selected. This determines the total number of selected Rays I. Therefore, in the tomographic reconstruction, only the Voxels intersected by the Rays thus identified are considered.

For the configuration shown in figure 5.10, with Voxels of size $(3 \times 3 \times 3)\,\mathrm{m}^3$,

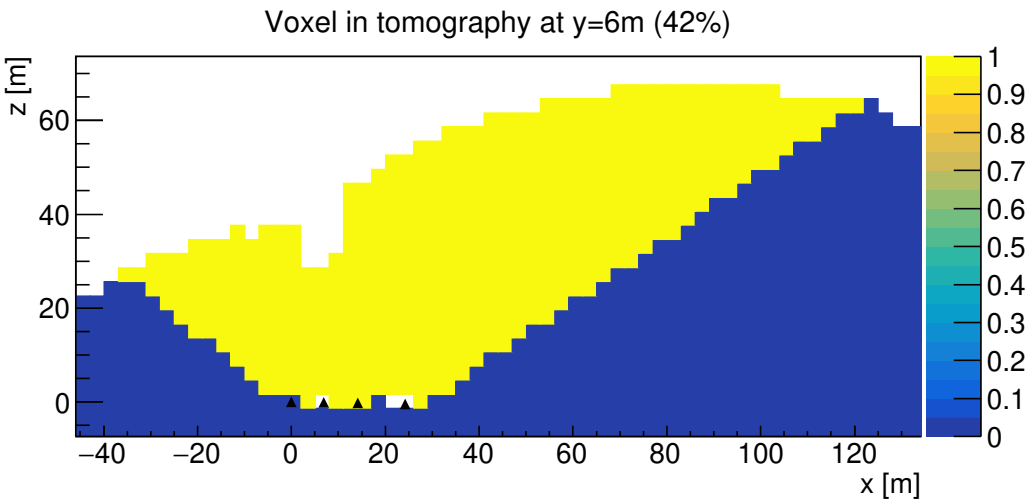

Figure 5.10: The slice shows which Voxels are included in the tomographic reconstruction algorithm (in yellow) and which are not (in blue). The size of the Voxels and the geometry of the slice is the same as in figure 5.9. Comparing that slice with this one, it is observed that some Voxels near the edges of the acceptance have been excluded.

we obtain a number of selected Rays and Voxels equal to $I = 10838$ and $J = 21513$. As described later, however, larger Voxels are sometimes used. For cubic Voxels with an edge of 6 m we get $I = 11159$ and $J = 3336$. By increasing the size of the Voxels, J decreases and I remains substantially unchanged.

Air volumes known a priori

This section describes how the geometric and morphological characteristics of the hill above the mine and of the Temperino gallery are introduced. In the same way it is also possible to introduce the geometry of other known cavities as the Gran Cava and the beam tunnel.

To do this it is necessary to identify which Voxels are completely (or predominantly) composed of air using the two geometric models available: the lidar relief of the hill and the meshes of various tunnels.

Through a bilinear interpolation of the data grid provided by the airborne lidar, the elevation of the hill, z_{hill}, is expressed as a continuous two-dimensional function of the x and y coordinates as $z_{\text{hill}}(x, y)$. Therefore a Voxel is assumed to be made of air, if the z_c coordinate of its geometric center (x_c, y_c, z_c) is greater than the altitude of the hill at that point, i.e. if $z_c > z_{\text{hill}}(x_c, y_c)$. The result of this algorithm has already been observed in

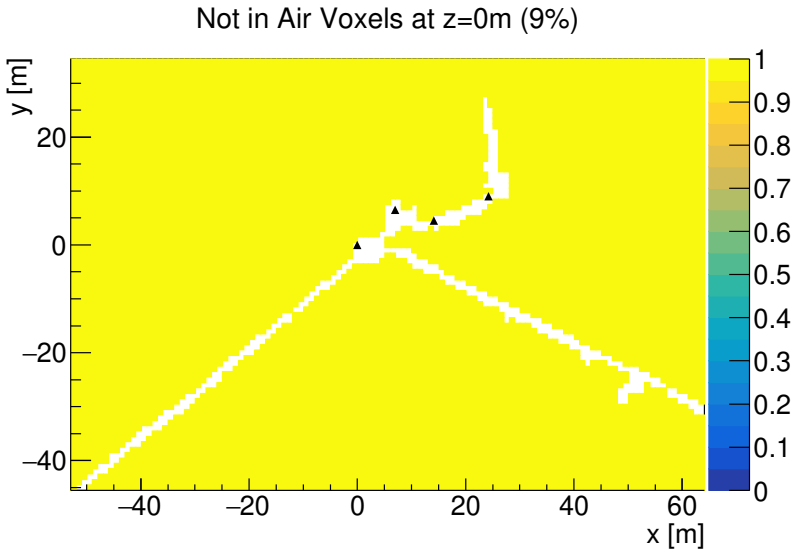

Figure 5.11: The slice presented is seen from above and is arranged horizontally at the altitude of the installation points. The Voxels that have been identified as made of air (whose geometric center is inside the mesh of the Temperino tunnel) are shown in white, while the Voxels that are inside the ground are in yellow. In this case, cubic Voxels with a 1 meter edge, smaller than those shown previously, had to be used to accurately show the shape of the tunnel. The similarity with the black tunnel in figure 5.3 can be observed.

figures 5.9 and 5.10 seen above.

In the case of a closed mesh of a known volume of air, such as the detector installation tunnel, the procedure is similar: each Voxel whose geometric center is inside the mesh is assumed to be entirely made up of air. Figure 5.11 shows the result of the identification of the air Voxels for a horizontal slice that cuts the Temperino tunnel where the installations are located.

The algorithms described above are rather simple but still allow to reconstruct the known geometries of the problem. A more precise, but much more complex solution would be to evaluate the percentage of air in each Voxel. The precision with which the described algorithm is able to reproduce the geometry of the air volumes is proportional to the size of the Voxels: the smaller the Voxels, the better the precision. A better alternative is presented a few paragraphs later.

Ray-Voxel intersection length

In equation 4.1, L_{ij} is defined as the mean length of intersection between the jth Voxel and the ith Ray. In the event that a Ray geometrically corresponds

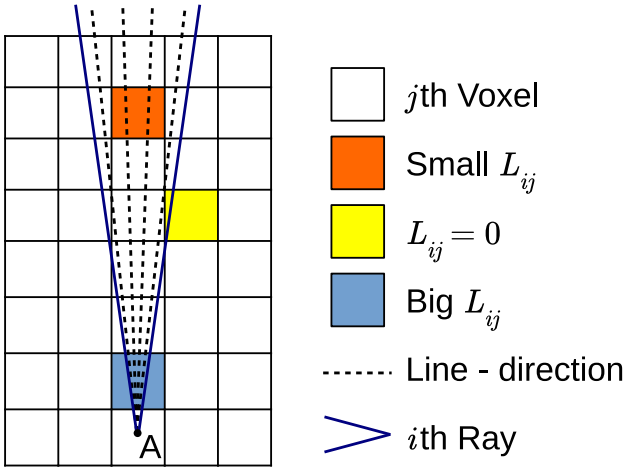

Figure 5.12: Schematic representation in a two-dimensional case of the calculation of the intersection length, L_{ij}, of the ith Ray with the jth Voxel. The directions inside the Ray are equally spaced. The blue Voxel, which is closer to the measurement point (point A in the figure) than the orange one, is crossed by a greater number of directions inside the Ray and has a greater intersection length. The yellow Voxel is at the edge of the Ray and, although geometrically intersected, it has a zero intersection length. The angular width of the Ray is not to scale.

to a precise rectilinear direction, L_{ij} could simply be calculated as the length of the intersection segment between the line of the ith Ray and the cuboid of the jth Voxel. However, as we have seen, a Ray corresponds geometrically to a solid angle. Its intersection length with a Voxel can therefore be calculated as the average of the intersection lengths of a series of directions within the solid angle of the Ray. For convenience, the chosen directions are uniformly distributed within the solid angle of the Ray, according to the polar reference system (a uniform grid is defined which further subdivides the pixel of each Ray). The minimum distance between two directions inside a Ray is chosen in such a way as to intersect at least once all the Voxels that are in the acceptance of the Ray (except those close to the edges).

Figure 5.12 shows a schematic drawing of a Ray and of the selected internal directions in the two-dimensional case. From the figure it can be observed that the intersection length on average decreases as the distance of the Voxel from the starting point of the Ray (i.e. the installation point of the detector for the corresponding measurement) increases, since the solid angle subtended by the Voxel decreases.

For the same reason, the Voxels close to the installation points are also

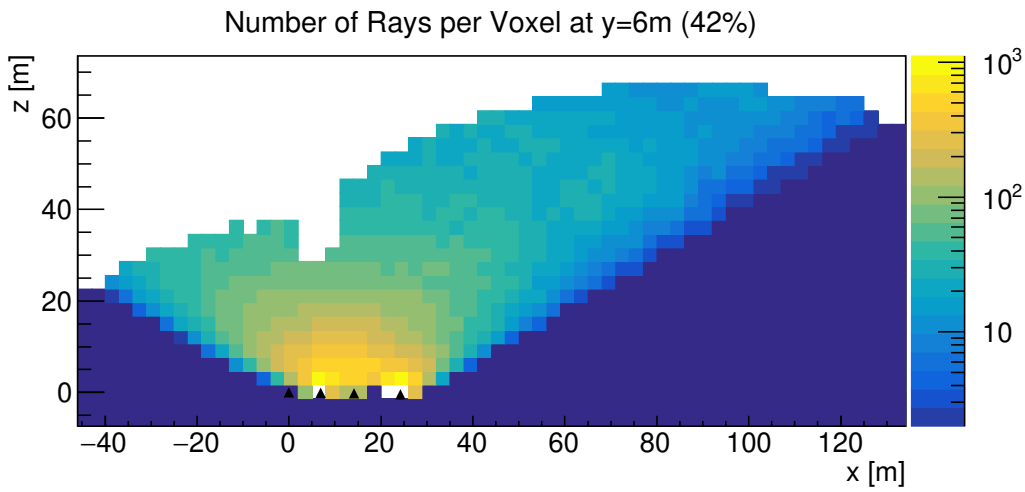

Figure 5.13: The slice and the size of the Voxels are the same as in figures 5.9 and 5.10, but in this case for each Voxel the number of intersected Rays is shown. The Voxels closest to the installation points cover a larger solid angle and therefore are crossed by a greater number of Rays.

crossed on average by a greater number of Rays than the more distant Voxels. This is also what can be seen in the slice of figure 5.13 which shows the number of Rays that intersect each Voxel.

The method of calculating the intersection lengths presented above would also allow taking multiple scattering into account. In [33] a simplified simulation of one of the measurements presented in this work was carried out, obtaining an average multiple scattering angle of 1.5°. The straight lines used for the calculation of the intersection lengths could be generated according to a suitable distribution function whose angular amplitude takes into account not only the solid angle associated with each Ray, but also the dispersion due to the above Coulomb multiple scattering.

MacroVoxel

As we have seen in paragraph 5.3.1 on page 99, to accurately reproduce the geometry of the hill above the Temperino mine it is necessary to define Voxels with a sufficiently small size. The decrease in the size of the Voxels is however limited by the solvability of the inversion problem. The smaller the Voxels, the greater the total number of Voxels of the inversion problem J, the greater the unknowns and the more the inversion problem becomes computationally challenging (especially with the minimum of Chi-squared method). The choice of the Voxel size therefore also depends on the computational

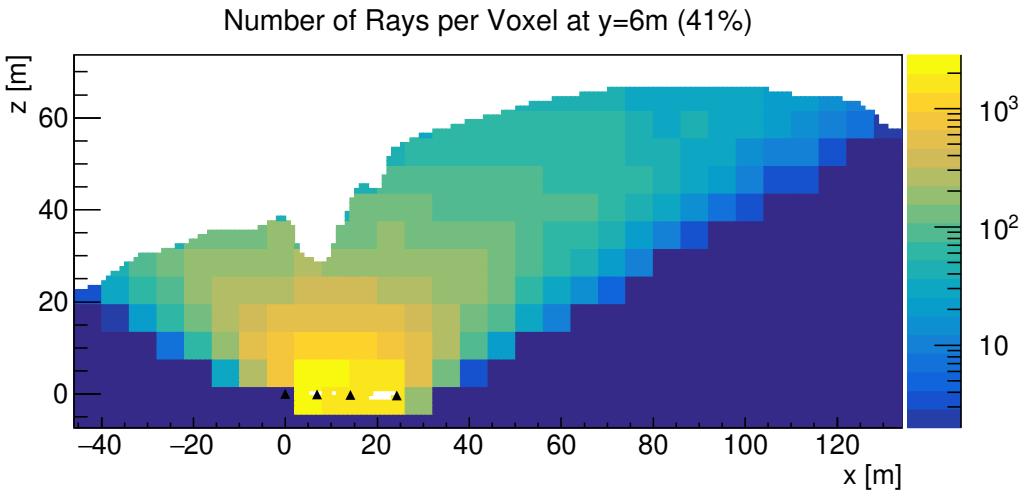

Figure 5.14: This slice and its content are the same as that in figure 5.13 (the number of Rays that have crossed each "Voxel" is reported), but here cubic MacroVoxels with a 6 m edge and with 1 m edge cubic microVoxels have been used. Thanks to the use of MacroVoxels, the geometry of the hill is reproduced in a much more precise way than in figure5.13, although the total number of unknowns is about six times smaller ($I = 11163$ and $J = 3802$).

complexity: in this work for the Chi-squared minimization technique, Voxels no smaller than 4 meters of edge are used, while for the SART algorithm and for the triangulation smaller Voxels can also be used. By choosing Voxels of this size, however, systematic effects arise due to the incorrect reconstruction of the morphology of the hill, which disappear by reducing the size of the Voxels at the cost of much higher computational times.

To make the accuracy of the geometric reconstruction independent of the size of the Voxels, MacroVoxels are introduced. MacroVoxels are Voxels in turn formed by a 3d matrix of smaller cuboids (microVoxels) which allow to better reproduce the morphology of the soil without increasing the number of unknowns. A MacroVoxel that is completely inserted into the ground (or completely in the air) will be in all respects the same as a Voxel. Instead a MacroVoxel that is half in the air and half in the ground, will contain microVoxels composed of air that are excluded from the calculation of the intersection length with the Rays.

The effect of what has been described is shown in figure 5.14 which presents a resolution of the geometry of the surface better than in figure 5.13 although the size of the MacroVoxels is bigger.

Simulated tomography

As we have discussed, the study of the Temperino mine presents numerous complications such as the presence of materials with very different densities and a myriad of unmapped tunnels. To test the tomographic inversion algorithms in a simplified case, reconstructions were carried out starting from a simulated model in which the mine had a uniform simulated density and only the Gran Cava could be present as a cavity to be identified.

To do this, we start by defining the World and setting as composed of air those Voxels that we know are either above the hill or inside the installation tunnel. Therefore all the other Voxels are assigned an initial and a simulated density (or model density) equal to a certain constant value $\rho_0 \approx 2.8\,\mathrm{g/cm^3}$. If the Gran Cava is also to be simulated, a null simulated density is assigned to the Voxels located inside the cavity. In this case the model density of equations 4.4 corresponds to the value of the simulated density of each Voxel, $\rho_j^{\mathrm{mod}} = \rho_j^S$ (and the same thing applies to the error on the density).

Using the simulated density values and the intersection lengths L_{ij} previously calculated, the ith Ray is assigned an opacity given by the formula

$$X_i = \boldsymbol{L}_i \cdot \boldsymbol{\rho}^S + r_{\mathrm{gaus}}(\mu = 0, \sigma = \sigma_{Xi})\,,$$

derived from equation 4.1 on page 70, where $\boldsymbol{\rho}^S$ is the vector of the simulated densities (or model densities) and r_{gaus} is a random number with Gaussian distribution (with zero mean and sigma equal to σ_{Xi}) and serves to add a Gaussian fluctuation to make the simulation realistic. For simplicity, for the uncertainty values, σ_{Xi}, those actually measured were taken. Once the opacities of the Rays have been initialized in this way, it is possible to apply the tomographic algorithms presented in a known and controlled case.

The tomographic problem obtained in this way is quite realistic, except for the fact that the initial model from which the opacities of the Rays are calculated is divided and quantized in the same Voxels used for the tomographic reconstruction. In a real case, on the other hand, there are always some Voxels which are partly made of rock and partly inserted in a cavity to be identified. As a further refinement the opacities could be calculated with a finer model (a World with smaller Voxels) than the one used for the reconstruction and measurement uncertainty could also be derived directly from the model.

5.3.2 Tomographic inversion

Below, the inversion algorithms described in section 4.2 are applied to the tomographic reconstruction of the Temperino mine.

Minimum of Chi-squared

As previously discussed, the Chi-square minimization algorithm becomes rather slow by reducing the size of the Voxels and consequently increasing their number, J (as a first approximation, the number of Voxels is inversely proportional to the volume of each of them). For the minimization process we used the Migrad algorithm of Minuit2, a gradient descend algorithm with variable metrics [51, 75], implemented in the ROOT library. Instead of letting the gradient be calculated numerically, the analytic gradient of the function to be minimized was implemented, so as to reduce the convergence times. Furthermore, the calculation of the Chi-square function and the gradient function has been developed with multitreading techniques to further reduce the computational time.

The Migrad algorithm at the end of the minimization process calculates the covariance matrix of the Voxel densities which allows to determine the density measurement uncertainty. To do this it is necessary to calculate the inverse of the Hessian matrix (i.e. the matrix of the second derivatives of the minimized function) of dimension $J \times J$. The inversion algorithm has a complexity $\mathcal{O}(J^3)$. For cubic Voxels with a 7 m edge, an inversion time, t_{inv}, equal to 51 s is obtained, while for Voxels with a 4 m edge you would get $t_{\text{inv}} \approx 130$ min. To reduce the computational time, we preferred to avoid calculating the covariance matrix.

The Chi-square minimization algorithm was applied to a simulated tomography (without the introduction of the Gran Cava) with a World made of cubic Voxels with a 7 m edge. The result of the reconstruction is shown in the two vertical slices of figure 5.15. In the figure 5.15a only the minimization of the opacity Chi-square was used: the formation of two horizontal bands with different average density is observed, as foreseen in section 4.1.1 on page 70, and the Voxels at the edge of the acceptances show significant density fluctuations. Both problems can be solved by imposing a minimization of the total Chi-square given by the sum of the opacity term plus the volume term as shown in figure 5.15b (the vertical scales of the two images are different). For this second simulated tomography the following parameters for the regularization term have been used: $\alpha_V = 1$, $\rho_j^S = \rho^S = 2.8\,\text{g/cm}^3$ and $\sigma_j^S = \sigma^S = 1\,\text{g/cm}^3$.

Then another simulated tomography was performed with cubic Voxels with an edge of 4 m, this time setting the simulated density of the Voxels inside the Gran Cava to zero, and leaving the other parameters unchanged. The result is shown in a horizontal slice that cuts the Gran Cava in figure 5.16a. In this tomography it was possible to correctly reconstruct the low density values of the Voxels whose center is inside the Gran Cava, whose

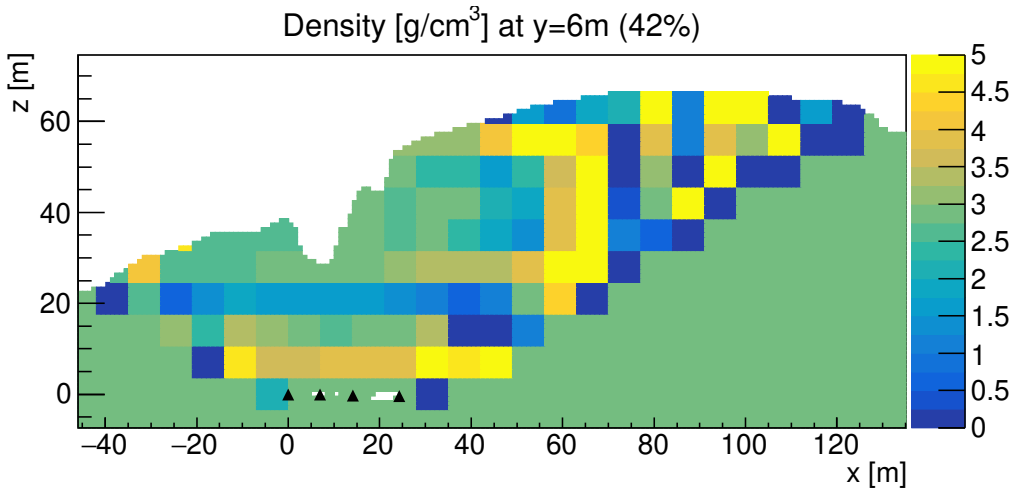

(a) Chi-square minimization without regularization term: $\chi^2_{\mathrm{TOT}} = \chi^2_X$.

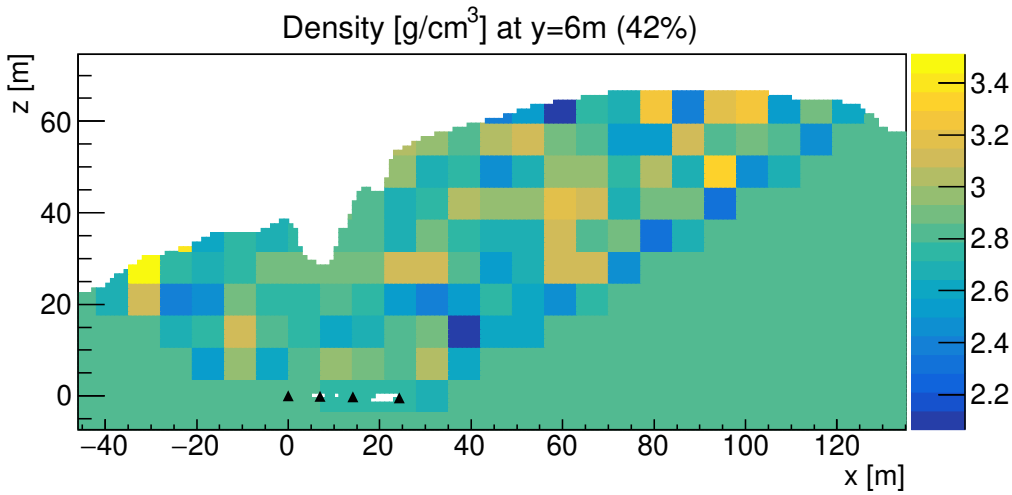

(b) Chi-square minimization with the volume regularization term: $\chi^2_{\mathrm{TOT}} = \chi^2_X + \chi^2_V$.

Figure 5.15: The two vertical slices show the result of two simulated tomographies obtained with the Chi-square minimum method. In figure (a) no regularization term has been used and two horizontal bands of opposite density are observed as expected from the theory (see figure 4.1 on page 71). Furthermore, the density values of the Voxels near the edges, where the opacity measurement is less precise and there is less tomographic information, fluctuate clearly and reach the limit values of $0\,\mathrm{g/cm^3}$ and $5\,\mathrm{g/cm^3}$. For the minimization presented in figure (b) a volume regularization term was used which eliminates the previous problems. Note that the two color palettes have two different ranges.

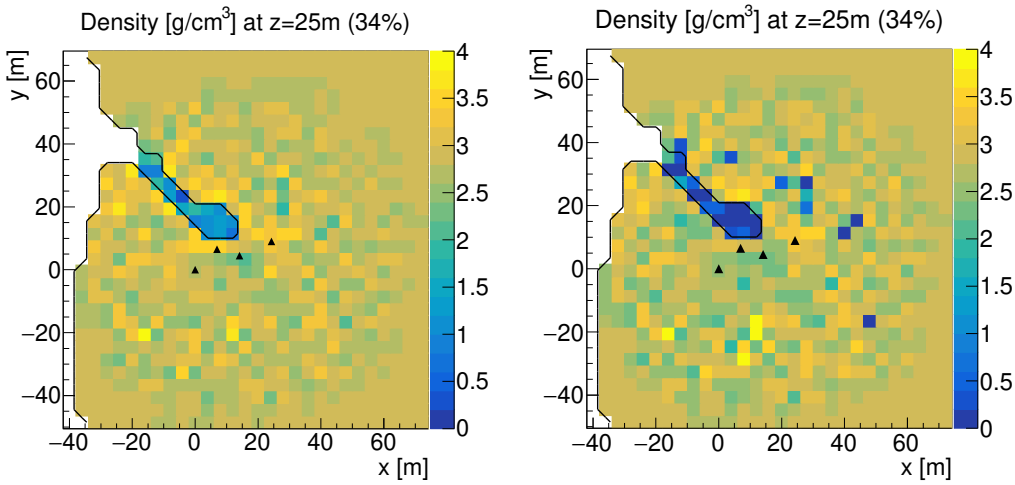

(a) Old regularization.

(b) New regularization.

Figure 5.16: The result of two simulated tomographies that make use of different regularization terms. The two horizontal slices cut the Gran Cava. The black line delimits the Voxels which have a zero simulated density while for the other Voxels we have $\rho^S = 2.8\,\mathrm{g/cm^3}$. In the reconstruction on the right, whose regularization term is explained later in the text, the reconstructed density of the Voxels inside the Gran Cava is closer to zero.

simulated density is zero, which are delimited by the black line. However, the density values of these Voxels are still not close to zero. This is precisely due to the volume regularization term which, if on the one hand leads to significant improvements (see figure 5.15), on the other hand it penalizes densities that are too different from the simulated density value, ρ^S. For this reason, a volume regularization term has been developed that favors both density values close to the average density of the rock and those close to zero that are associated with the presence of cavities.

In general the n allowed density values (in this case $n = 2$) will be listed, in ascending order, in the vector $\tilde{\boldsymbol{\rho}} = (\tilde{\rho}_1, \ldots, \tilde{\rho}_n)$ (for continuity the same nomenclature of the density vector used for the DART algorithm in paragraph 4.2.2 on page 74 is used). Then the volume regularization function presented in equation 4.4 is modified as follows:

$$\chi_V^2 = \sum_{j=1}^{J} f(\rho_j; \tilde{\boldsymbol{\rho}}, \sigma), \tag{5.1}$$

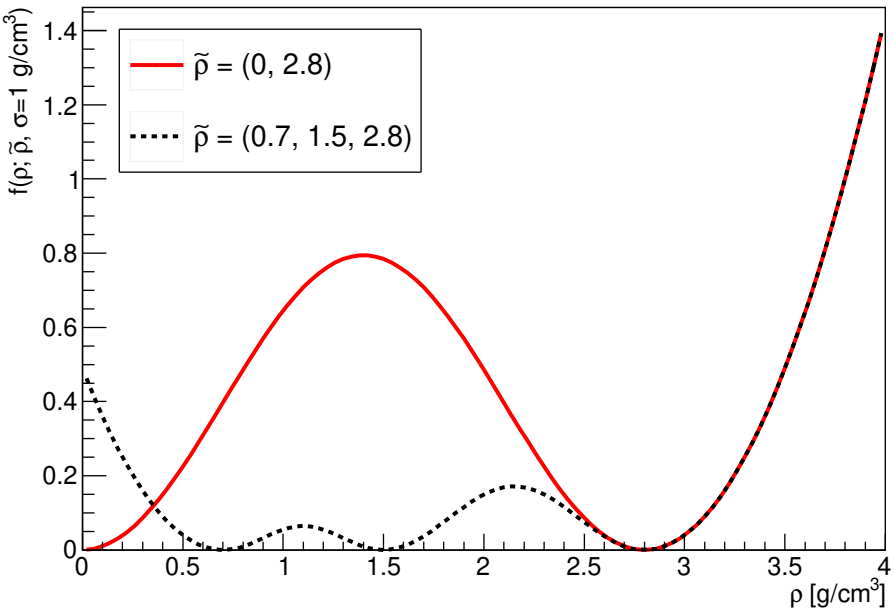

Figure 5.17: The potential-like function $f(\rho; \tilde{\boldsymbol{\rho}}, \sigma)$ is represented for two sets of values of the allowed densities $\tilde{\boldsymbol{\rho}}$ and for $\sigma = 1\,\mathrm{g/cm^3}$.

where f is the following potential-like function:

$$f(\rho; \tilde{\boldsymbol{\rho}}, \sigma) = \begin{cases} \left(\dfrac{\rho - \tilde{\rho}_1}{\sigma}\right)^2 & 0 < \rho < \tilde{\rho}_1, \\ \left(\dfrac{\Delta\tilde{\rho}_i}{\sigma}\right)^2 \sin^2\left(\dfrac{\rho - \tilde{\rho}_i}{\Delta\tilde{\rho}_i}\right) & \tilde{\rho}_i < \rho < \tilde{\rho}_{i+1}, \\ \left(\dfrac{\rho - \tilde{\rho}_n}{\sigma}\right)^2 & \rho > \tilde{\rho}_n, \end{cases} \tag{5.2}$$

where $\Delta\tilde{\rho}_i = (\tilde{\rho}_{i+1} - \tilde{\rho}_i)/\pi$.

Figure 5.17 shows the function $f(\rho; \tilde{\boldsymbol{\rho}}, \sigma)$ for two sets of values of the allowed densities $\tilde{\boldsymbol{\rho}}$, with $\sigma = 1\,\mathrm{g/cm^3}$. The red line indicates the potential function actually used in this work. It is observed that the function is defined in such a way that the second derivative in any minimum is constant. However in this way, by increasing the number of allowed densities, the function becomes substantially flat and loses its effectiveness (note the dashed black line).

By applying this new regularization term, the result shown in figure 5.16b is obtained, where again the Voxels that have a simulated density equal to zero have been highlighted with a black line. By doing so, the density of

such Voxels approaches much closer to zero than it previously did. However, at the same time, some isolated Voxels with zero density are erroneously reconstructed.

All the results shown for the Chi-square minimization technique refer to simulated tomographies and unfortunately it was not possible to obtain satisfactory results by applying this technique to the real measurements.

SART

The SART algorithm with respect to Chi-square minimization is faster and allows the use of smaller Voxels. In the results presented below we will use cubic MacroVoxels and microVoxels with 2 m and 1 m edge respectively. In this way we obtain a number of Rays and Voxels equal to $I = 10680$ and $J = 69022$.

The results obtained by applying 400 iterations of the SART algorithm are presented below, having chosen an initial density equal to $2.8\,\mathrm{g/cm^3}$. This value is in agreement with what is reported in the regions that are presumed to be without cavities in the average density maps of figures 5.7 and 5.8 on page 95 and with the typical rock values of the mine (see table 5.1 on page 79). The number of iterations, N_{it}, is chosen on the basis of a convergence criterion: by increasing the number of iterations, the variation of the opacity Chi-squared, which measures how well the tomographic reconstruction is in agreement with the opacity measurements, becomes negligible. For the number of interactions chosen, $N_{\mathrm{it}} = 400$, we have

$$\frac{\partial \ln \chi_X^2}{\partial N_{\mathrm{it}}} = \frac{\partial \chi_X^2}{\partial N_{\mathrm{it}}} \frac{1}{\chi_X^2} < 1.5 \cdot 10^{-3}.$$

Figure 5.18 shows two slides, one horizontal at the height of the Gran Cava and a vertical one passing near the detectors.

In slice 5.18a it is possible to delineate the shape of the Gran Cava and we can see the signals of other unknown cavities. However, the density values obtained for these regions are still well above zero. This is due to the fact that the algorithm tends to modify all the Voxels which are observed in the same direction as the Gran Cava forming a sort of trail, as shown on figure 5.18b. Furthermore, the Voxels closest to the detector are the most modified. These in fact, as seen in paragraph 5.3.1 on page 100, on average have a greater length of intersection and are crossed by a greater number of Rays. As described in section 4.2.2 these two aspects both lead to an increase in the density variation term of formula 4.8.

In order to try to reduce the dependence of the density variation on the number of Rays that cross each Voxel, we tried to use the local normalization

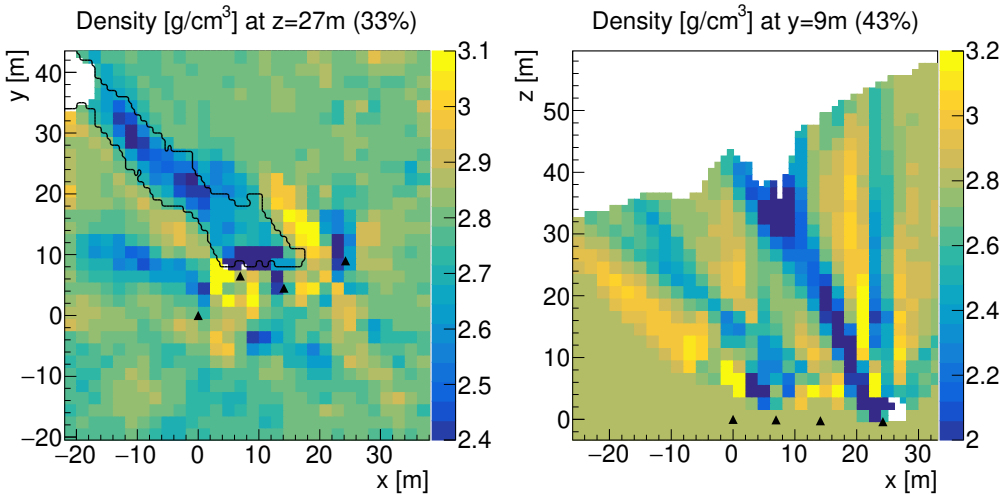

(a) Horizontal slice. (b) Vertical slice.

Figure 5.18: Two slices of the tomographic reconstruction obtained with the SART algorithm. The slice (a) is horizontal and seen from above and the signals of some cavities can be observed: the Gran Cava (whose section is outlined by the black line), part of the beam tunnel and other signal regions that can be associated with other cavities. The low density region of the Gran Cava close to the measurements is in correspondence with the North wall of the collapse where the laser scanner reliefs are missing. The same region is the cause of the main low density trail of slice (b). In this vertical slice it is observed that the Voxels closest to the measures are those whose density is most modified. Consequently the density of the known vacuum volumes (such as the Gran Cava) remains high, around $2.5\,\mathrm{g/cm^3}$.

presented at the SART paragraph of section 4.2.2. However, the use of this normalization has led to an excessive fluctuation of the density of Voxels that are crossed by a few Rays (those that are on the edge of acceptance). This local normalization was however useful for other variants of the SART algorithm not described in this work.

To reduce the dependence of the density variation on the intersection length of the Voxels, the ART algorithm has been modified as follows. The density variation vector of the SART algorithm is still expressed by the average reported in formula 4.8, but its term $\Delta\boldsymbol{\rho}_i^{\mathrm{ART}}$ is no longer given by the equation 4.7 on page 73, but is replaced by the vector $\Delta\boldsymbol{\rho}_i^{\mathrm{modif}}$, whose jth

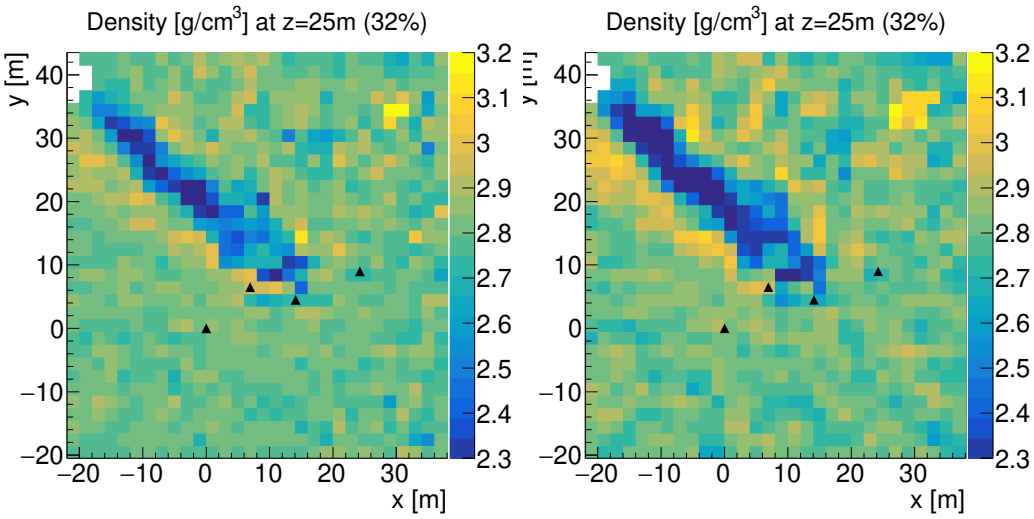

Figure 5.19: The two slices show the result of the simulated tomographic reconstruction in the case of a soil with uniform density with only the Gran Cava to be identified. The left image shows the reconstruction obtained with the classic SART algorithm while the right one was obtained with the modified algorithm and better highlights the reconstruction of the cavity.

element is given by the formula

$$\Delta \boldsymbol{\rho}_i^{\text{modif}}\Big|_j = \begin{cases} \dfrac{X_i - \boldsymbol{L}_i \cdot \boldsymbol{\rho}}{|\boldsymbol{L}_i|} & \text{if } L_{ij} > 0, \\ 0 & \text{if } L_{ij} = 0. \end{cases} \tag{5.3}$$

In this way all the Voxels intersected by a certain Ray are modified in the same way regardless of their intersection length.

To test the effectiveness of this method, the SART and the modified SART algorithms were applied to a simulated tomography with initial density and simulated density equal to $2.8\,\text{g/cm}^3$, except for the Voxels inside the Gran Cava, whose simulated density was set to zero. The results of the comparison of the two algorithms are shown in the two horizontal slices of figure 5.19. With both algorithms (SART and modified SART) 400 iterations were performed. It is observed that with the modified-SART algorithm a slightly higher contrast of the Gran Cava is obtained compared to the basic algorithm. This is due to the reduction of low density trails obtained for the Voxels closest to the detector. However, the density reconstructed in the void region inside the Gran Cava is still too high, being slightly smaller than $2.3\,\text{g/cm}^3$.

Despite the limited results, the SART algorithm has already been successfully used in [66] to perform a tomography based on absorption muon radiography measurements. In that case, however, the target, of reduced dimensions, was placed inside the tracker itself and was studied from a large number of observation points and at very different angles. For the mine measurements, on the other hand, there is no possibility of studying the target from multiple points of view and in particular in a direction close to the horizontal.

To further improve the algorithm some attempts have been made presented in chapter 6 together with other possible future developments.

Triangulation

The results of the application of the triangulation technique presented in section 4.2.3 on page 75 are shown below. The algorithm is based on the assumption that the target has substantially uniform density and that the variations of the mean density are mainly due to the presence of cavities. As previously described, however, the Temperino mine is a particularly varied context in which rocks of various types and densities alternate. The maps of figures 5.7 and 5.8 on page 95, regardless of the areas affected by the isolated cavities, suggest that the average density has different values for the four measurements, probably due to the presence of a skarn vein or voids near the installation points covering the whole acceptance. For this reason, with reference to formulas from 4.11 to 4.13 on page 76, four different values have been chosen for the average density $\rho_0 = (2.98, 2.83, 2.77, 2.8)\,\mathrm{g/cm^3}$ ordered from A to D. Only the average density of point A is significantly larger than the others consistently with the average density maps mentioned above. Then the following values were chosen for the other variables of the previous formulas: $n_{\mathrm{seed}} = n_{\mathrm{clu}} = 2$ and $L_V = 3\,\mathrm{m}$.

Therefore, for each measurement, clusters of low opacity were identified. For ease of visualization, the results are in any case expressed in terms of the average density in figure 5.20. This image shows the four average density maps already seen with the cluster margins superimposed. By comparing these distributions with those of figure 5.7 on page 94, it can be recognized that a large part of the Gran Cava and of the beam tunnel have been identified. In addition, other low-density regions were also delineated.

With the highlighted clusters a triangulation was carried out by selecting those Voxels which are observed in a cluster region from all four measurements. Using Voxels with a 1 m edge, the horizontal slices of figure 5.21 were obtained which show in blue the Voxels identified by the triangulation algorithm, to which a zero density value has been assigned. On the left of

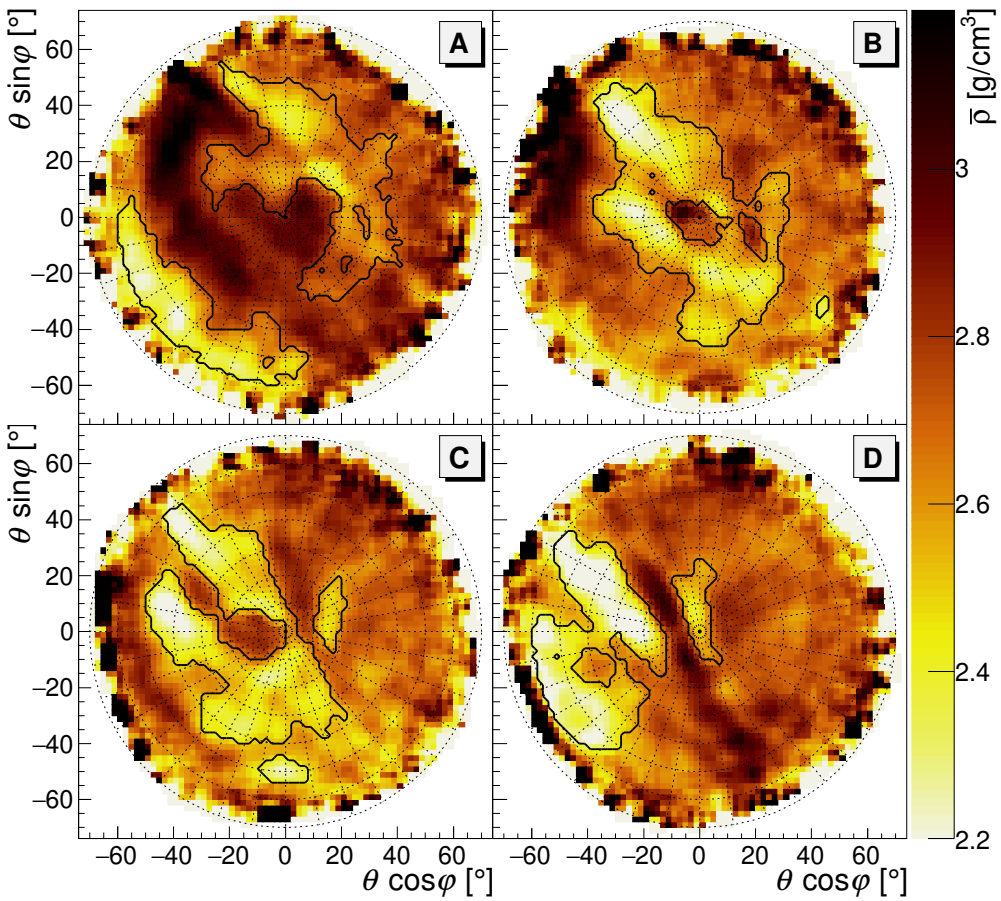

Figure 5.20: Average density maps (with smoothing filter). The black line delimits the low density clusters obtained as described in the text. As previously said for the opacity measurements, and therefore also for the clusters, only the angular regions with $\theta < 60°$ were considered.

figure 5.21 the slice corresponding to the sectioning plane $z = 27\,\mathrm{m}$ is shown and the black line, which indicates the section of the Gran Cava mesh, corresponds quite well with the blue signal obtained from the triangulation. Two other signal zones observed by all four measurements are then highlighted, which can therefore be associated with cavities. A reconstruction of these volumes starting from a single muographic measurement was presented in [33]. As previously discussed, the vacuum volumes reconstructed with the triangulation technique have a vertical halo (both above and below the real cavity) that we will address more forward. The left slice of figure 5.21 shows the same spatial region in x and y of the slice on the right, but for a higher

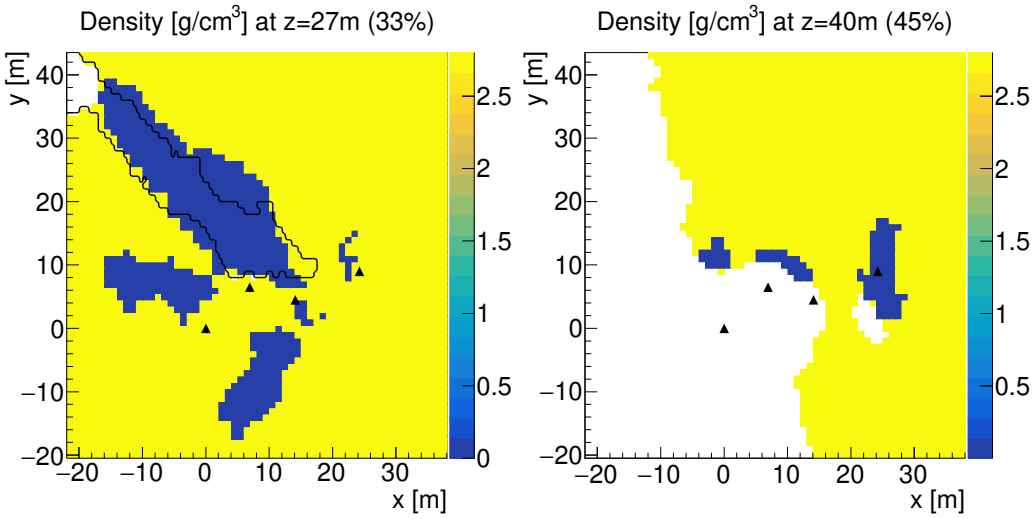

Figure 5.21: The two slices show the result of the triangulation algorithm. Cubic Voxels with 1 m edge were used. Voxels in blue are those that have been identified as empty by the algorithm. On the left you can see the Gran Cava, in accordance with its section highlighted by the black line, and two other signals associated with unknown cavities. On the right you can see a section of the beam tunnel, above the last measure on the right, and the North wall of the collapse of the Gran Cava, not mapped by the laser surveys.

altitude ($z = 40\,\mathrm{m}$) at the level of the access to the beam tunnel and just above the collapse of the Gran Cava. In correspondence with measurement D (the last one on the right) a section of the beam tunnel is observed. To create this image, the volume of air of the Gran Cava was introduced in the tomographic reconstruction (as described in section 5.3.1 on page 99) so as to remove the halo of the Gran Cava signal. In this way it is also possible to highlight the reconstructed cavity signal in correspondence with the North wall of the collapse of the Gran Cava which, as discussed at page 93, is missing in the laser scanner surveys and in the lidar.

Further developments to try to reduce the halo effect are presented in chapter 6.

Chapter 6

Conclusions and future developments

The results obtained from this work and the expected developments for the future are reported below, following the order in which they were presented in the text.

For the first time the complete geometric factor of the MIMA detector is calculated according to the trigger configuration usually chosen, and the analytical expression of the effective area is in agreement with the rate of particles measured in the free-sky configuration. A more detailed development of the effective area calculation presented in the text would allow to directly calculate the muon flux in a target measurement without the need to perform a free-sky measurement. In this way, numerous difficult-to-parameterize effects that are relevant for low-energy muons, and therefore for free-sky measurements, could be excluded: the low-energy electron background, the East-West effect and the dependence of muon flux on atmospheric pressure.

The equalization of the gains presented in section 2.2.2, together with other hardware and software developments, has made it possible to significantly improve the spatial and angular resolution of the detector compared to what described in previous works (see section 2.2.3).

In the text various effects that are currently neglected in the simulations are quantified: in some cases these phenomena have been assessed as not relevant, while in other cases more detailed studies will be required. In sections 2.2.5 and 2.2.7, the dependence of muon flux as a function of atmospheric pressure and the East-West asymmetry are quantitatively evaluated. These two effects, for measurements with thick targets, can be corrected directly in the free-sky measurements, but in the future a simulation that takes into account these dependencies as a function of the particle momentum may be useful (especially for targets with reduced thickness). Other approxima-

tions that will have to be evaluated in more detail in the future are reported in paragraph 3.2.3 on page 64, and the main points are reported below: an assessment of the background contribution of low-energy electrons, the propagation of measurement uncertainties of the muon spectrum at ground level and the use of the survival probabilities of muons as a function of their initial momentum.

Despite the approximations made, in section 3.2.3 on page 62 a quick and effective simulation is presented that allows you to directly convert transparency measurements into opacity measurements. Using a model of the target thickness it is then possible to obtain the average density maps. The results of this procedure are shown in section 5.2 for the measurements inside the Temperino mine and the study of the density maps already allows to identify anomalous regions associated with the presence of some cavities.

On the basis of the tomographic inversion techniques presented in section 4.2, a generic 3d reconstruction software has been developed that can be easily adapted to other measurement cases. The developed programs are highly configurable and allow you to easily import the geometry of the target, and the opacity measurements and to set the main characteristics of the World. The definition of MacroVoxels allows to improve the accuracy of the known geometric characteristics of the target regardless of the size of the Voxels. A slicing tool has also been implemented in the software which facilitates the visualization of various characteristics of the tomographic reconstruction. The tomographic inversion algorithms, present in the literature, have been improved and adapted for the identification of cavities, obtaining promising results: the SART algorithm has been modified to better highlight the signals associated with the Gran Cava; for the Chi-square minimum method, a potential-like function was introduced (with a minimum for a zero density value) through which it was possible to identify the Gran Cava for a simulated tomography; for the triangulation technique, combining the results of other works, a clustering algorithm was developed to identify empty volumes.

The tomographic techniques developed have shown an overall capability to identify some still unexplored empty cavities and volumes. However, further developments will be useful to clearly reconstruct the shape of the identified voids. Below are some possible future developments for the three tomographic techniques used.

The Chi-square minimum algorithm is computationally slower than the others (although a lot of work has already been done to improve this aspect) and it is therefore difficult to carry out a complete work of testing and optimization of the minimization parameters. The promising results obtained in the case of a simulated tomography are shown in figure 5.16b, where the vacuum of the Gran Cava can be correctly reconstructed, but isolated low-

density Voxels are created. To limit this effect, a further regularization term can be added that penalizes the isolated low density Voxels. To do this, it is possible to identify clusters consisting of adjacent low-density Voxels. Then for each of these clusters the volume and the surface are calculated. Finally, by introducing a regularization term equal to the sum of the surface-to-volume ratio of each cluster, it might be possible to remove small clusters by favoring larger ones such as that of the Gran Cava.

To try to further improve the SART algorithm, some possibilities are envisaged. The first one is to iteratively use filters that penalize the variation of the Voxels of the signal trails, to the advantage of those that correspond to the Gran Cava (which extend over larger spatial scales). To do this, filters with appropriately chosen spatial ranges can be used so that the Voxels of the signal trail are brought back to having the nominal density of the rock. The size of the filter kernel can then be progressively reduced to highlight smaller structures. With this in mind, an attempt was made to use an average filter which nevertheless produced an unwanted diffusion of the Gran Cava low-density signal. Alternatively, it is possible to use a mode or a threshold-average filter. Another possibility is to try to favor specific density values as already done for the Chi-square minimum algorithm. In this sense, for each Voxel it is possible to introduce further terms of density variation which are proportional to the negative derivative of the potential function $f(\rho; \tilde{\boldsymbol{\rho}}, \sigma)$ of equation 5.2. These variation terms can then be averaged with the ART ones in equation 4.8.

The triangulation algorithm is the one that has shown the greatest potential, clearly managing to identify the Gran Cava (including a volume of air not scanned by the lidar in correspondence with the North wall of the collapse), the beam tunnel and two further still unexplored cavities already highlighted in [33]. However, as already mentioned in the text, the main problem is the presence of a residual halo due to the fact that the Voxels that are observed in the projection of the cavity (both above and below) are still identified as made of air. To limit this effect it is possible to use the DART algorithm: by varying the density of the Voxels that are at the edge of the low density clusters, this algorithm can effectively modify the shape and thickness of the reconstructed cavities. Preliminary tests have already been carried out with this algorithm which have given good results but have highlighted the need to use filters (such as average, mode, median) that allow the topology of the cavities to be left unchanged.

In conclusion the results obtained with the tomographic reconstruction, especially those from the triangulation algorithm, are able to identify both known and unexplored cavities confirming the results of a previous work. Some inspections have been carried out in the region of interest, also with

a group of speleologists, that identified numerous gaps of modest size that cannot justify the results obtained. However, below one of the reconstructed and inaccessible cavities a filling was observed, such as those described in section 5.1.2 on page 80, which further confirm the presence of an ancient extraction void above it.

Appendix A

Threshold momentum for multilayer target

This appendix shows a simple method for calculating the equivalent opacity and the threshold momentum for muons for a target composed of separate layers of different material. For this method the continuous slowing down approximation is assumed to be valid.

For simplicity, consider the case in which the target is composed of only two different layers: for example, going from the detector to the outside, first a layer of rock followed by one of water, with opacity respectively equal to X_{1R} and X_{2W}. A more complicated configuration, in which the target is formed by a greater number of layers, is solved as a simple generalization of the case under consideration.

The goal is to calculate the minimum momentum, $p_{\min}$, that muons must have to be able to completely cross the target (both the water layer and the rock layer). This is equivalent to calculating the initial momentum of the muons which, after having completely crossed the target, have a substantially zero momentum. Reasoning backwards, for such muons the residual momentum before having crossed the rock layer, p_1, is simply given by

$$p_1 = p_R(X_{1R}),$$

where the conversion function $p_R(X)$ is the inverse of the CSDA range of muons in rock, $X_R(p)$, as shown in figure 3.3, that is $p_R(X) = X_R^{-1}(p)$.

The reasoning followed hereafter is illustrated in figure A.1 where the two curves $X_R(p)$ and $X_W(p)$ of the CSDA range of muons in water and rock are shown in a qualitative way. Once p_1 has been determined, it is possible to calculate the opacity of water equivalent to the rock layer ($X_{1W} \equiv X_{1R}$) as $X_{1W} = X_W(p_1) = X_W\big(p_R(X_{1R})\big)$. Once this is done, the total equivalent opacity of water is calculated as $X_{\mathrm{tot}W} = X_{1W} + X_{2W}$ and finally the threshold

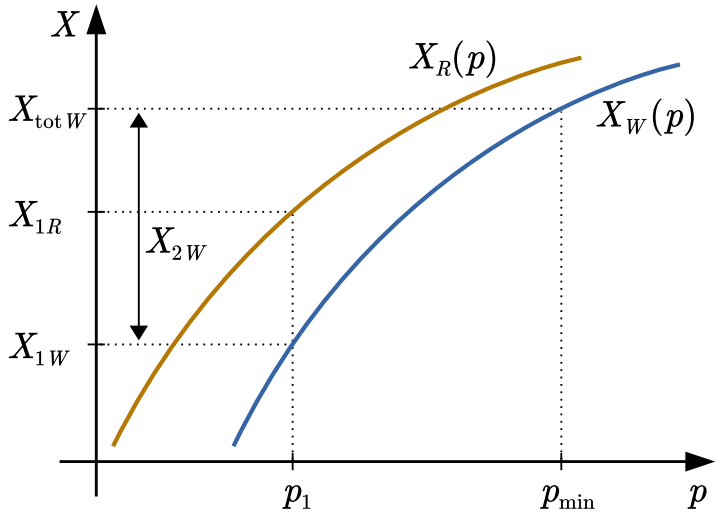

Figure A.1: Schematic illustration of the method for calculating the threshold momentum, p_{min}, for muons that first pass through a layer of water with opacity X_{2W} and then a layer of rock with opacity X_{1R}. To obtain the threshold momentum, we proceed backwards starting from the rocky layer. The two curves in brown and blue represent the CSDA range of muons in rock and water respectively as a function of the muon momentum. In figure it is implicitly assumed that the momentum is always less than 10^6 MeV/c, since below this value the range in water is less than that in rock (see figure 3.4).

momentum can be determined as $p_{\mathrm{min}} = p_W(X_{\mathrm{tot}W})$. By expressing what was previously said in a single formula, we obtain

$$p_{\mathrm{min}} = p_W\Big(X_W\big(p_R(X_{1R})\big) + X_{2W}\Big). \tag{A.1}$$

With the same method, other layers of different materials can also be added iteratively.

Appendix B

Maps of the opacity measurements

This appendix shows the polar maps of the opacity measurements (both the magnitude and the uncertainty) which constitute the input for the tomographic inversion algorithms. Unlike the average density maps, these opacity maps still contain the information of the morphology of the hill and therefore do not show only the signals associated with the presence of cavities.

The process of converting the measured transparency maps into the opacity maps is illustrate in paragraph 3.2.3 on page 62, while the procedure used to estimate the uncertainty on opacity is described in paragraph 3.2.3 on page 64.

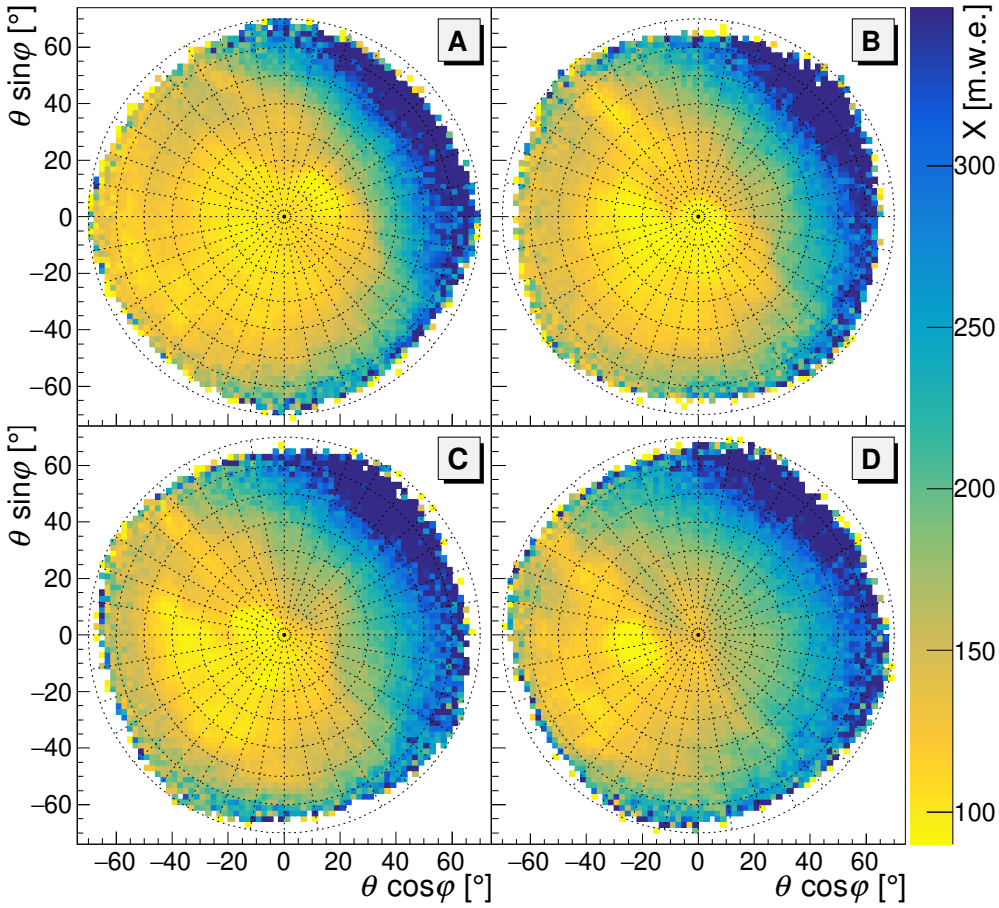

Figure B.1: The four opacity maps in polar coordinates. Also in these images there is a decrease in opacity in the South-West direction due to the decrease in the thickness of the hill in that direction. The opacity is expressed in meters of water equivalent ($1\,\mathrm{m.w.e.} = 10^2\,\mathrm{g\,cm^{-2}}$)

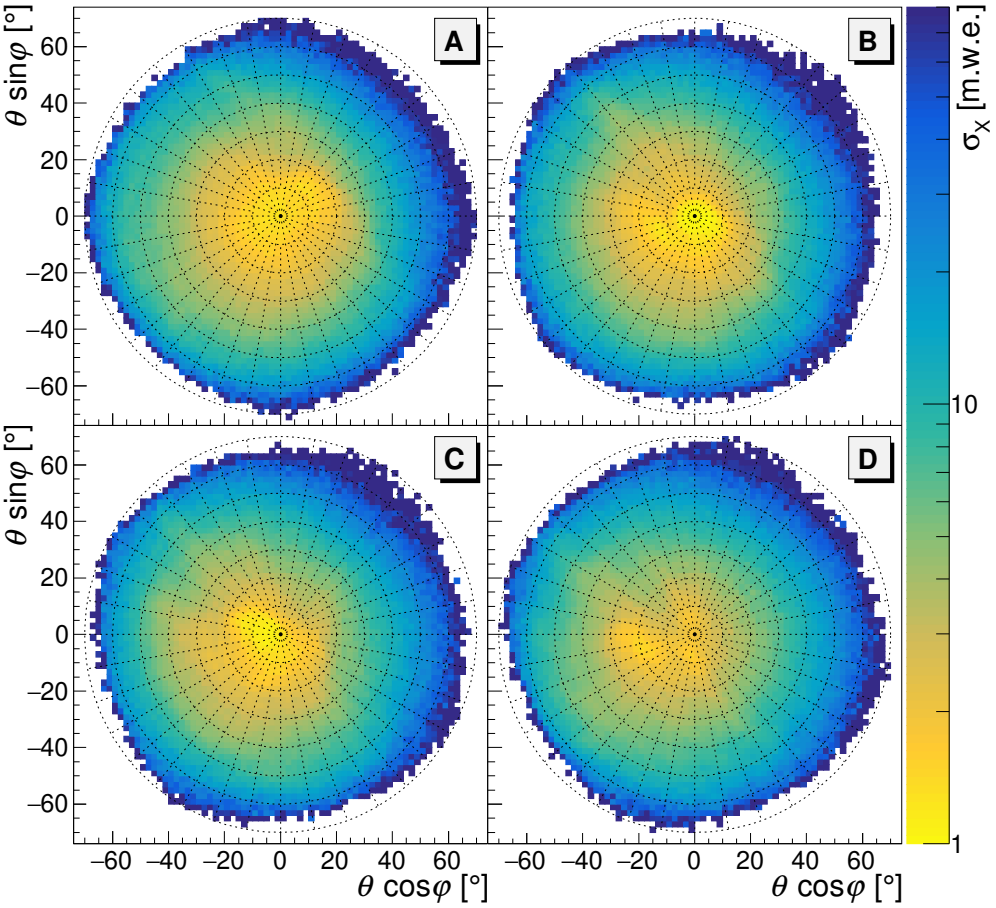

Figure B.2: Polar maps of the error on the opacity measure for the four measures. The error was calculated as described in section 3.2.3 on page 62. The measurement error increases going from the vertical direction towards the edges of the angular acceptance as the number of detected muons decreases. Vertically, the measurement error is of the order of one meter of water equivalent ($1\,\mathrm{m.w.e.} = 10^2\,\mathrm{g\,cm^{-2}}$).

Bibliography

[1] T. Wulf. "Observations on the radiation of high penetration power on the Eiffel tower". In: *Physikalische Zeitschrift* 11 (1910), p. 811.

[2] D. Pacini. "La radiazione penetrante alla superficie ed in seno alle acque". In: *Il Nuovo Cimento (1911-1923)* 3.1 (1912), pp. 93–100.

[3] V. F. Hess. "Uber Beobachtungen der durchdringenden Strahlung bei sieben Freiballonfahrten". In: *Phys. Zeits.* 13 (1912), pp. 1084–1091.

[4] B. Rossi. "Directional measurements on the cosmic rays near the geomagnetic equator". In: *Physical Review* 45.3 (1934), p. 212.

[5] P. D. Group et al. "Review of Particle Physics". In: *Progress of Theoretical and Experimental Physics* 2020.8 (Aug. 2020). 083C01. ISSN: 2050-3911. DOI: `10.1093/ptep/ptaa104`. eprint: `https://academic.oup.com/ptep/article-pdf/2020/8/083C01/33653179/ptaa104.pdf`. URL: `https://doi.org/10.1093/ptep/ptaa104`.

[6] D. J. Bird et al. "Detection of a cosmic ray with measured energy well beyond the expected spectral cutoff due to cosmic microwave radiation". In: *The Astrophysical Journal* 441 (1995), pp. 144–150.

[7] P. K. Grieder. *Cosmic rays at Earth*. Elsevier, 2001.

[8] T. Gaisser et al. *Cosmic rays and particle physics, Cambridge, UK: Univ.* 1990.

[9] L. Bonechi et al. "Atmospheric muons as an imaging tool". In: *Reviews in Physics* 5 (2020), p. 100038.

[10] D. E. Groom et al. "Muon stopping power and range tables 10 MeV–100 TeV". In: *Atomic Data and Nuclear Data Tables* 78.2 (2001), pp. 183–356. URL: `https://pdg.lbl.gov/2020/AtomicNuclearProperties/`.

[11] V. Kudryavtsev. "Muon simulation codes MUSIC and MUSUN for underground physics". In: *Computer Physics Communications* 180.3 (2009), pp. 339–346.

[12] P. Lipari et al. "Propagation of multi-TeV muons". In: *Physical Review D* 44.11 (1991), p. 3543.

[13] A. Donzella et al. "Historical building stability monitoring by means of a cosmic ray tracking system". In: *NuovoCimento C* 37 (2014), pp. 223–232.

[14] S. Procureur. "Muon imaging: Principles, technologies and applications". In: *Nuclear Instruments and Methods in Physics Research Section A: Accelerators, Spectrometers, Detectors and Associated Equipment* 878 (2018), pp. 169–179.

[15] R. Kaiser. "Muography: overview and future directions". In: *Philosophical Transactions of the Royal Society A* 377.2137 (2019), p. 20180049.

[16] E. P. George. "Cosmic rays measure overburden of tunnel". In: *Commonwealth Engineer* 455 (1955).

[17] L. W. Alvarez et al. "Search for hidden chambers in the pyramids". In: *Science* 167.3919 (1970), pp. 832–839.

[18] K. Morishima et al. "Discovery of a big void in Khufu's Pyramid by observation of cosmic-ray muons". In: *Nature* 552.7685 (2017), pp. 386–390.

[19] H. K. Tanaka et al. "High resolution imaging in the inhomogeneous crust with cosmic-ray muon radiography: The density structure below the volcanic crater floor of Mt. Asama, Japan". In: *Earth and Planetary Science Letters* 263.1-2 (2007), pp. 104–113.

[20] F. Ambrosino et al. "Joint measurement of the atmospheric muon flux through the Puy de Dôme volcano with plastic scintillators and Resistive Plate Chambers detectors". In: *Journal of Geophysical Research: Solid Earth* 120.11 (2015), pp. 7290–7307.

[21] H. K. Tanaka et al. "Radiographic visualization of magma dynamics in an erupting volcano". In: *Nature Communications* 5.1 (2014), pp. 1–9.

[22] K. Jourde et al. "Muon dynamic radiography of density changes induced by hydrothermal activity at the La Soufrière of Guadeloupe volcano". In: *Scientific reports* 6 (2016), p. 33406.

[23] F. Ambrosino et al. "The MU-RAY project: detector technology and first data from Mt. Vesuvius". In: *Journal of Instrumentation* 9.02 (2014), p. C02029.

[24] M. D'Errico et al. "Muon radiography applied to volcanoes imaging: the MURAVES experiment at Mt. Vesuvius". In: *Journal of Instrumentation* 15.03 (2020), p. C03014.

[25] V. Tioukov et al. "First muography of Stromboli volcano". In: *Scientific reports* 9.1 (2019), pp. 1–11.

[26] C. Cârloganu et al. "Towards a muon radiography of the Puy de Dôme". In: *GID* 2.2 (2012), pp. 765–780.

[27] R. Nishiyama et al. "First measurement of ice-bedrock interface of alpine glaciers by cosmic muon radiography". In: *Geophysical Research Letters* 44.12 (2017), pp. 6244–6251.

[28] D. Bryman et al. "Muon geotomography—bringing new physics to orebody imaging". In: *Building exploration capability for the 21st century* (2014), pp. 235–241.

[29] E. Guardincerri et al. "3D cosmic ray muon tomography from an underground tunnel". In: *Pure and Applied Geophysics* 174.5 (2017), pp. 2133–2141.

[30] N. Lesparre et al. "3-D density imaging with muon flux measurements from underground galleries". In: *Geophysical Journal International* 208.3 (2017), pp. 1579–1591.

[31] D. Schouten et al. "Muon Tomography Applied to a Dense Uranium Deposit at the McArthur River Mine". In: *Journal of Geophysical Research: Solid Earth* 123.10 (2018), pp. 8637–8652.

[32] G. Baccani et al. "Muon radiography of ancient mines: The san silvestro archaeo-mining park (campiglia marittima, tuscany)". In: *Universe* 5.1 (2019), p. 34.

[33] D. Borselli. "Muographic study of the Temperino mine with the MIMA detector: development and test of an algorithm for identification and reconstruction of cavities in three dimensions". (text in italian). MA thesis. P.zza S.Marco, 4 - 50121 Florence: University of Florence, 2019.

[34] K. N. Borozdin et al. "Radiographic imaging with cosmic-ray muons". In: *Nature* 422.6929 (2003), pp. 277–277.

[35] F. Riggi et al. "The Muon Portal Project: Commissioning of the full detector and first results". In: *Nuclear Instruments and Methods in Physics Research Section A: Accelerators, Spectrometers, Detectors and Associated Equipment* 912 (2018), pp. 16–19.

[36] P. Checchia et al. "INFN muon tomography demonstrator: past and recent results with an eye to near-future activities". In: *Philosophical Transactions of the Royal Society A* 377.2137 (2019), p. 20180065.

[37] D. Poulson et al. "Cosmic ray muon computed tomography of spent nuclear fuel in dry storage casks". In: *Nuclear Instruments and Methods in Physics Research Section A: Accelerators, Spectrometers, Detectors and Associated Equipment* 842 (2017), pp. 48–53.

[38] S. Pesente et al. "First results on material identification and imaging with a large-volume muon tomography prototype". In: *Nuclear Instruments and Methods in Physics Research Section A: Accelerators, Spectrometers, Detectors and Associated Equipment* 604.3 (2009), pp. 738–746.

[39] A. Clarkson et al. "Characterising encapsulated nuclear waste using cosmic-ray Muon Tomography (MT)". In: *2015 4th International Conference on Advancements in Nuclear Instrumentation Measurement Methods and their Applications (ANIMMA)*. IEEE. 2015, pp. 1–7.

[40] F. Ambrosino et al. "Assessing the feasibility of interrogating nuclear waste storage silos using cosmic-ray muons". In: *Journal of Instrumentation* 10.06 (2015), T06005.

[41] K. Borozdin et al. "Cosmic ray radiography of the damaged cores of the Fukushima reactors". In: *Physical review letters* 109.15 (2012), p. 152501.

[42] H. Miyadera et al. "Imaging Fukushima Daiichi reactors with muons". In: *Aip Advances* 3.5 (2013), p. 052133.

[43] G. Saracino et al. "The MURAVES muon telescope: technology and expected performances". In: *Annals of Geophysics* 60.1 (2017), p. 0103.

[44] G. Baccani. "Production and calibration of the MIMA cosmic ray tracker for application to muon radiography and first measurements". (text in italian). MA thesis. P.zza S.Marco, 4 - 50121 Florence: University of Florence, 2017.

[45] G. Baccani et al. "The MIMA project. Design, construction and performances of a compact hodoscope for muon radiography applications in the context of archaeology and geophysical prospections". In: *Journal of Instrumentation* 13.11 (2018), P11001.

[46] L. Bonechi et al. "Multidisciplinary applications of muon radiography using the MIMA detector". In: *Journal of Instrumentation* 15.05 (2020), p. C05030.

[47] G. Saracino et al. "Imaging of underground cavities with cosmic-ray muons from observations at Mt. Echia (Naples)". In: *Scientific reports* 7.1 (2017), pp. 1–12.

[48] L. Cimmino et al. "3d muography for the search of hidden cavities". In: *Scientific reports* 9.1 (2019), pp. 1–10.

[49] G. Baccani et al. "The Reliability of Muography Applied in the Detection of the Animal Burrows within the River Levees Validated by Means of Geophysical Techniques". In: *Journal of Applied Geophysics* (2021). (Submitted article).

[50] J. Sullivan. "Geometric factor and directional response of single and multi-element particle telescopes". In: *Nuclear Instruments and methods* 95.1 (1971), pp. 5–11.

[51] R. Brun et al. "ROOT—an object oriented data analysis framework". In: *Nuclear Instruments and Methods in Physics Research Section A: Accelerators, Spectrometers, Detectors and Associated Equipment* 389.1-2 (1997), pp. 81–86.

[52] T. Ullrich et al. *Treatment of Errors in Efficiency Calculations*. Tech. rep. physics/0701199. Jan. 2007. URL: `https://cds.cern.ch/record/1010669`.

[53] *Enviro for Raspberry Pi*. URL: `https://media.digikey.com/pdf/Data%20Sheets/Pimoroni%20PDFs/PIM486_Web.pdf`.

[54] L. Bonechi et al. "Development of the ADAMO detector: test with cosmic rays at different zenith angles". In: *International Cosmic Ray Conference* 9 (Jan. 2005), p. 283.

[55] O. Adriani et al. "PAMELA measurements of cosmic-ray proton and helium spectra". In: *Science* 332.6025 (2011), pp. 69–72.

[56] E. Vannuccini et al. "Study of the deuterium spectrum in cosmic rays with the CAPRICE98 experiment". PhD thesis. PhD thesis, Università degli studi di Firenze, 2001.

[57] GEANT Collaboration et al. "GEANT4–a simulation toolkit". In: *Nucl. Instrum. Meth. A* 506.25 (2003).

[58] V. Niess et al. "Backward Monte-Carlo applied to muon transport". In: *Computer Physics Communications* 229 (2018), pp. 54–67.

[59] F. Hivert et al. "Simulations of the muon flux sensitivity to rock perturbation associated to hydrogeological processes". In: *E3S Web of Conferences*. Vol. 4. EDP Sciences. 2014, p. 01003.

[60] G. Cowan. *Statistical data analysis*. Oxford university press, 1998.

[61] M. J. Berger et al. *Stopping-power and range tables for electrons, protons, and helium ions*. NIST Physics Laboratory Gaithersburg, MD, 1998. URL: `https://physics.nist.gov/PhysRefData/Star/Text/ESTAR.html`.

[62] A. Erlandson et al. "One-sided muon tomography—A portable method for imaging critical infrastructure with a single muon detector". In: *CNL Nuclear Review* 7.1 (2016), pp. 1–9.

[63] M. Rosas-Carbajal et al. "Three-dimensional density structure of La Soufrière de Guadeloupe lava dome from simultaneous muon radiographies and gravity data". In: *Geophysical Research Letters* 44.13 (2017), pp. 6743–6751.

[64] K. Davis et al. "Joint 3D of muon tomography and gravity data to recover density". In: *ASEG Extended Abstracts* 2012.1 (2012), pp. 1–4.

[65] K. Jourde et al. "Improvement of density models of geological structures by fusion of gravity data and cosmic muon radiographies". In: *Geoscientific Instrumentation, Methods and Data Systems* 4 (2015), pp. 177–188.

[66] G. Baccani. "Muon absorption tomography of a lead structure through the use of iterative algorithms". In: *Journal of Instrumentation* 15.12 (2020), P12024.

[67] C. Civinini et al. "Proton Computed Tomography: iterative image reconstruction and dose evaluation". In: *Journal of Instrumentation* 12.01 (Jan. 2017), pp. C01034–C01034. DOI: `10.1088/1748-0221/12/01/c01034`. URL: `https://doi.org/10.1088%2F1748-0221%2F12%2F01%2Fc01034`.

[68] A. C. Kak et al. "Principles of computerized tomographic imaging". In: *Medical Physics* 29.1 (2002), pp. 107–107.

[69] K. J. Batenburg et al. "DART: a practical reconstruction algorithm for discrete tomography". In: *IEEE Transactions on Image Processing* 20.9 (2011), pp. 2542–2553.

[70] S. Vezzoni et al. "Reverse telescoping in a distal skarn system (Campiglia Marittima, Italy)". In: *Ore Geology Reviews* 77 (2016), pp. 176–193.

[71] A. Dini et al. "Miniere e minerali del Campigliese". In: *Milano: Gruppo Mineralogico Lombardo* (2013).

[72] A. Semplici. "Bianca e sfolgorante appare la Rocca–Guida al Parco Archeominerario di San Silvestro". In: *Ed. Parchi Val di Cornia Piombino* (2011).

[73] D. Girardeau-Montaut. *CloudCompare*. 2016.

[74] M. Kazhdan et al. "Poisson surface reconstruction". In: *Proceedings of the fourth Eurographics symposium on Geometry processing*. Vol. 7. 2006.

[75] M. Hatlo et al. "Developments of mathematical software libraries for the LHC experiments". In: *IEEE Transactions on Nuclear Science* 52.6 (2005), pp. 2818–2822.